UNIVERSITÀ DEGLI STUDI DI PADOVA

Dipartimento di Fisica e Astronomia "Galileo Galilei"

Master Degree in Physics

Final Dissertation

Quasi-frictionless water flow in narrow carbon nanotubes

Thesis supervisor

Dr. Alberto Ambrosetti

Thesis co-supervisor

Prof. Pier Luigi Silvestrelli

Candidate

Niccolò Damian

Academic Year 2023/2024

Abstract

Recent experiments revealed surprisingly high water-flow rates in narrow carbon nanotubes, with permeabilities that tend to diverge when the nanotube diameter is decreased towards the nanometer scale. This physical phenomenon could not be explained within classical fluid mechanics, and could not even be reproduced by semi-classical molecular dynamics. Here we aim to investigate the problem from a quantum-mechanical viewpoint, starting from state of the art ab-initio simulations. Systematic characterization of water-nanotube interactions under different phases/conditions will help the comprehension of the subtle mechanisms that eventually cause quasi-frictionless flow. On the same basis, possible relations to superfluidity will be explored.

Contents

Chapter 1

Introduction

Carbon nanotubes (CNTs) represent a paradigmatic example of quasi one-dimensional systems: referring to **Figure 1.1**, a CNT can be described as a graphite sheet rolled up into a cylinder, matching crystallographically equivalent sites (in the case of the figure points along $\overline{OB}$ with points along $\overline{AB'}$). The type of nanotubes considered in this thesis work, i.e. single-walled CNTs, is characterized by one-atom thickness, a circumference of the order of 1 nm, and ideally infinite length. CNTs are described in terms of the *chiral vector* $\vec{C}_h$

$$\vec{C}_h = n\vec{a}_1 + m\vec{a}_2\,, \tag{1.1}$$

with (n, m) two integer numbers called *chiral coefficients* and $\vec{a}_1$, $\vec{a}_2$ the vectors of the basis of the hexagonal (or triangular) honeycomb direct lattice

$$\vec{a}_1 = \left(\frac{\sqrt{3}}{2}, \frac{1}{2}\right)a\,, \quad \vec{a}_2 = \left(\frac{\sqrt{3}}{2}, -\frac{1}{2}\right)a\,, \tag{1.2}$$

$a = \sqrt{3}\,a_{\mathrm{C-C}} = 2.46\,\text{Å}$ being the lattice constant of graphite, with $a_{\mathrm{C-C}} = 1.42\,\text{Å}$ being its nearest neighbour $\mathrm{C} - \mathrm{C}$ distance.

In terms of chiral coefficients n and m, one can define the *CNT diameter* d_{CNT} as

$$d_{\mathrm{CNT}} = \frac{C_h}{\pi} = \sqrt{3}\,a_{\mathrm{C-C}}\frac{\sqrt{n^2 + nm + m^2}}{\pi}\,, \tag{1.3}$$

with C_h being the length of the chiral vector, and the angle θ formed by $\vec{C}_h$ with respect to the zigzag direction of $\vec{a}_1$, called *chiral angle*, as

$$\theta = \arctan\left[\sqrt{3}\frac{m}{m + 2n}\right]; \tag{1.4}$$

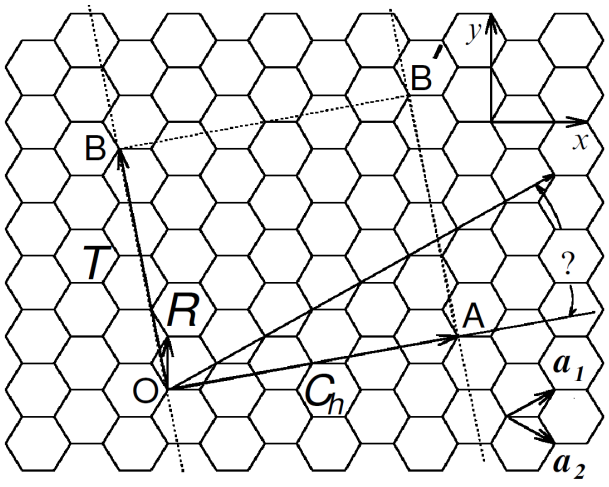

Figure 1.1: Graphene direct honeycomb lattice with primitive lattice vectors $\vec{a}_1$ and $\vec{a}_2$ and with the chiral vector $\vec{C}_h$. The picture is taken from Ref. [1].

Membrane	Pore diameter (nm)	Enhancement over no-slip, hydrodynamic flow (minimum)
DWNT 1	1.3 to 2.0	1500 to 8400
DWNT 2	1.3 to 2.0	680 to 3800
DWNT 3	1.3 to 2.0	560 to 3100
Polycarbonate	15	3.7

Figure 1.2: Ratio between experimental water flow rates and predictions from continuum flow model for different double-walled carbon nanotube (DWNT) membranes; polycarbonate membrane data serve as reference. Data are taken from Ref. [4].

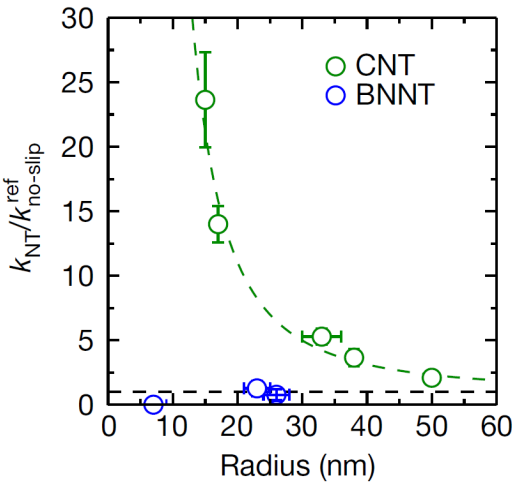

Figure 1.3: Water permeability k_{NT} for CNT and boron nitride nanotubes (BNNT) of different radius R; the reference value $k^{\mathrm{ref}}_{\mathrm{no-slip}} = \frac{R^2}{8}$ corresponds to the permeability of a nanotube of radius R with no-slip boundary condition at its surface. The plot is taken from Ref. [5].

this angle ranges from 0° (corresponding to zigzag CNTs) to 30° (characteristic of armchair nanotubes).

Consequently, a CNT can be identified in terms of either (n, m) or $(d_{\mathrm{CNT}}, \theta)$. All armchair CNTs are characterized by $n = m$.

The type of electronic energy band structure of a CNT depends on the values of indices (n, m): if they satisfy

$$2n + m = 3q,\ q\,\text{integer}, \tag{1.5}$$

the nanotube is metallic (which occurs with approximately 1/3 of the possible CNTs), otherwise it is semiconducting. From this condition one can see that all armchair nanotubes (n, n) present a metallic conduction behaviour. [1]

In the last years [2–4], experiments evidenced enhanced water flow through CNT membranes, compared to classical fluid-mechanics predictions. Measured enhancements amount to one order of magnitude at pore size of 44 nm, $4 \div 5$ orders of magnitude at pore size of 7 nm and $3 \div 4$ orders of magnitude when pore size varies between 1.3 nm and 2.0 nm, as reported in **Figure 1.2** for the last case. Experimental water-flow enhancements are huge, but exhibit scattered magnitude. Hence, presently unexplored factors could play a non-trivial role in water-CNT friction effects. Water permeability in individual CNTs was also experimentally seen to increase as the CNT radius decreases, and was expected to diverge for radii smaller than 10 nm [5], as seen in **Figure 1.3**.

Recent theoretical investigations [6, 7] showed that single helium atoms or single water molecules (shown in **Figure 1.4**) can flow through a $(5, 5)$ CNT experiencing no friction if their initial velocity is smaller than a critical value v_{crit}. Indeed, below this threshold, water-CNT phonon scattering (responsible for the energy transfer between flowing particle and CNT) is not allowed and, in the absence of such energy transfer, the flowing particle experiences no friction. This phenomenon presents evident analogies with superfluidity. However, even though both mechanisms rely on Landau's superfluidity

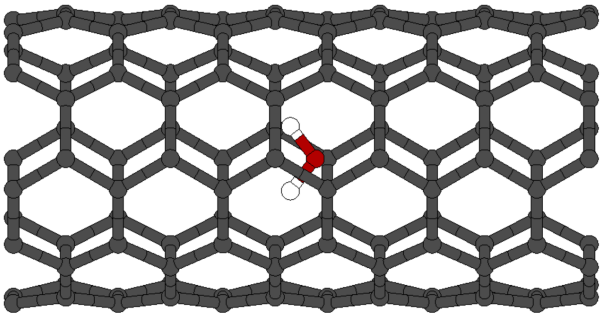

Figure 1.4: Representation of a water molecule in a $(5, 5)$ armchair carbon nanotube, realized with the visualization program *XCrySDen* [8]: carbon atoms are in grey, oxygen atoms in red and hydrogen atoms in white.

criterion, the present remains a single-particle effect, whereas superfluidity is a many-body effect. For instance, the dispersion relation used in superfluidity stems from many-body excitations in the flowing medium. In the case under analysis (that could be denoted as *superflow* or *quasi-frictionless flow*), instead, it is the CNT to present many-body effects, while the flowing He atom or H_2O molecule behaves as a quasi-free particle.

Quasi-frictionless flow could neither be explained by classical fluid mechanics, nor by semi-classical molecular dynamics simulations. In this thesis CNTs will be addressed employing different theoretical and computational tools in order to examine complementary points of view. The relevance of this specific subject is both theoretical (due to the novelty of the phenomenon), and technological (due to possible development of non-dissipative transport). The study and rationalization of friction properties could eventually enable efficient water filtration at the nanometer scale, or nanofluidical injection. From the physical viewpoint, it is also interesting to shed light on the reasons why Born-Oppenheimer molecular dynamics could not describe frictionless flow.

In **Chapter 2** a classical effective model is developed to describe the interaction between a flowing particle and a $(5, 5)$ CNT. The dispersion relation of the chain will effectively account for a phonon mode that can be excited upon scattering with the flowing particle.

In **Chapter 3** Born-Oppenheimer molecular dynamics simulations (BOMDs) with different types of force fields are performed using the aforementioned effective model: the comparison of these results with quantum-mechanics will help to identify possible classical dissipation mechanisms absent in the quantum-mechanical case below the critical speed.

In **Chapter 4** *ab-initio* simulations are used to characterize corrugation potentials (i.e. the barrier experienced by an encapsulated particle during its flow) for a single water molecule and for a chain of interacting H_2O in CNTs with different chiralities. First-principle calculations are also used to extract realistic parameters for the $(5, 5)$ CNT effective model. Corrugation of interface potentials and phonon dispersions are two of the main parametrization tasks. In fact, these will directly contribute to the energy-exchange between water and CNT.

A number of relevant results are found in this thesis.

1. BOMD simulations of the particle-chain effective model show that:

   (a) in the purely harmonic case, the particle initially releases a small fraction of its energy to the chain. However, after a short transient, periodic oscillations emerge and persist throughout the trajectory. The particle either oscillates between two carbons or flows along the chain, with oscillating particle-chain energy exchange, and oscillating chain energy;

   (b) if suitable anharmonic contributions are added in the chain, one can observe an enhancement in the particle-chain energy exchange (i.e. the particle loses more energy) and disappearance of its periodic oscillations. The values of the anharmonic coefficients at which the energy exchange becomes the highest depend on the height of the corrugated potential and on the initial velocity of the particle; the energy of the particle is transferred and harvested in the chain;

(c) if viscous contributions further act on chain atoms, one finds energy losses both in the chain and in the particle, which increase with the height of the corrugated potential and with the values of the damping coefficient. The chain energy loss does not occur immediately: it first requires the particle to transfer part of its energy to the chain, and follows a specific behaviour which varies as a function of involved parameters;

2. First-principle simulations show that the corrugation of the interface potential tends to decrease when the CNT diameter increases. This is true both for the single water molecule and for a periodic quasi-1D ice structure, with a higher barrier per unit molecule when water molecules are interacting. Moreover, metallic CNTs are consistently associated with weaker corrugations.

Chapter 2

Carbon nanotube classical model

Due to the complexity of the $(5,5)$ armchair CNT, we will simplify our simulations introducing an effective model that retains the most important features, i.e. periodicity, phonon spectrum and interaction with a particle flowing along the CNT axis. This effective model consists of a one-dimensional periodic linear chain, with a supercell containing N carbon atoms of mass M interacting with nearest neighbours by means of identical springs (which mimic phonons) of elastic constant K and rest length L (representing the lattice parameter of the carbon chain); the chain Hamiltonian is then

$$H_{\text{chain}} = \sum_{n=1}^{N} \frac{P_n^2}{2M} + \frac{K}{2} \sum_{\substack{n=1 \\ n \text{ per}}}^{N} (X_n - X_{n-1} - L)^2 \,, \tag{2.1}$$

where $X_n = \frac{L}{2} + (n-1)L$[1] is the position of the n^{th} C atom, $P_n = MV_n$ is its momentum, V_n its velocity and "n per" in the summation ensures that periodic boundary conditions are enforced.

Considering a particle (in particular a He atom or a H_2O molecule) of mass m and position x flowing through the CNT along its longitudinal axis with a non-zero velocity v, the isolated particle Hamiltonian is

$$H_{\text{part}} = \frac{p^2}{2m} \,, \tag{2.2}$$

with p being its momentum, and the interaction potential between the particle and the chain can be modeled with the periodic potential

$$V_{\text{part,chain}}(x; \{X_n\}) = V_0 \sum_{\substack{n=1 \\ n \text{ per}}}^{N} e^{-\left(\frac{x - X_n}{\Delta}\right)^2} \,. \tag{2.3}$$

By adjusting the parameters V_0 and Δ one can reproduce different interactions between the two sub-systems: V_0 describes the amplitude of the potential and Δ the width of the Gaussians. A visual representation of this effective model is shown in **Figure 2.1**.

[1] The zero of the x-axis is taken between the first C atom and the preceding periodic replica of the N^{th} one, i.e. such that the position of the former is $\frac{L}{2}$.

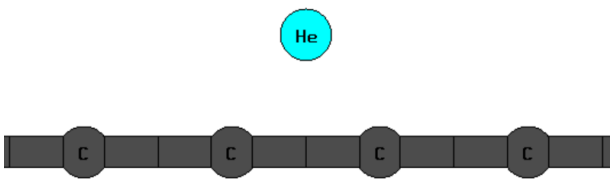

Figure 2.1: Representation of the classical effective model used to describe the flow of a particle (helium in this case) inside a $(5,5)$ CNT. It was realized with the visualization program *XCrySDen* [8]: carbon atoms are in grey while the flowing particle is in turquoise.

2.1 Dispersion relation calculations

We used this effective model to compute dispersion relations relative to the chain and to the flowing particle.

2.1.1 Isolated chain phonon spectrum

Expressing the n^{th} carbon atom position X_n in Fourier series (in which "IBZ" stands for "First Brillouin Zone")

$$\begin{cases} X_n = \frac{1}{\sqrt{N}} \sum\limits_{k_l \in IBZ} \tilde{X}_{k_l} e^{ik_l L n} = \frac{1}{\sqrt{N}} \sum\limits_{l=-N/2+1}^{N/2} \tilde{X}_{k_l} e^{2\pi i \frac{ln}{N}} \\ \tilde{X}_{k_l} = \frac{1}{\sqrt{N}} \sum\limits_{n=1}^{N} X_n e^{-ik_l L n} = \frac{1}{\sqrt{N}} \sum\limits_{n=1}^{N} X_n e^{-2\pi i \frac{ln}{N}} \end{cases} \tag{2.4}$$

(where second equalities come from periodicity, i.e. to satisfy $e^{ik_l LN} = 1$, yielding $k_l = \frac{2\pi}{L}\frac{l}{N}$, with $l = 0, \pm 1, \ldots, \frac{N}{2}$) and doing the same with momentum P_n, one obtains

$$H_{\text{chain}} = \sum_{l=-N/2+1}^{N/2} \left\{ \frac{|\tilde{P}_{k_l}|^2}{2M} + \frac{1}{2}\left[4K \sin^2\left(\frac{\pi l}{N}\right)\right] |\tilde{X}_{k_l}|^2 \right\} + \frac{K}{2} L^2 \,, \tag{2.5}$$

which is the Hamiltonian of a set of uncoupled quantum harmonic oscillators, whose l-dependent oscillation frequency is provided by:

$$M\omega_l^2 = 4K \sin^2\left(\frac{\pi l}{N}\right) \implies \omega_l = \omega(k_l) = \sqrt{\frac{4K}{M}} \left| \sin\left(\frac{\pi l}{N}\right) \right| = \sqrt{\frac{4K}{M}} \left| \sin\left(\frac{k_l L}{2}\right) \right| . \tag{2.6}$$

In order to be later able to compare the chain phonon spectrum with the energy bands of a flowing particle encapsulated in the periodic CNT, we impose that the slope of ω_l at $l = 0$ corresponds to the velocity of the slowest mode among acoustic ones in the nanotube, i.e. the velocity of the transverse-acoustic mode $v_{\text{TA}} = 9.841 \times 10^3\,\text{m/s}$ [7]; thus we get, expanding (2.6) for small k_l

$$\sqrt{\frac{4K}{M}}\frac{L}{2} = v_{\text{TA}} \implies \sqrt{\frac{4K}{M}} = \omega = \frac{2v_{\text{TA}}}{L} \text{ or } K = \frac{M}{4}\left(\frac{2v_{\text{TA}}}{L}\right)^2 = \frac{M\omega^2}{4} \,. \tag{2.7}$$

Proceeding this way we end up with the following phonon spectrum for the isolated chain

$$\omega_l = \omega(k_l) = \frac{2v_{\text{TA}}}{L} \left| \sin\left(\frac{\pi l}{N}\right) \right| = \omega \left| \sin\left(\frac{\pi l}{N}\right) \right| , \tag{2.8}$$

which is shown in **Figure 2.2**.

Finally, we can rewrite the linear chain Hamiltonian as

$$H_{\text{chain}} = \sum_{n=1}^{N} \frac{P_n^2}{2M} + \frac{M\omega^2}{8} \sum_{\substack{n=1 \\ n \text{ per}}}^{N} (X_n - X_{n-1} - L)^2 \,. \tag{2.9}$$

2.1.2 Particle dispersion relation [9]

So as to find the energies of the particle in presence of the chain, to be later compared with the chain phonon spectrum, we solve the corresponding Schrödinger equation

$$\left[-\frac{\hbar^2}{2m}\nabla^2 + V_{\text{part,chain}}(x; \{X_n\}) \right] \psi^{\text{part}}(x) = E\, \psi^{\text{part}}(x) \,, \tag{2.10}$$

in which the chain-particle interaction plays the role of an external potential.

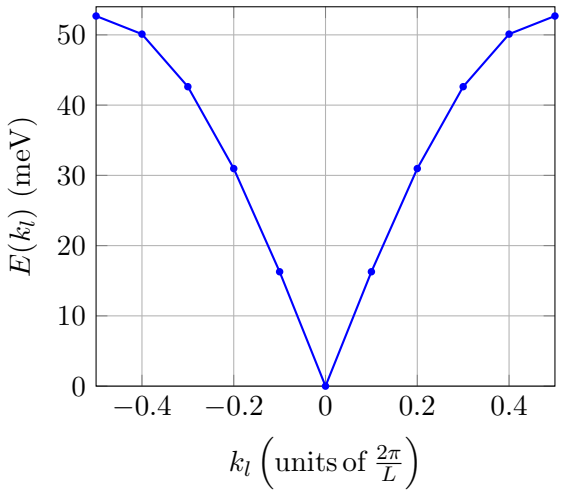

Figure 2.2: Phonon energy band for the linear chain of carbons. The coefficient in front of the module of the sine function is 52.686 meV (or 79.936 THz in terms of frequency ω).

In order to do it, we proceed[2] to expand both $\psi^{\text{part}}(x)$ and $V_{\text{part,chain}}(x;\{X_n\})$ in Fourier modes

$$\begin{cases} \psi^{\text{part}}(x) = \sum_q C_q e^{iqx} \\ V_{\text{part,chain}}(x;\{X_n\}) = \sum_{G_m} V_{G_m} e^{iG_m x} \end{cases} , \tag{2.11}$$

with $V_{G_m} = \frac{1}{L}\int_{-\frac{L}{2}}^{\frac{L}{2}} dx\, V_{\text{part,chain}}(x;\{X_n\})\, e^{-iG_m x}$, q being a generic one-dimensional vector of the reciprocal space and $G_m = \frac{2\pi}{L}m$ ($m \in \mathbb{Z}$) a one-dimensional vector in the reciprocal lattice due to the periodicity of $V_{\text{part,chain}}$.

Inserting (2.11) in (2.10) one gets that

$$\frac{\hbar^2 q^2}{2m} C_q + \sum_{G_l} V_{G_l} C_{q-G_l} - E\, C_q = 0\,; \tag{2.12}$$

however, noticing that every point in reciprocal space can be described as sum of the vector G'_l pointing to the corresponding cell in reciprocal lattice and of the vector k in the cell pointing to that point

$$q = k - G'_l\,, \tag{2.13}$$

with suitable changes of dummy indices one obtains in the end

$$\frac{\hbar^2}{2m}(k-G_l)^2 C_{k-G_l} + \sum_{G'_l} V_{G'_l - G_l} C_{k-G'_l} = E\, C_{k-G_l}\,. \tag{2.14}$$

This equation can be rewritten in matrix form as

$$\hat{A}(k)\,\vec{C}(k) = E\,\vec{C}(k)\,, \tag{2.15}$$

in which $\hat{A}(k)$ is a $(2N_G+1)\times(2N_G+1)$ matrix (where $2N_G+1$ is the number of considered G-vectors), whose matrix elements are

$$A_{hl}(k) = \frac{\hbar^2}{2m}\left(\frac{2\pi}{L}\right)^2 (n_k - l)^2 \delta_{h,l} + V_{h-l}\,, \tag{2.16}$$

[2]This is the same procedure used to get, from the Schrödinger equation of a single electron in the periodic potential of a metal, the corresponding Central Equation, since the problem is the same but with the particle in place of the electron and with C atoms in place of metallic nuclei. A different approach, using the expression for ψ^{part} coming from Bloch theorem and yielding anyway the same result, is shown in **Appendix A**.

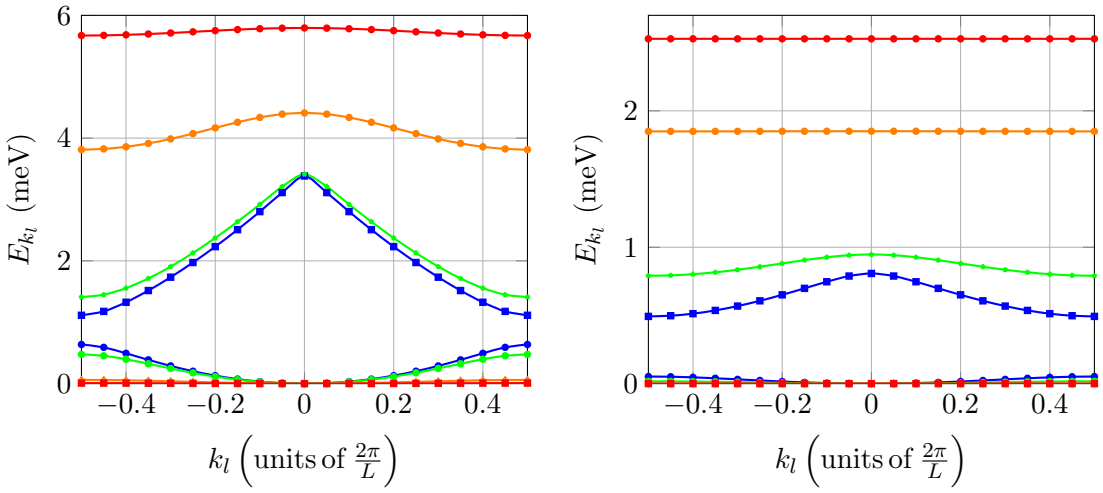

(a) He energy bands **(b)** H_2O energy bands

Figure 2.3: Energy bands for He and for H_2O interacting with the chain for different values of the amplitude V_0: red bands correspond to 1 meV, orange ones to 0.5 meV, green ones to 0.1 meV and blue ones to 0.05 meV. Eigenenergies were shifted suitably to have the minimum of the lowest band in 0 and were computed using $N_G = 20$. They become more and more bent for smaller V_0 and they are flatter for water than for helium due to the higher mass of the former.

where $n_k \in \left\{ -\frac{1}{2} + \frac{1}{N}, \dots, \frac{1}{2} - \frac{1}{N}, \frac{1}{2} \right\}$ is such that $k = \frac{2\pi}{L} n_k \in \text{IBZ}$. Moreover, the coefficient V_{h-l} is

$$V_{h-l} = \frac{1}{L} \int_{-\frac{L}{2}}^{\frac{L}{2}} dx\, V_{\text{part,chain}}(x; \{X_n\})\, e^{-i(G_h - G_l)x} \approx$$

$$\approx \frac{V_0}{L} \sum_{n=1}^{N} \int_{-\infty}^{+\infty} dx\, e^{-\left(\frac{x - X_n}{\Delta}\right)^2} e^{-i(G_h - G_l)x} = \sqrt{\pi} \frac{V_0 N \Delta}{L} e^{-\left[\frac{\pi \Delta}{L}(h-l)\right]^2} (-1)^{(h-l)}, \quad (2.17)$$

with the last factor $(-1)^{(h-l)}$ related to the fact that $X_n = \frac{L}{2} + (n-1)L$.

Eigenenergies are obtained solving numerically the eigenproblem (2.15) (e.g. using the *C++* template library for linear algebra *Eigen* [10]): they arrange on band structures as functions of the wave vector k_l, as illustrated in **Figure 2.3a** for He and in **Figure 2.3b** for H_2O, obtained using $N_G = 20$. As one can see, bands become more and more bent for smaller V_0 and they are flatter for water than for helium due to the higher mass of the former.

Chapter 3

Born-Oppenheimer molecular dynamics simulations

In order to better understand why Born-Oppenheimer molecular dynamics simulations (also abbreviated as *BOMDs*) are not able to properly describe characteristic features of water flow in CNTs, the effective model developed in the previous chapter was combined with different features: first of all purely harmonic $C-C$ bonds were considered, then anharmonic contributions were added. Finally, viscous terms acting on C atoms were introduced (both with and without anharmonic coefficients).

Two different algorithms were used in order to integrate the equations of motion throughout dynamical simulations. Every time the stability and reasonableness of numerical results were explicitly checked.

3.1 General computational details on BOMDs

In this section details regarding simulations with all kinds of $C-C$ bonds are reported.

3.1.1 Values of parameters

Equations of motion were integrated, regardless of the algorithm employed, with a timestep dt smaller or equal to 1 fs[1], for different simulation lengths (of the order of 5 ns) and with the parameters exposed in **Table 3.1**. In particular, the values of L and Δ^2 were obtained fitting *ab-initio* data from a preliminary characterization of the water-$(5,5)$ CNT corrugation potential when the water dipole was rotated by $-48°$ with respect to the CNT axis, as shown in **Figure 3.1a**; the software *Gnuplot* [11] was used for the fit. **Figure 3.1b** shows the resulting interaction potential.

In all molecular dynamics simulations the particle was considered at a distance of 3.409 595 Å from the chain (i.e. along the CNT axis), and was placed at $t = 0$ either between the second and third C atom (i.e. at $x_0^{\text{lab}} = 2L$ and hence with minimum initial potential energy) or above the second carbon

[1]The timestep was estimated as one tenth of the characteristic time of the fastest motion in the system, corresponding in this case to the oscillation of C atoms, since characteristic frequencies of He and H_2O (estimated as the frequency associated with the average energy jump between the lowest and the following band) are of $\mathcal{O}(10\,\text{THz})$, i.e. much smaller than $\omega = 79.936\,\text{THz}$, hence providing longer timesteps (whose magnitude is larger than 10 fs).

[2]The error associated with this parameter was estimated to be of 0.004 Å.

Table 3.1: Values of parameters of the model considered in BOMDs.

L (Å)	Δ (Å)	V_0 (meV)	ω (THz)	$K = M\omega^2/4$ (N/m)	x_0^{lab} (Å)	N
2.462	0.568	$0.005 \div 1.0$	79.936	31.859	$1.5L$, $2L$	10, 20

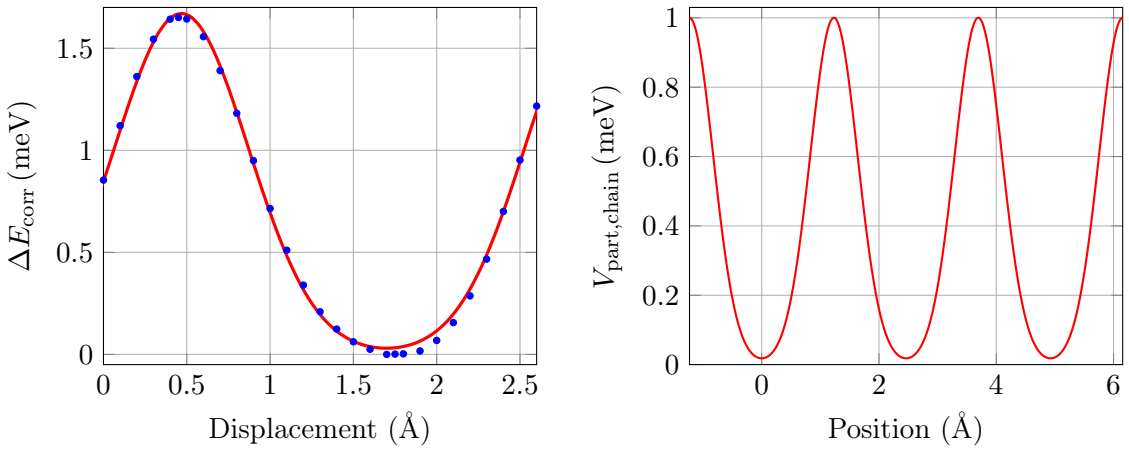

(a) *Ab-initio* data (in blue) of water-(5, 5) CNT corrugation potential (obtained with PBE-D2 functional, see **Chapter 4**) with the water dipole rotated by $-48°$ with respect to the CNT axis and corresponding fitting function (2.3) (in red) for $L = 2.462\,\text{Å}$ and $\Delta = 0.568\,\text{Å}$

(b) Plot of particle-chain interaction potential (2.3) for $L = 2.462\,\text{Å}$, $\Delta = 0.568\,\text{Å}$ and $V_0 = 1.0\,\text{meV}$

Figure 3.1

(namely at $x_0^{\text{lab}} = 1.5L$ with maximum initial potential energy), in both cases with a non-zero initial velocity; C atoms instead were always initialized at rest in their equilibrium lattice position.

3.1.2 Choice of the flowing particle

As previously stated, both single helium atoms and water molecules can exhibit superflow inside a (5, 5) armchair CNT [6, 7]; nevertheless, given that:

1. the aim of this study is identifying possible sources of dissipation coming into play during the flow, meaning that we are interested just in global trends and not in precise values;

2. He bands are more parabolic and hence associated with higher flow velocities (obtained as band slope), as one can see in **Figure 2.3**;

3. in these BOMDs helium and water differ just by their mass m since the interaction with the chain is modeled in the same way (V_0 will be treated as a variable parameter);

BOMDs were performed here adopting He as the reference flowing particle. However in the end, for physically relevant results these simulations will be repeated with a water molecule and with realistic parameters estimated in **Chapter 4** to verify such findings.

3.2 Harmonicity and anharmonicity

In this first case, Newton's equations were solved employing the velocity Verlet integrator [12], exposed in **Appendix B.2**. This algorithm was chosen first of all because it is symplectic, i.e. it conserves the energy of the system under analysis when integrating its equations of motion. Moreover, if compared to the original Verlet integrator [13], velocity Verlet equations are numerically more stable on computers with finite precision, even though mathematically equivalent. [12]

In order to better interpret our results for this kind of BOMDs, we considered the reference frame of the center of mass (CM), unless differently stated; indeed, if we were in the laboratory frame we would see the motion of the particles in the CM reference frame superposed to the one of the CM (which is uniform).

Galileian transformations performed from the laboratory to the CM reference frame are

$$\begin{cases} X^{\mathrm{CM}}(t) = X^{\mathrm{lab}}(t) - (V_{\mathrm{CM}}t + X_{\mathrm{CM}}(0)) \\ V^{\mathrm{CM}}(t) = V^{\mathrm{lab}}(t) - V_{\mathrm{CM}} \end{cases} , \tag{3.1}$$

where superscripts denote the corresponding reference frame; $V_{\mathrm{CM}} = \frac{m}{M_{\mathrm{tot}}} v_0^{\mathrm{lab}}$ is the CM velocity (since only the particle has a non-zero initial velocity and since no external forces are acting on the total system) and $M_{\mathrm{tot}} = m + NM$ is the total mass of the system.

3.2.1 Preliminary checks

First of all, so as to ensure energy conservation, it was always checked that total energy percentage wise fluctuations $\Delta E_{\mathrm{tot},\%}$ with respect to the mean $\bar{E}_{\mathrm{tot}}$

$$\Delta E_{\mathrm{tot},\%}(t) = \frac{E_{\mathrm{tot}}(t) - \bar{E}_{\mathrm{tot}}}{\bar{E}_{\mathrm{tot}}} \times 100 \tag{3.2}$$

were below the threshold of 0.01 % in module, as shown in **Figure 3.2a**. Moreover, it was always verified that no artificial external contributions were acting on the system by checking that the center of mass motion was uniform and consequently by ensuring its position remained constant in its reference frame. $X_{\mathrm{CM}}^{\mathrm{CM}}$ fluctuations were indeed found to have an upper limit of $\mathcal{O}(10^{-9}\,\text{Å})$ and were attributed to numerical noise associated with finite precision. An example can be seen in **Figure 3.2b**.

Then an analysis of the effect of timestep duration dt was carried out. In the harmonic case (anharmonic contributions will be introduced later), dt solely affects percentage wise fluctuations of particle's maximum velocity $\Delta v_{\%}$ with respect to v_0^{lab} (see later), of particle's minimum velocity with respect to v_0^{lab} and of the total energy $\Delta E_{\mathrm{tot},\%}$; these quantities increase as dt increases (except for minimum velocity fluctuations, which vary without following any specific trend with dt). Also the behaviour of $\Delta E_{\mathrm{tot},\%}$ with the timestep was checked: using series expansion of position and velocity shown in **Appendix B.2** one obtains

$$E_{\mathrm{tot}}(t+dt) = E_{\mathrm{tot}}(t) + dt \sum_i v_i(t) \left[\frac{1}{2} F_i(t) + \frac{1}{2} F_i(t+dt) + \frac{\partial E_{\mathrm{pot}}}{\partial x_i}(\{x_j(t)\}) \right] + \mathcal{O}(dt^2)\,, \tag{3.3}$$

in which $F_i(t)$ is the force acting on i^{th} particle at time t and $E_{\mathrm{pot}}(\{x_j(t)\})$ system potential energy at the same instant, depending only on particles' positions at time t. However, if the system is subject to only conservative forces, $F_i(t) = -\frac{\partial E_{\mathrm{pot}}}{\partial x_i}(\{x_j(t)\})$ and if a sufficiently small value is taken for dt, the term in square brackets is null or quite small, getting that energy is conserved up to errors of order dt^2, with an expected parabolic trend. This can indeed be seen in **Figure 3.3**, in which data have been fitted in a satisfactory way by quadratic polynomials $ax^2 + bx + c$.

On the other hand, it was discovered that single spring energies, single spring displacements and shape of the total energy of the system are independent of dt. Anyway, the latter is not random but follows a specific, periodic behaviour: indeed, as shown in **Figure 3.4a**, plotting the system total energy together with the rescaled and shifted total potential energy E_{pot} (which is sum of the particle-chain interaction energy E_{int} and of springs' elastic energies) one can see that E_{tot} follows the periodicity of E_{pot} (which coincides with the periodicity of E_{int}) and that some relative points of the total energy correspond to minima and maxima of the interaction potential. Remaining relative points are due to the sum of functions representing profiles of total potential and total kinetic energies[3], as one would expect from the definition of total mechanical energy and as illustrated in **Figure 3.4b**.

However, it was observed that replacing double precision values with single precision ones in the code of BOMDs led to fluctuations $\Delta E_{\mathrm{tot},\%}$ with a different shape (and also with a different and larger order of magnitude). With double precision, even decreasing dt down to 1×10^{-8} fs, these fluctuations did not disappear, as instead one would expect. From these two observations one could infer that total energy percentage wise fluctuations may be mainly numerical noise fluctuations associated with computer finite precision.

[3] This was checked for different values of x_0^{lab} and Δ.

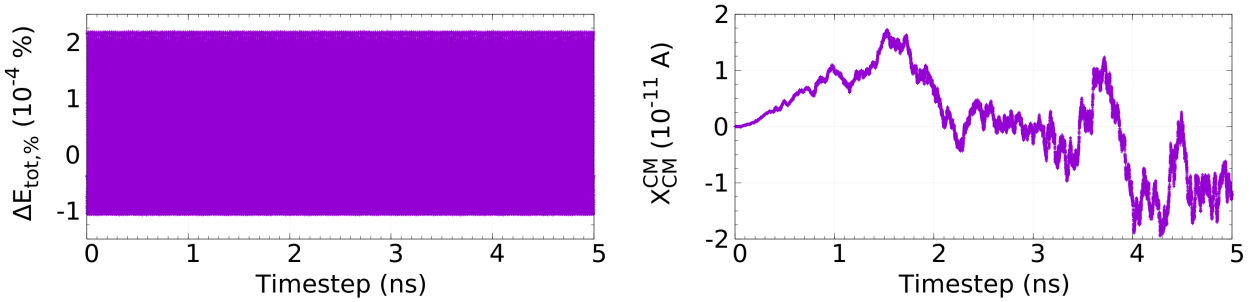

(a) Total energy percentage wise fluctuations, always below the threshold of 0.01 % in module

(b) Center of mass position in its reference frame: fluctuations are deemed to be caused by numerical noise related to finite precision

Figure 3.2: Quantities used for preliminary checks in BOMDs, showing that total energy is conserved and that the center of mass stays fixed in time (except for numerical noise associated with finite precision); these data were obtained with $V_0 = 0.1\,\text{meV}$, $v_0^{\text{lab}} = 630\,\text{m/s}$ and $x_0^{\text{lab}} = 2L$.

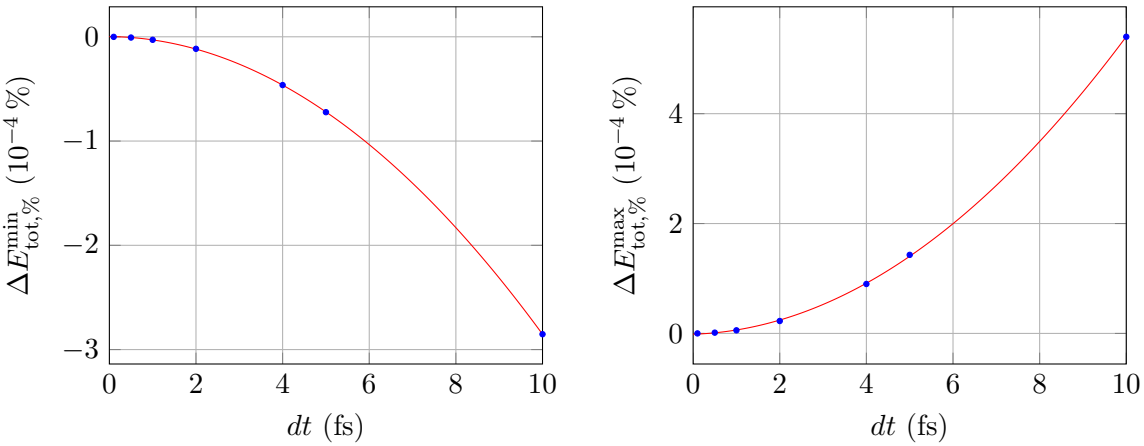

Figure 3.3: Plots of minima and maxima of percentage wise total energy fluctuations $\Delta E_{\text{tot},\%}$ at different timestep lengths dt for $v_0^{\text{lab}} = 30\,\text{m/s}$ and $x_0^{\text{lab}} = 2L$ in the harmonic case. Each set of data is fitted with a quadratic polynomial $ax^2 + bx + c$ in a satisfactory way, as expected theoretically.

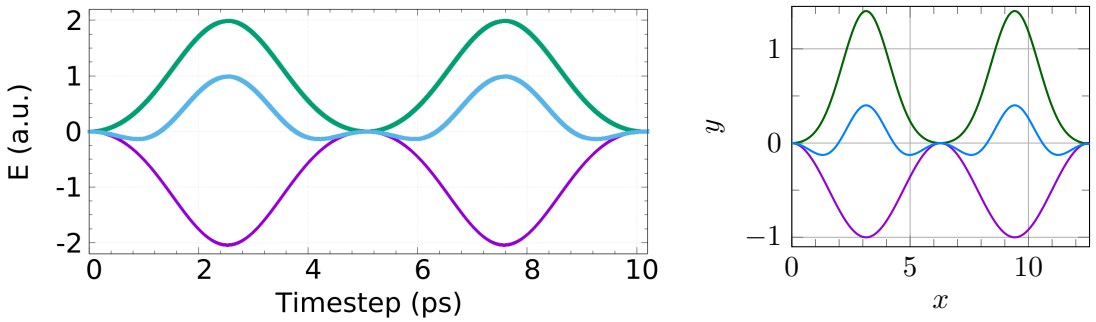

(a) Comparison of rescaled data for total kinetic energy E_{kin} (in violet), total potential energy E_{pot} (in green) and total mechanical energy E_{tot} (in light blue)

(b) Functions used to represent simulation data: the violet line was obtained fitting the total kinetic energy E_{kin}, the green line fitting the total potential energy E_{pot} and the light blue line is the sum of the two, hence representing total mechanical energy E_{tot}; this plot shows how relative points of E_{tot} not present in E_{pot} come from the sum of functional profiles of total kinetic and total potential energy

Figure 3.4

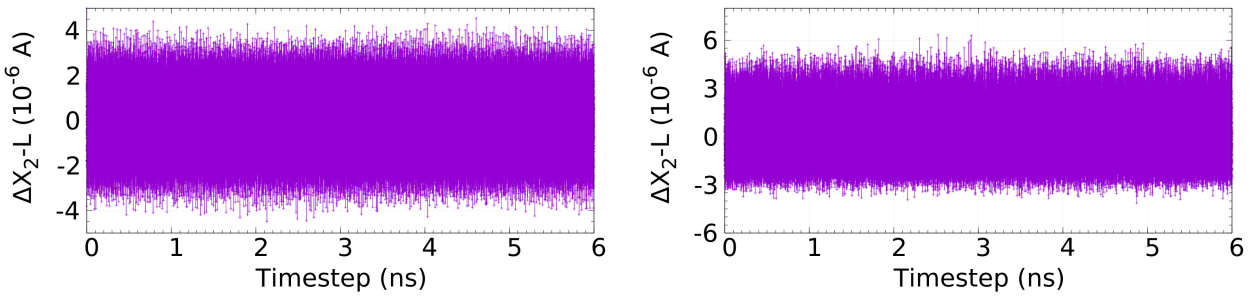

(a) Harmonic case **(b)** Anharmonic case

Figure 3.5: Displacement of the second spring in absence of the flowing particle and of its Gaussian interaction; both harmonic and anharmonic cases are considered, with an initial displacement of 5.0×10^{-6} Å. These plots were found to be in agreement with what expected theoretically from **Figure 3.6**.

3.2.2 Code reasonableness

In order to assess the reasonableness of the employed code, periodic chain dynamics were studied in absence of the particle and of its periodic Gaussian interaction, with both harmonic and anharmonic contributions. Anharmonic terms can be introduced in the Hamiltonian of the system as follows:

$$\begin{cases} H_{\text{chain}}^{\text{harm}} = \sum_{n=1}^{N} \frac{P_n^2}{2M} + \frac{M\omega^2}{8} \sum_{\substack{n=1 \\ n\,\text{per}}}^{N} (X_n - X_{n-1} - L)^2 \\ H_{\text{chain}}^{\text{anharm}} = K_3 \sum_{\substack{n=1 \\ n\,\text{per}}}^{N} (X_n - X_{n-1} - L)^3 + K_4 \sum_{\substack{n=1 \\ n\,\text{per}}}^{N} (X_n - X_{n-1} - L)^4 \\ H_{\text{chain}} = H_{\text{chain}}^{\text{harm}} + H_{\text{chain}}^{\text{anharm}} \end{cases} . \tag{3.4}$$

In these expressions quartic terms are also retained for two reasons: first of all because an Hamiltonian with only cubic terms (even though small enough to be considered small perturbations) is unstable; secondly, because conservation laws often impose rather stringent restrictions on processes produced by cubic terms and hence these third-order processes are so few that their transition rates are comparable with those of four-phonon processes, even though the latter is smaller [9].

BOMDs of the carbons alone were studied and, in order to keep the CM at rest and have $E_{\text{tot}}^{\text{chain}} = E_{\text{pot},0}^{\text{chain}}$, just the second carbon of the chain was displaced from its equilibrium position by 5.0×10^{-6} Å with null initial velocity (consequently, just second and third springs have a non-zero energy since they are the only ones affected by this displacement). It was found that, with just pure harmonicity, displacements of a single spring $\Delta X_n - L$ (with $\Delta X_n = X_n - X_{n-1}$) were symmetric (as shown in **Figure 3.5a**) and in discrete agreement with those expected theoretically considering the initial potential energy of the chain (which coincides with its total energy), as illustrated in **Figure 3.6** by the red plot and by the orange line. Introducing anharmonic coefficients $(K_3, K_4) = (-6.0 \times 10^{16}\,\text{N/m}^2, 1.0 \times 10^{32}\,\text{N/m}^3)$, chosen because they produce an appreciable variation in the shape of spring elastic energy, springs' displacements became asymmetric instead, as one can see in **Figure 3.5b**, and still in agreement with the corresponding predictions (black line in **Figure 3.6**). Discrepancies can be explained with the fact that the second spring was not isolated and hence redistributed its initial potential energy with the others through excitation of vibrational modes.

3.2.3 Code stability

While performing BOMDs with anharmonic terms, it was noticed that, for $v_0^{\text{lab}} = 630\,\text{m/s}$, $(K_3, K_4) = (-6.0 \times 10^{16}\,\text{N/m}^2, 1.0 \times 10^{32}\,\text{N/m}^3)$, $N = 20$, $dt = 1.0\,\text{fs}$ and a duration of 5×10^6 timesteps, after approximately 2 208 340 steps all quantities become "NaN". So as to assess the stability of the code, this simulation was repeated with the same parameters just listed but using single precision and with 10 carbons in the chain with both precisions. It was observed that in all four cases there is a specific timestep at which physically relevant quantities (e.g. positions, velocities, accelerations and

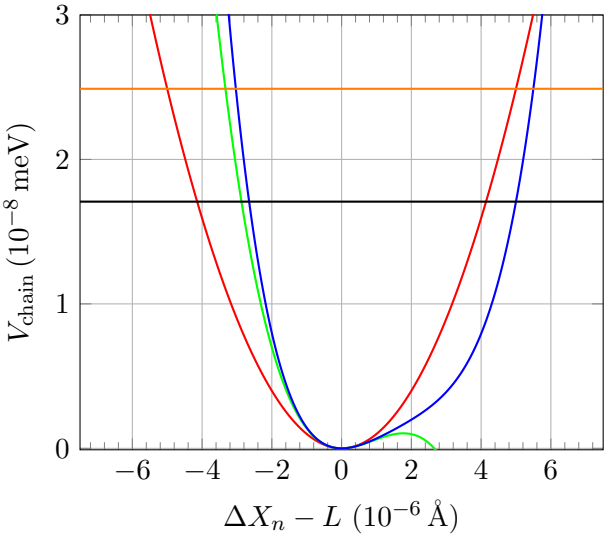

Figure 3.6: Plots of the potential of the n^{th} spring between two adjacent atoms of the carbon chain alone for anharmonic coefficients $(K_3, K_4) = (-6.0\times10^{16}\,\text{N/m}^2, 1.0\times10^{32}\,\text{N/m}^3)$: the red plot is the harmonic potential, the green one presents the additional K_3 contribution and the blue one represents the potential with also the K_4 term; the orange line represents the initial potential energy of the second spring in the harmonic case and the black one its initial potential energy in the anharmonic case, both for an initial displacement of 5.0×10^{-6} Å.

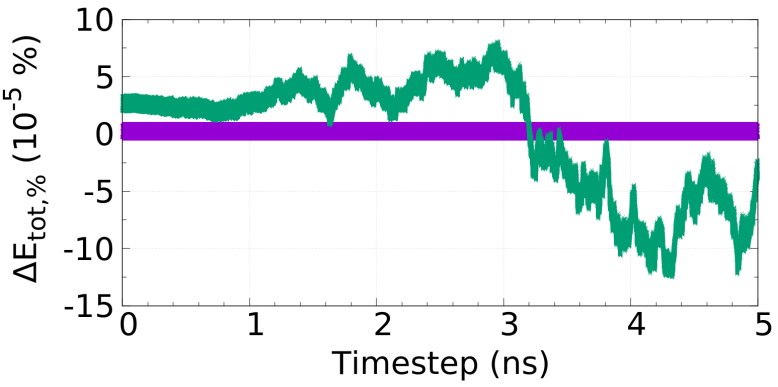

Figure 3.7: Comparison of total energy percentage wise fluctuations between the original Verlet algorithm [13] (in green) and the velocity one [12] (in violet) in the harmonic case for $v_0^{\text{lab}} = 630\,\text{m/s}$, $V_0 = 0.1\,\text{meV}$, $x_0^{\text{lab}} = 2L$ and $dt = 0.6\,\text{fs}$: as one can see, in both cases energy is conserved but velocity Verlet integrator provides stabler fluctuations (the same occurs with the center of mass position X_{CM}^{CM}).

energies) become anomalous, i.e. start differing largely from the values assumed until that step, and that this anomaly emerges sooner if single precision is used and later if less carbons are considered; such an anomaly is then followed by "NaN" values. A closer inspection showed that this anomaly followed by "NaN" values solely affects the chain, since particle's quantities do not present any deviation from usual values (obviously until "NaN" values occur). Furthermore, the cause could not be the particle, since its energy was still finite while the chain's one became anomalous (meaning that no abnormal energy transfer between the two occurred), neither could be functions used in the *Fortran* code (i.e. *dnint* and *dexp*), since "NaN" values were returned only after their appearance in other physical quantities. It was also noticed that the larger the helium initial velocity was, the sooner the anomaly appeared. On the other hand, "NaN" appeared later if dt was decreased and anomalies were absent if only harmonic terms were present.

In order to understand whether the employed velocity Verlet algorithm could be responsible for the observed anomaly, some simulations were performed using also the original Verlet algorithm [13], which is explained in **Appendix B**: first of all, in absence of anharmonicity the total energy was still conserved but original Verlet integrator provided total energy fluctuations which were more chaotic than those obtained with its velocity version, as one can see from **Figure 3.7**; also CM position fluctuations were larger, since $X_{\mathrm{CM}}^{\mathrm{CM}}$ deviated from 0 up to $\mathcal{O}(10^{-5}\,\text{Å})$. Nevertheless, using the same values of the parameters that caused the appearance of "NaN" with velocity Verlet algorithm, one finds that the aforementioned anomalies occur at larger times; this however is not regarded to be a good enough reason to use original Verlet integrator in place of the velocity one, since the same result (i.e. a delay in the onset of these anomalies) can be achieved reducing the timestep.

Based on these observations, such anomalies are regarded to be caused by the accumulation of numerical errors related to the finite precision in the representation and to the integration step dt; these anomalies are also deemed to be amplified by the large anharmonic coefficients used. It was also observed that anomalies correlated with unphysical crossing between C atoms within the chain. In practice, accumulation of numerical noise can eventually lead to unphysical configurations. These can be avoided in any case by a suitable choice of the timestep.

3.2.4 Analysis of results

After these checks, dynamical simulations were interpreted from a physical point of view and particularly interesting quantities were studied varying available parameters.

System dynamics

With initial conditions $v_0^{\mathrm{lab}} \lesssim \sqrt{\frac{2V_0}{m}}$ and x_0^{lab} situated between two C atoms, the particle oscillates between the same two atoms since the corresponding potential barrier is too high (i.e. the particle is confined); if instead the particle has sufficient velocity, or equivalently x_0^{lab} is on top of one of the carbons, the barrier is overcome and the particle moves along the chain (whose atoms move or oscillate in the opposite direction with respect to the particle). Such dynamics are shown in **Figure 3.8** in the harmonic case for $V_0 = 0.1\,\text{meV}$ and $0.5\,\text{meV}$, for different values of v_0^{lab} and either with $x_0^{\mathrm{lab}} = 2L$ or $1.5L$. These behaviours occur both with and without anharmonic contributions, but the introduction of anharmonicity causes in general a phase shift in positions, velocities and energies (as one can see for example in **Figure 3.9a**) and makes oscillations more chaotic for both velocities and energies, as shown in **Figure 3.9b**.

Moreover, in the anharmonic case carbon velocities' oscillation amplitude increases compared to the harmonic case (see **Figure 3.9c** for instance), while helium velocity presents oscillations that decrease with time; these observations can be explained in terms of an enhancement of helium-chain energy exchange when anharmonicity is considered (see below).

Dissipation curves

Other two relevant differences arising when anharmonic contributions are taken into account are the disappearance of periodicity in helium maximum velocity percentage wise fluctuations $\Delta v_{\%}$ (see

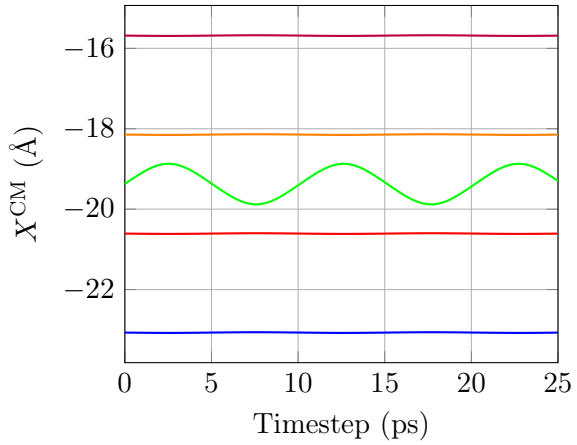

(a) $(V_0, v_0^{\mathrm{lab}}, x_0^{\mathrm{lab}}) = (0.1\,\mathrm{meV}, 30\,\mathrm{m/s}, 2L)$

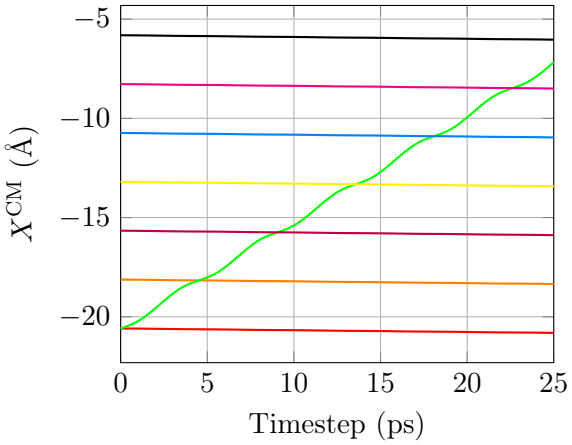

(b) $(V_0, v_0^{\mathrm{lab}}, x_0^{\mathrm{lab}}) = (0.1\,\mathrm{meV}, 30\,\mathrm{m/s}, 1.5L)$

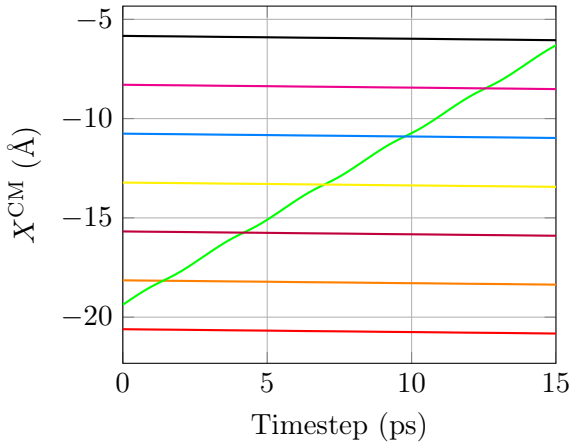

(c) $(V_0, v_0^{\mathrm{lab}}, x_0^{\mathrm{lab}}) = (0.1\,\mathrm{meV}, 100\,\mathrm{m/s}, 2L)$

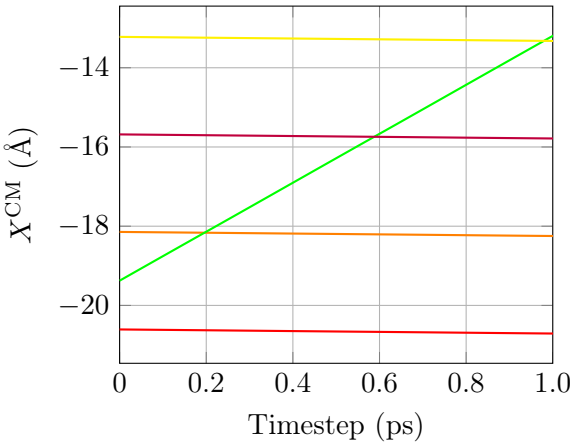

(d) $(V_0, v_0^{\mathrm{lab}}, x_0^{\mathrm{lab}}) = (0.1\,\mathrm{meV}, 630\,\mathrm{m/s}, 2L)$

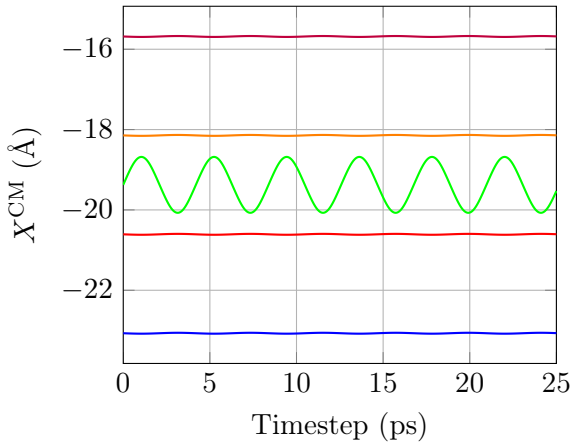

(e) $(V_0, v_0^{\mathrm{lab}}, x_0^{\mathrm{lab}}) = (0.5\,\mathrm{meV}, 100\,\mathrm{m/s}, 2L)$

Figure 3.8: Plots of carbon atoms and helium particle positions during BOMDs in the harmonic case: green lines correspond to He position, while other colored lines to carbon ones; in particular, blue lines (i.e. the lowest ones) are associated with the first C, red lines with the second, orange lines with the third and so on. These BOMDs were performed for different values of the triplet $(V_0, v_0^{\mathrm{lab}}, x_0^{\mathrm{lab}})$ and are in agreement with classical mechanics expectations.

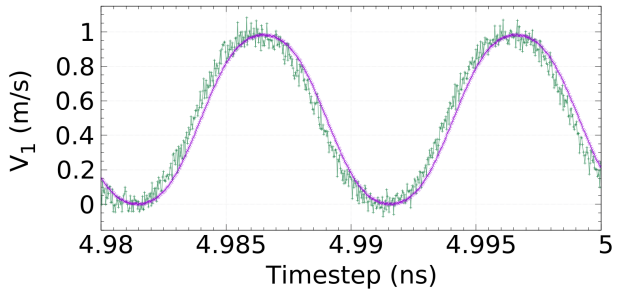

(a) Comparison of the first carbon atom velocity V_1 between the harmonic (in violet) and the anharmonic (in green) case towards the end of a 5 ns-long simulation at $(V_0, v_0^{\text{lab}}, x_0^{\text{lab}}) = (0.1\,\text{meV}, 30\,\text{m/s}, 2L)$. This behaviour occurs also at 630 m/s

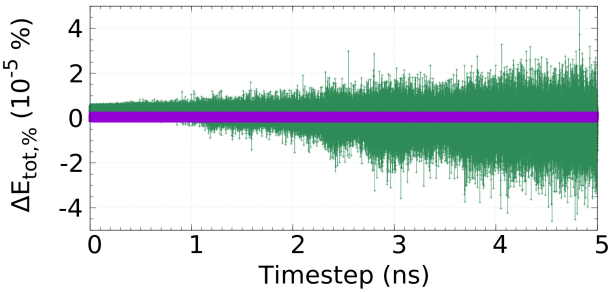

(b) Comparison of total energy percentage wise fluctuations $\Delta E_{\text{tot},\%}$ between the harmonic (in violet) and anharmonic (in green) case at $(V_0, v_0^{\text{lab}}, x_0^{\text{lab}}) = (0.1\,\text{meV}, 30\,\text{m/s}, 2L)$. This behaviour occurs also at 630 m/s

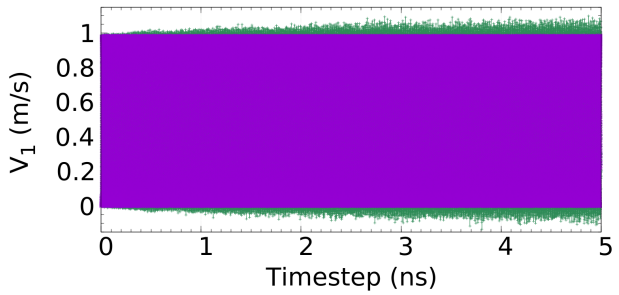

(c) Comparison of the first carbon atom velocity V_1 between the harmonic (in violet) and the anharmonic (in green) case at $(V_0, v_0^{\text{lab}}, x_0^{\text{lab}}) = (0.1\,\text{meV}, 30\,\text{m/s}, 2L)$. This behaviour occurs also at 630 m/s

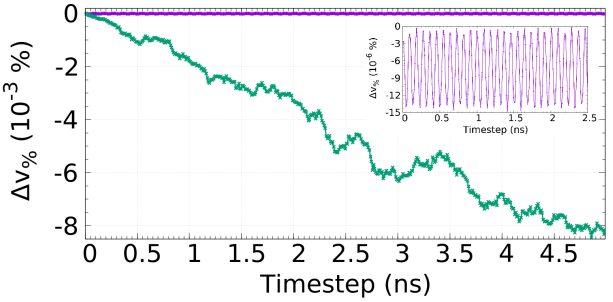

(d) Comparison of helium maximum velocity fluctuations $\Delta v_{\%}$ between the harmonic (in violet) and the anharmonic (in green) case at $(V_0, v_0^{\text{lab}}, x_0^{\text{lab}}) = (0.1\,\text{meV}, 30\,\text{m/s}, 2L)$; the inset shows the oscillating harmonic case alone

Figure 3.9: Plots showing the effect of the introduction of anharmonic coefficients $(K_3, K_4) = (-6.0 \times 10^{16}\,\text{N/m}^2, 1.0 \times 10^{32}\,\text{N/m}^3)$, i.e. the presence of a phase shift in positions, velocities and energies, more chaotic oscillations of velocities and energies, a change in velocity oscillation amplitude and an increase in particle-chain energy exchange (with disappearance of periodic oscillations). These data were obtained in 5 ns-long simulations with $dt = 0.6$ fs.

Table 3.2: Values of percentage wise fluctuations $\Delta v_{\%}^{\text{end}}$ and $\Delta E_{\text{He},\%}^{\text{end}}$ in the harmonic and anharmonic case for $(K_3, K_4) = (-6.0 \times 10^{16}\,\text{N/m}^2, 1.0 \times 10^{32}\,\text{N/m}^3)$ and $V_0 = 0.1\,\text{meV}$. Different v_0^{lab} are considered; values shown are taken towards the end of 5 ns-long simulations with $dt = 0.7\,\text{fs}$.

v_0^{lab} (m/s)	$\Delta v_{\%}^{\text{harm,end}}$ (10^{-3} %)	$\Delta v_{\%}^{\text{anharm,end}}$ (10^{-3} %)	$\Delta E_{\text{He},\%}^{\text{harm,end}}$ (10^{-2} %)	$\Delta E_{\text{He},\%}^{\text{anharm,end}}$ (10^{-2} %)
30	-7.0×10^{-3}	-6.7	-2.79×10^{-3}	-1.19
45	-7.1×10^{-3}	-7.6	-1.65×10^{-3}	-1.45
65	-7.0×10^{-3}	-4.5	2.29×10^{-3}	-0.87
100	-6.0×10^{-3}	-5.4	1.46×10^{-3}	-1.04
165	-0.2	-5.3	-5.83×10^{-2}	-1.05
230	-1.7	-2.6	-0.15	-0.49
400	-1.0	-2.1	-5.90×10^{-2}	-0.43
630	-0.3	-1.4	-1.33×10^{-2}	-0.28

later for their definition), which is present instead in the purely harmonic case as shown in the inset of **Figure 3.9d**, and the increase in their magnitude for suitable values of K_3 and K_4, as one can see in the aforementioned figure.

Considering helium energy E_{He} as sum of its kinetic energy and of the particle-chain interaction energy, i.e. as

$$E_{\text{He}} = \frac{1}{2}mv^2 + E_{\text{int}}\,, \tag{3.5}$$

percentage wise fluctuations of helium maximum velocity $\Delta v_{\%}$ and of helium energy transferred to the chain $\Delta E_{\text{He},\%}$ were defined at time t as

$$\begin{cases} \Delta v_{\%} = \frac{v_{\text{max}}^{\text{lab}}(t) - v_0^{\text{lab}}}{v_0^{\text{lab}}} \times 100 \\ \Delta E_{\text{He},\%} = \frac{\bar{E}_{\text{He}}(t) - \bar{E}_{\text{He},0}}{\bar{E}_{\text{He},0}} \times 100 \end{cases} . \tag{3.6}$$

Here $v_{\text{max}}^{\text{lab}}(t)$ is the maximum of helium velocity profile around instant t and $\bar{E}_{\text{He}}(t)$ denotes helium average total energy at that time, i.e. computed from minima and maxima of E_{He} around t; a "0" as subscript denotes that the quantity is taken at the start of the simulation. When these quantities are computed towards the end of a simulation, a subscript "end" is used.

As one can see from data in **Table 3.2**, modules of these quantities are always larger when large anharmonic contributions are introduced; the facts that $\Delta E_{\text{He},\%}^{\text{harm,end}}$ is positive (meaning that energy was transferred from the chain to He) at 65 m/s and 100 m/s and that it has a value almost comparable to the anharmonic one at 230 m/s can be attributed to fluctuations of minima and maxima of E_{He}.

In order to understand how these fluctuations vary with K_3, *dissipation curves* were studied: they consist of $\{(|K_3|, \Delta v_{\%}^{\text{end}})\}$ and $\{(|K_3|, \Delta E_{\text{He},\%}^{\text{end}})\}$ data at fixed V_0 and v_0^{lab}. Since we are interested in the study of a particle flowing inside the CNT, for every value of V_0 (namely 0.1 meV, 0.5 meV and 1.0 meV), values of v_0^{lab} were chosen in the set {100, 190, 230, 400, 630} m/s provided that they allowed the particle to flow. Furthermore, in order to avoid the appearance of previously described "NaN" anomalies due to numerical noise and so as to guarantee energy conservation, timestep duration was progressively decreased with potential barrier height: for $V_0 = 0.1\,\text{meV}$ it was chosen to be 0.6 fs, for $V_0 = 0.5\,\text{meV}$ it was reduced to 0.4 fs and for $V_0 = 1.0\,\text{meV}$ to 0.2 fs.

To construct these dissipation curves, percentage wise fluctuations in (3.6) were considered towards the end of 5 ns-long simulations, deemed to be long enough for relevant He-chain energy exchange to occur. Just as a check, results were compared for different BOMDs durations: as illustrated in **Figure 3.10a** for the case $(V_0, v_0^{\text{lab}}) = (0.1\,\text{meV}, 190\,\text{m/s})$, $\Delta v_{\%}^{\text{end}}$ percentage wise fluctuations (but also $\Delta E_{\text{He},\%}^{\text{end}}$ ones since, as it will be shown later, the two have the same qualitative behaviour) preserve almost the same trend even for longer time lengths, with the magnitude changing slightly in module; this indeed occurs because equilibrium was not reached, and it is neither expected to be reached after longer times, as one can see from **Figure 3.10b**.

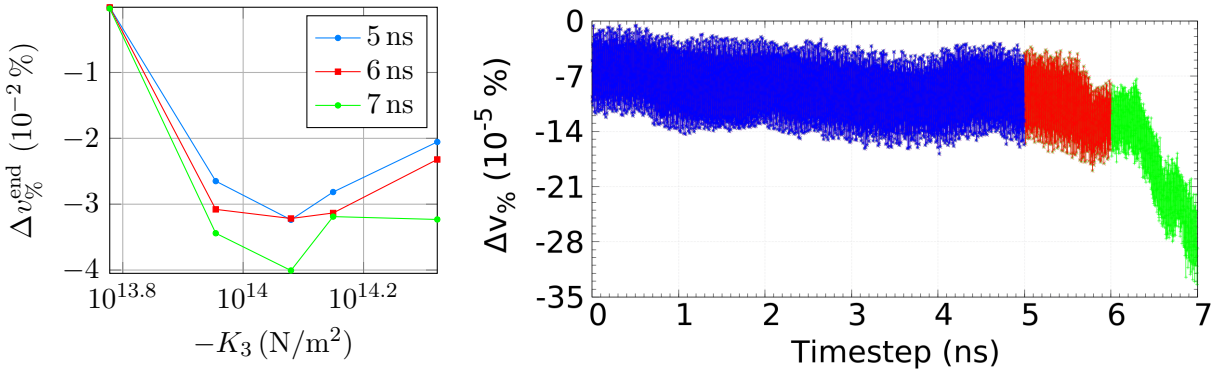

(a) Comparison of dissipation curve details at $(V_0, v_0^{\mathrm{lab}}) = (0.1\,\mathrm{meV}, 190\,\mathrm{m/s})$ for different time durations. Data were acquired towards the end of 5 ns-long simulations

(b) Comparison of maximum particle velocity fluctuations $\Delta v_{\%}$ at $(V_0, v_0^{\mathrm{lab}}) = (0.1\,\mathrm{meV}, 190\,\mathrm{m/s})$ for different time durations: blue points correspond to 5 ns, red ones to 6 ns and green ones to 7 ns

Figure 3.10: Comparison of dissipation curve details and $\Delta v_{\%}$ at $(V_0, v_0^{\mathrm{lab}}) = (0.1\,\mathrm{meV}, 190\,\mathrm{m/s})$ for different time durations, showing that in dissipation curves the trend is almost the same even for longer durations and that in BOMDs an equilibrium is not reached.

Dissipation curves for $V_0 = 0.1\,\mathrm{meV}$ are shown in **Figure 3.11**: first of all one can notice how $\Delta v_{\%}^{\mathrm{end}}$ and $\Delta E_{\mathrm{He},\%}^{\mathrm{end}}$ have the same qualitative behaviour but different magnitudes. As K_3 decreases in module, both percentage wise fluctuations decrease (i.e. there is an increase in the loss of velocity and energy, transferred from He to chain), reaching an absolute minimum; then they increase, until the harmonic regime is recovered. One can notice the presence of irregularities, that were checked not to be an artifact of simulations by reducing dt: as illustrated in **Figure 3.12** (in which just velocity fluctuations are considered since the trend is the same), decreasing the timestep length does not remove such irregularities, that slightly reduce or increase their height, except for the case at $v_0^{\mathrm{lab}} = 400\,\mathrm{m/s}$, at which the peak disappears for $dt = 0.5\,\mathrm{fs}$.

An interesting feature to notice is that the absolute minimum of these dissipation curves seems to decrease as v_0^{lab} increases, meaning that the larger the initial velocity the higher the maximum amount of velocity and energy that can be transferred from He to the chain, even if such minimum occurs at different K_3.

Concerning higher values of the potential barrier, one can see from **Figure 3.13a** and **Figure 3.13b** that dissipation curves follow the same qualitative behaviour as those at $V_0 = 0.1\,\mathrm{meV}$, with anomalous peaks appearing just for $v_0^{\mathrm{lab}} = 400\,\mathrm{m/s}$ at 0.5 meV and for 630 m/s at 1.0 meV. As previously noticed, as v_0^{lab} increases keeping V_0 fixed, the maximum transfer of velocity and energy increases, occurring however at smaller values of $|K_3|$; this trend occurs also increasing the potential amplitude V_0 while keeping v_0^{lab} fixed, as can be seen comparing these curves with those in **Figure 3.11**.

Thus, these dissipation curves effectively showed how anharmonic contributions in a given range can cause a significant increase in particle-chain transfer of velocity and energy with respect to the purely harmonic case; these exchanges are also not monotonic with $|K_3|$. The comparison also showed how one cannot identify a precise trend of $\Delta v_{\%}^{\mathrm{end}}$ (or $\Delta E_{\mathrm{He},\%}^{\mathrm{end}}$) with v_0^{lab} at fixed $(|K_3|, V_0)$ due to the complexity of dissipation curve profiles.

3.3 Viscous contributions

In the previous section anharmonicity was observed to enhance the amount of velocity and energy transferred from the flowing particle to the chain. Now it is interesting to study energy dissipation in the CNT. Such dissipation is meant to effectively mimic possible radiative decays or couplings to the environment. The question is whether continuous energy losses in the CNT can favour energy transfer from the flowing particle to the CNT, with consequent enhancement of friction forces.

With this aim, in order to reduce the average lifetime of CNT vibrations (consequently preventing

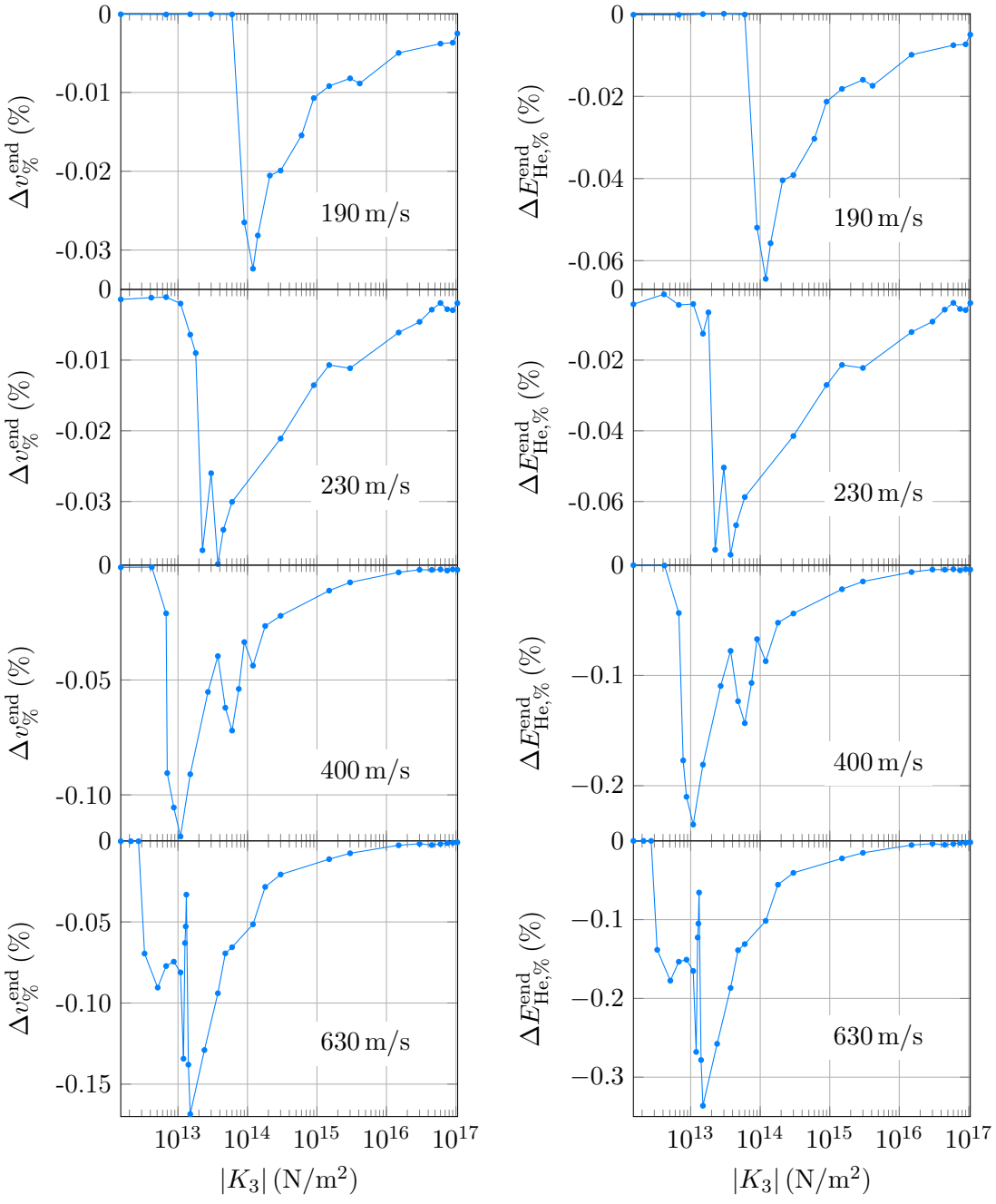

(a) $\{(|K_3|, \Delta v_{\%}^{\mathrm{end}})\}$ data **(b)** $\{(|K_3|, \Delta E_{\mathrm{He},\%}^{\mathrm{end}})\}$ data

Figure 3.11: Dissipation curves in terms of $\Delta v_{\%}^{\mathrm{end}}$ and $\Delta E_{\mathrm{He},\%}^{\mathrm{end}}$ at different fixed velocities for constant ratio $K_3/K_4 = -6.0 \times 10^{-16}$ m and $V_0 = 0.1$ meV. Data were acquired towards the end of 5 ns-long simulations with $dt = 0.6$ fs and are shown with a logarithmic x-axis. The absolute minimum decreases with v_0^{lab}.

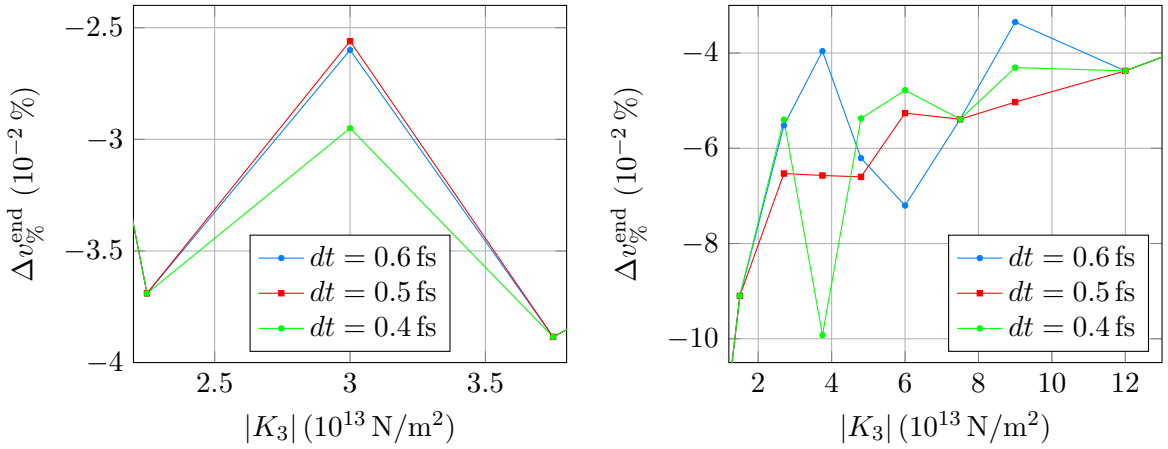

(a) $v_0^{\mathrm{lab}} = 230\,\mathrm{m/s}$ **(b)** $v_0^{\mathrm{lab}} = 400\,\mathrm{m/s}$

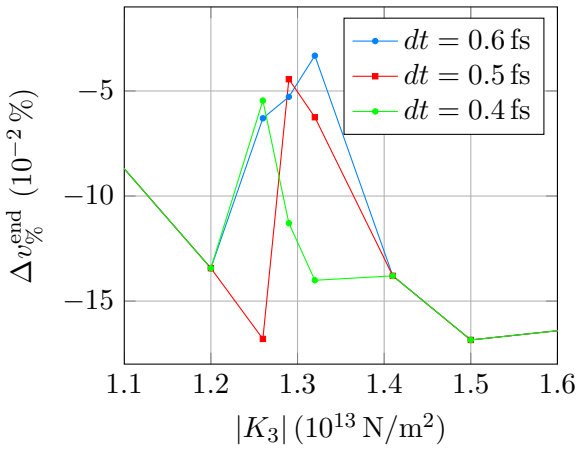

(c) $v_0^{\mathrm{lab}} = 630\,\mathrm{m/s}$

Figure 3.12: Irregularities in $\Delta v_{\%}^{\mathrm{end}}$ dissipation curves of **Figure 3.11** for different values of dt at $V_0 = 0.1\,\mathrm{meV}$. These data were acquired towards the end of 5 ns-long simulations and show that, except for the case at $v_0^{\mathrm{lab}} = 400\,\mathrm{m/s}$, decreasing the timestep length does not remove irregularities, which just slightly reduce or increase their height. The same occurs for $\Delta E_{\mathrm{He},\%}^{\mathrm{end}}$.

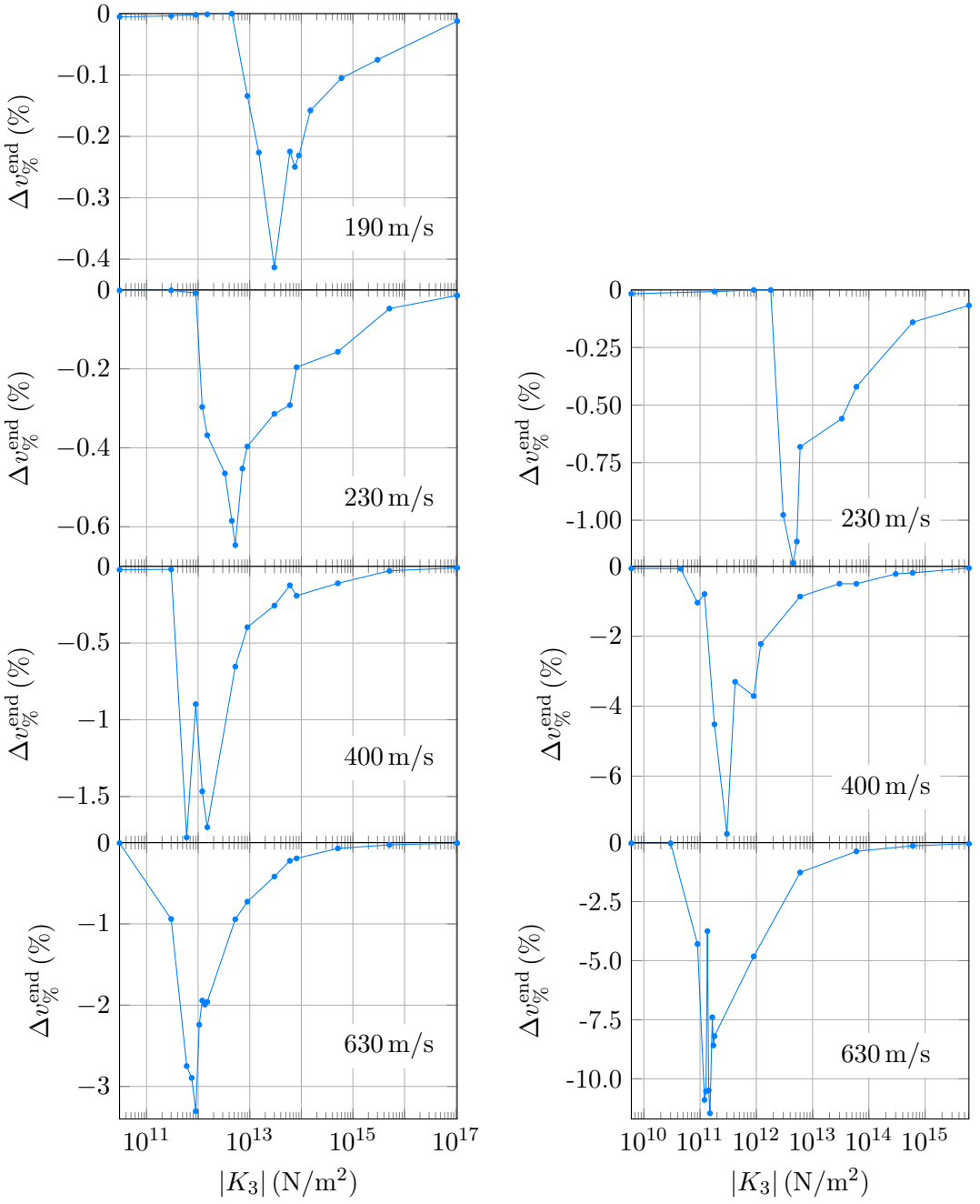

(a) $\{(|K_3|, \Delta v_{\%}^{\mathrm{end}})\}$ data for $V_0 = 0.5\,\mathrm{meV}$ and $dt = 0.4\,\mathrm{fs}$

(b) $\{(|K_3|, \Delta v_{\%}^{\mathrm{end}})\}$ data for $V_0 = 1.0\,\mathrm{meV}$ and $dt = 0.2\,\mathrm{fs}$

Figure 3.13: Dissipation curves in terms of $\Delta v_{\%}^{\mathrm{end}}$ at different fixed velocities for constant ratio $K_3/K_4 = -6.0 \times 10^{-16}\,\mathrm{m}$ and $V_0 = \{0.5, 1.0\}\,\mathrm{meV}$. Data were acquired towards the end of 5 ns-long simulations and are shown with a logarithmic x-axis. The absolute minimum decreases with v_0^{lab}. The same trends (with different magnitudes) were observed for the corresponding $\Delta E_{\mathrm{He},\%}^{\mathrm{end}}$ dissipation curves.

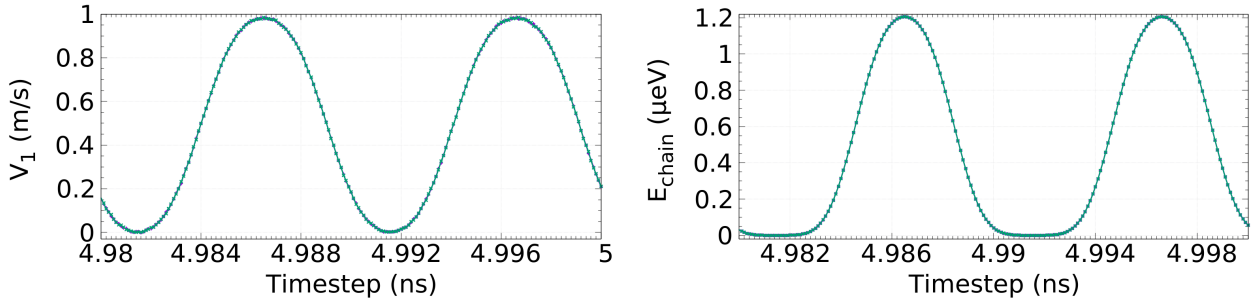

(a) Comparison of the first carbon atom velocity V_1 in the harmonic case between the velocity Verlet integrator (in violet) and the Fourth order Runge-Kutta algorithm (in green) at $v_0^{\text{lab}} = 30\,\text{m/s}$ towards the end of a 5 ns-long simulation. This behaviour occurred also at 630 m/s, but with larger discrepancies

(b) Comparison of the chain total energy E_{chain} in the harmonic case between the velocity Verlet integrator (in violet) and the Fourth order Runge-Kutta algorithm (in green) at $v_0^{\text{lab}} = 30\,\text{m/s}$ towards the end of a 5 ns-long simulation. This behaviour occurred also at 630 m/s, but with larger discrepancies

Figure 3.14: Plots showing the comparison of different quantities in the harmonic undamped case between velocity Verlet and Fourth order Runge-Kutta integrators. These data were obtained in simulations with $V_0 = 0.1\,\text{meV}$ and $x_0^{\text{lab}} = 2L$. As one can see, trends are the same, assessing the reasonableness of the employed Runge-Kutta algorithm.

them from persisting for the whole trajectory), viscous contributions of the kind $-\zeta V_i$ were added in the i^{th} equation of motion of the chain, ζ being a positive damping coefficient and V_i the velocity of the i^{th} carbon atom. However, the previously employed velocity Verlet algorithm could not be used anymore, since it is symplectic, while in this case energy is not conserved; the integrator had to be changed also because (as one can see from (B.5) in **Appendix B.2**) to obtain the i^{th} carbon velocity at time $t + dt$ the corresponding acceleration at time $t + dt$ is required, but such acceleration now needs the unknown velocity $V_i(t + dt)$ in order to be computed. To overcome this problem the Fourth order Runge-Kutta algorithm [14, 15] was used, whose equations are exposed in **Appendix B.3**.

Proceeding as in the case of the velocity Verlet integrator, first of all the reasonableness of the code was checked comparing Runge-Kutta harmonic dynamics in absence of viscous coefficient with velocity Verlet ones in **Section 3.2** for $x_0^{\text{lab}} = 2L$ and $dt = 1.0\,\text{fs}$, whose reasonableness was already assessed. First of all, we defined the percentage wise difference of a quantity Q (either the position or the velocity) between its velocity Verlet and Runge-Kutta versions at the same time t as

$$\Delta Q_{\text{comparison},\%}(t) = \frac{Q_{\text{VV}}(t) - Q_{\text{RK}}(t)}{Q_{\text{VV}}(t)} \times 100\,, \tag{3.7}$$

$Q_{\text{VV}}(t)$ being the velocity Verlet version of Q at time t and $Q_{\text{RK}}(t)$ the corresponding Runge-Kutta one. For $v_0^{\text{lab}} = 30\,\text{m/s}$ we observed that positions differed in module at max by $1.5 \times 10^{-4}\,\%$, while for $v_0^{\text{lab}} = 630\,\text{m/s}$ the module of these percentage wise differences was $\lesssim 5 \times 10^{-3}\,\%$. Also velocities presented a good agreement, exhibiting the same trend in both cases with what was deemed to be a satisfactory overlap, as exposed for instance in **Figure 3.14a**. As for the total energy, its behaviour was different since Runge-Kutta algorithm is not symplectic; nevertheless, magnitudes were comparable. Moreover, the trend of chain total energy was exactly the same at 30 m/s, as shown in **Figure 3.14b**, while for 630 m/s values were slightly different but positions of minima and maxima almost coincided. These observations were deemed enough to certify the reasonableness of this new integrator.

In order to study the general behaviour of particles in viscous molecular dynamics, a reference value of the damping coefficient was estimated based on characteristic quantities of the system under analysis, i.e. the initial helium velocity v_0^{lab} and the carbon mass M, and it was chosen in such a way that the viscous force was comparable with the average carbon acceleration without damping, i.e.

$$\zeta v_0^{\text{lab}} \sim M\mathcal{O}(a_{\text{C}}^{\max})\,, \tag{3.8}$$

$a_{\text{C}}^{\max}$ being the maximum value of the acceleration of a carbon of the chain in absence of viscous coefficients. This estimate yielded the value of $\mathcal{O}(10^{-16}\,\text{kgs}^{-1})$, which is comparable with estimates provided by Ref. [16] and Ref. [17], i.e. $1.0 \times 10^{-17}\,\text{kgs}^{-1}$ and $1.0 \times 10^{-15}\,\text{kgs}^{-1}$ respectively.

3.3.1 Viscous dynamics

Focusing only on cases with $x_0^{\text{lab}} = 2L$ since they are the most interesting ones, using the reference value $\zeta = 1.0 \times 10^{-16}\,\text{kgs}^{-1}$ and the reference pair of anharmonic coefficients $(K_3, K_4) = (-6.0 \times 10^{16}\,\text{N/m}^2, 1.0 \times 10^{32}\,\text{N/m}^3)$, viscous dynamics were studied in the harmonic and anharmonic case for $V_0 = 0.1\,\text{meV}$, $dt = 1.0\,\text{fs}$, $x_0^{\text{lab}} = 2L$ (i.e. He starts between the second and the third carbon atom) and v_0^{lab} both equal to 30 m/s and 630 m/s. At variance with what done with velocity Verlet results, now the analysis is carried out in the laboratory reference frame.

For $v_0^{\text{lab}} = 30\,\text{m/s}$ in the harmonic case, after an initial drift (deemed to be caused by the dissipation of the CM initial velocity due to viscous contributions) both carbon and helium atoms oscillate with oscillations that get damped with time, as one can see in **Figure 3.15a**; the same damping occurs also to velocities (see, for instance, **Figure 3.15b**). Hence, if the initial energy of the flowing particle is not high enough to overcome the energy barrier, this remains confined between two carbons (as shown in **Figure 3.15c**), oscillating with a progressively decreasing amplitude. The He energy decreases with time (**Figure 3.15d**); also $\Delta v_{\%}$ decreases but with a much stronger rate (**Figure 3.15e**) compared to the undamped case, in which periodic oscillations are present. If anharmonicity is introduced, position, velocity and He energy behaviours are the same, but the phase shift seen in the undamped case occurs here too; it has to be pointed out that $\Delta v_{\%}^{\text{anharm}}$ and E_{He} are slightly smaller (see for instance **Figure 3.15f**), meaning that more velocity and energy are transferred or lost in presence of anharmonic terms. Instead, E_{chain} will be studied later separately.

For $v_0^{\text{lab}} = 630\,\text{m/s}$ in the harmonic case, from **Figure 3.16a** one can see how, for large enough times, the position of the carbon atoms do not oscillate anymore around zero but around a straight linear trajectory with finite positive small slope, while the coordinate of He keeps growing with a slope which slightly reduces with time due to the energy exchange with the chain (see the corresponding inset). Velocities oscillate around a non-zero value with an almost constant amplitude after a first transient, as illustrated, for instance, in **Figure 3.16b**: this is deemed to occur because, after a first gain, energy dissipation occurs due to viscous contributions until a quasi-stationary state is reached. As it happens for $v_0^{\text{lab}} = 30\,\text{m/s}$, both $\Delta v_{\%}$ and E_{He} do not oscillate anymore (at variance with corresponding undamped cases) but decrease, as it can be seen in **Figure 3.16c**. The introduction of anharmonic contributions causes fluctuations to become more chaotic and, as for energy and velocity exchange, for the considered values of ζ and V_0 the particle loss becomes greater (see **Figure 3.16d** as an example).

From these observations, it seems that if the initial energy of helium is not sufficient to overcome the energy barrier, damped oscillations occur; if instead the initial energy is high enough, the particle flows with v that decreases while carbon velocities stabilize after a transient. This stabilization can be seen computing the percentage wise ratio between carbons' average acceleration and the corresponding amplitude for $v_0^{\text{lab}} = 630\,\text{m/s}$:

$$r_{i,\%} = \frac{\bar{A}_i}{A_{A_i}} \times 100\,, \tag{3.9}$$

$\bar{A}_i$ being the i^{th} carbon atom average acceleration and A_{A_i} its corresponding acceleration amplitude after the transient (i.e. approximately after 1.5 ns). It was found that their modules lay in the range $[1 \times 10^{-4}; 2 \times 10^{-3}]\%$, meaning that carbon average accelerations are approximately null.

3.3.2 Effects of viscous contributions

In this part of the thesis work the effect of viscous contributions was characterized by studying the behaviour of the already presented particle maximum velocity percentage wise fluctuations $\Delta v_{\%}^{\text{end}}$ and of chain total energy percentage wise fluctuations $\Delta E_{\text{chain},\%}$ at the end of simulations; the latter is defined as

$$\Delta E_{\text{chain},\%}^{\text{end}} = \frac{\bar{E}_{\text{chain}}(t_{\text{end}}) - \bar{E}_{\text{chain},0}}{\bar{E}_{\text{chain},0}} \times 100\,, \tag{3.10}$$

in which $\bar{E}_{\text{chain}}(t)$ is the average energy of the chain obtained averaging minima and maxima around time t and a "0" as subscript denotes that the energy is taken at the start of the simulation. These two kinds of percentage wise fluctuations were studied for different values of the four parameters characterizing the system, i.e. the chain damping coefficient ζ, the third order anharmonic coefficient

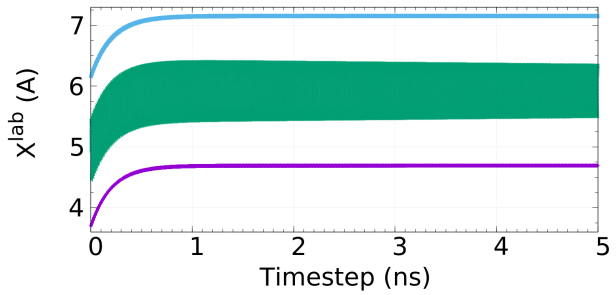

(a) Comparison of positions of the second carbon atom X_2 (in violet), of the He particle x (in green) and of the third carbon atom X_3 (in light blue) in the harmonic case

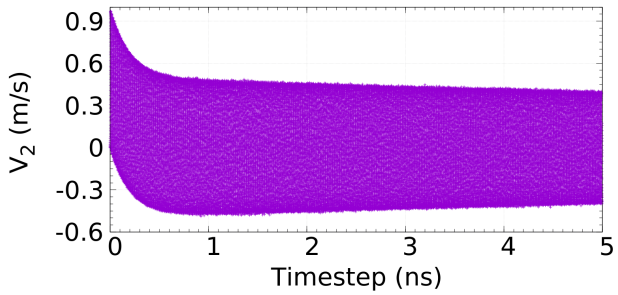

(b) Plot of the velocity of the second carbon atom V_2 in the harmonic case

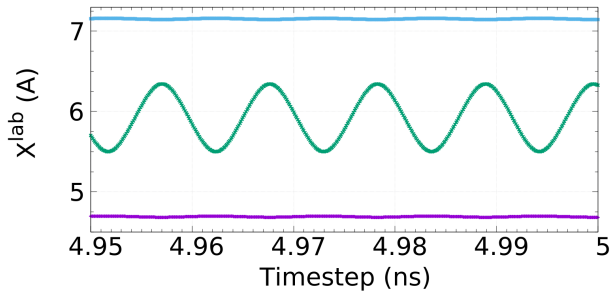

(c) Comparison of positions of the second carbon atom X_2 (in violet), of the He particle x (in green) and of the third carbon atom X_3 (in light blue) in the harmonic case at the end of a 5 ns-long simulation

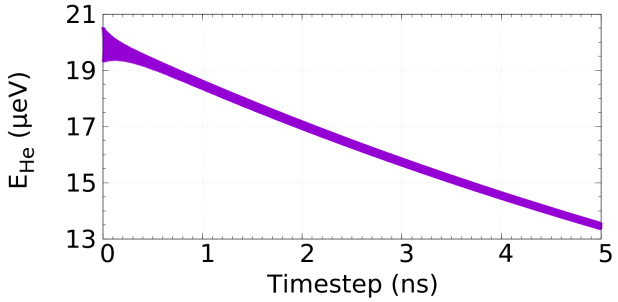

(d) Plot of helium total energy E_{He} in the harmonic case

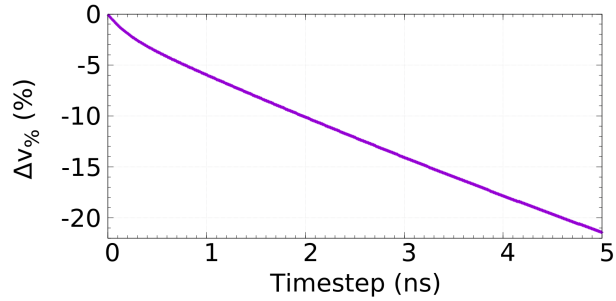

(e) Plot of particle maximum velocity fluctuations $\Delta v_{\%}$ in the harmonic case

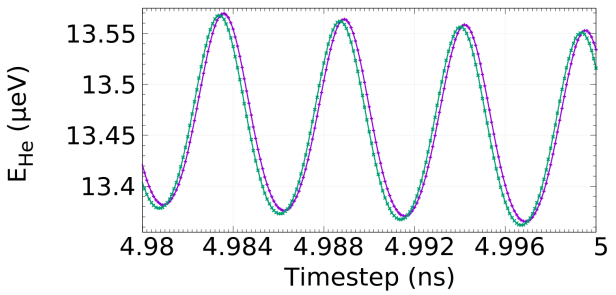

(f) Comparison of helium total energy E_{He} between the harmonic case (in violet) and the anharmonic one (in green) at the end of a 5 ns-long simulation

Figure 3.15: Plots showing quantities associated with system damped harmonic dynamics and comparing them with the corresponding anharmonic case. These data were obtained in 5 ns-long simulations for $\zeta = 1.0 \times 10^{-16}\,\mathrm{kgs}^{-1}$ and $(dt, V_0, x_0^{\mathrm{lab}}, v_0^{\mathrm{lab}}) = (1.0\,\mathrm{fs}, 0.1\,\mathrm{meV}, 2L, 30\,\mathrm{m/s})$ and show how, if v_0^{lab} is small enough, the particle is confined and exhibits both damped oscillations and enhanced monotonic particle-chain energy and velocity exchange (slightly increased in presence of suitable anharmonicity).

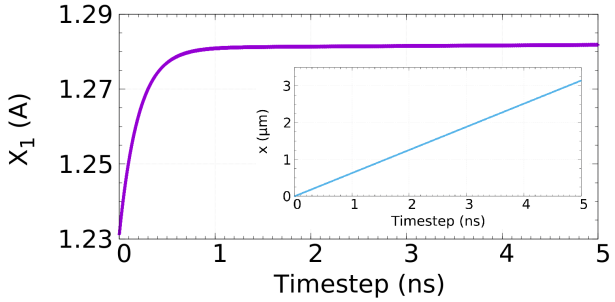

(a) Plot of the position of the first carbon atom X_1 in the harmonic case. The inset shows in light blue the position of the helium particle x in the same case

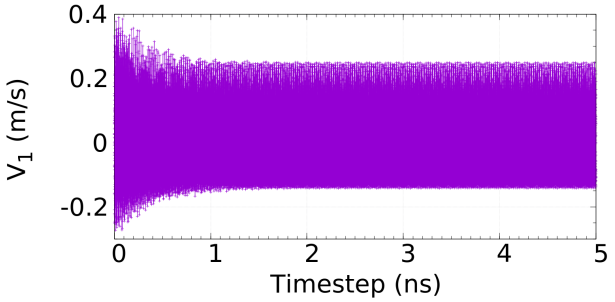

(b) Plot of the velocity of the first carbon atom V_1 in the harmonic case

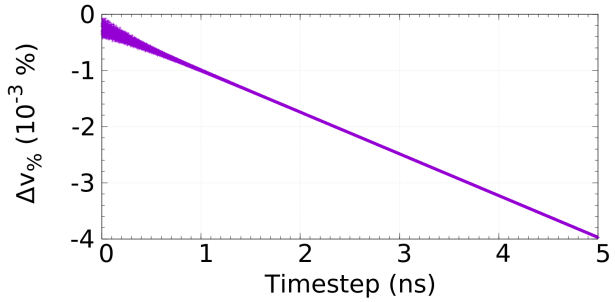

(c) Plot of particle maximum velocity fluctuations $\Delta v_{\%}$ in the harmonic case

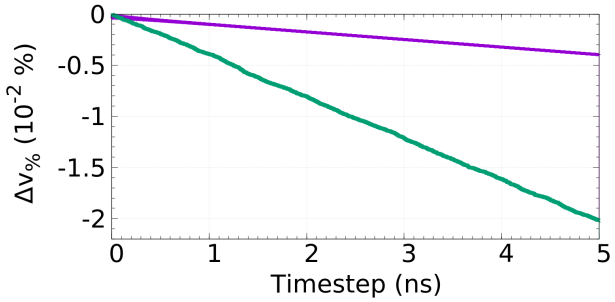

(d) Comparison of particle maximum velocity fluctuations $\Delta v_{\%}$ between the harmonic case (in violet) and the anharmonic one (in green)

Figure 3.16: Plots showing quantities associated with system damped harmonic dynamics and comparing them with the corresponding anharmonic case. These data were obtained in 5 ns-long simulations for $\zeta = 1.0 \times 10^{-16}\,\mathrm{kgs}^{-1}$ and $(dt, V_0, x_0^{\mathrm{lab}}, v_0^{\mathrm{lab}}) = (1.0\,\mathrm{fs}, 0.1\,\mathrm{meV}, 2L, 630\,\mathrm{m/s})$ and show how the particle can flow with an enhanced and monotonic particle-chain energy and velocity exchange, increased when suitable anharmonic coefficients are included.

Table 3.3: Values of parameters $(\zeta, K_3, V_0, v_0^{\text{lab}})$ employed in simulations used to characterize effects of viscous contributions.

	ζ (kgs^{-1})	K_3 (N/m^2)	V_0 (meV)	v_0^{lab} (m/s)
Value 1	0.0	0.0	0.1	100
Value 2	1.0×10^{-16}	-5.4×10^{13}	0.5	190
Value 3	1.0×10^{-12}	-6.0×10^{16}	1.0	230
Value 4	–	–	–	400
Value 5	–	–	–	630

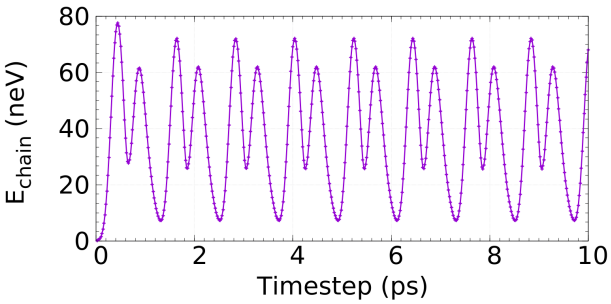

Figure 3.17: Example of chain total energy E_{chain} initial increase during the first picoseconds, deemed to correspond to the activation of vibrational modes. This plot was realized for $(\zeta, K_3, V_0, v_0^{\text{lab}}) = (1.0 \times 10^{-12}, -5.4 \times 10^{13}, 0.5, 230)$.

K_3[4], the potential barrier height V_0 and helium initial velocity in the laboratory reference frame v_0^{lab}. For each of these parameters at least three values were always considered, as shown in **Table 3.3**: in particular, the value $K_3 = -5.4 \times 10^{13}\,\text{N/m}^2$ was chosen as a possible realistic estimate of the anharmonicity of a $(5,5)$ carbon nanotube at zero temperature, as shown in **Appendix C**. It has to be pointed out that not all values of v_0^{lab} were used at every V_0: being interested only in flowing particles, we considered only initial velocities which allowed the particle to flow over the chain for that specific value of the barrier. Moreover, simulations with these values of parameters were always performed with a timestep $dt = 0.2\,\text{fs}$, since it was the interval that guaranteed numerically stable results in the previous study of undamped dissipation curves for every V_0.

However, before studying possible trends of $\Delta v_{\%}^{\text{end}}$ and $\Delta E_{\text{chain},\%}^{\text{end}}$ for different parameter values, it is interesting to describe the shape of chain total energy with time, so as to better grasp the effects of vibrational mode damping.

E_{chain} shape

First of all, it has to be underlined that the initial energy of the chain was always zero in all simulations, since all C atoms start at rest in their equilibrium position. However, regardless of the value chosen for the four parameters, an energy increase in the first picoseconds was always detected and it is deemed to correspond to the activation of vibrational modes due to the very first interaction of the chain with the He, as illustrated in **Figure 3.17** as an example.

Moving on to the analysis of the shape of chain total energy, in the *undamped case* (i.e. $\zeta = 0$) there are two possibilities:

- one in which minima and maxima remain constant (except for some fluctuations), as shown in **Figure 3.18a**, characteristic of the harmonic case and of the weakly anharmonic one (i.e. $K_3 = -5.4 \times 10^{13}\,\text{N/m}^2$) for the two smallest velocities at $V_0 = 0.1\,\text{meV}$;
- one which is characterized by a net upward drift, as depicted in **Figure 3.18b**, in **Figure 3.18c** and in **Figure 3.18d**, arising in presence of anharmonicity.

[4]The fourth order anharmonic coefficient K_4 was always considered in such a way that the ratio K_3/K_4 was kept fixed at $-6.0 \times 10^{-16}\,\text{m}$.

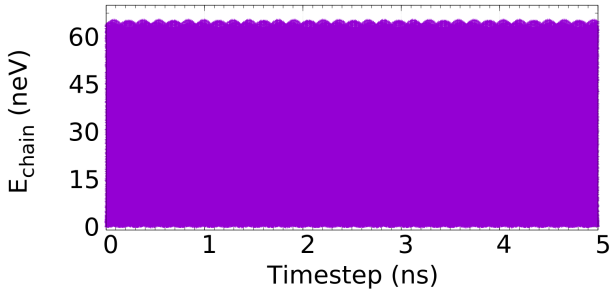

(a) $(\zeta, K_3, V_0, v_0^{\text{lab}}) = (0, 0, 0.1, 190)$. The same result occurs for all possible V_0 in the undamped harmonic case, for $(0, -5.4\times10^{13}, 0.1, 100)$ and $(0, -5.4\times10^{13}, 0.1, 190)$

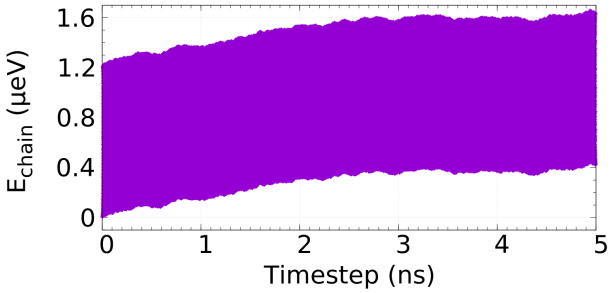

(b) $(\zeta, K_3, V_0, v_0^{\text{lab}}) = (0, -6.0\times10^{16}, 0.5, 230)$. Similar shapes are present in all cases not contemplated in **Figure 3.18a**

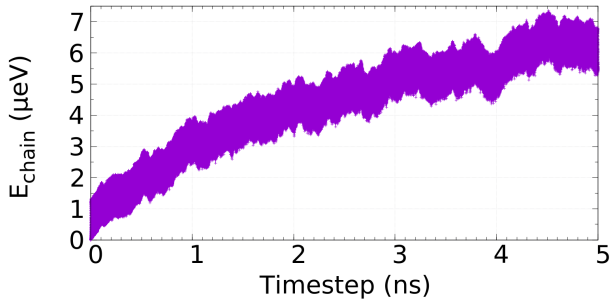

(c) $(\zeta, K_3, V_0, v_0^{\text{lab}}) = (0, -5.4\times10^{13}, 0.5, 230)$. Similar shapes are present in all cases not contemplated in **Figure 3.18a**

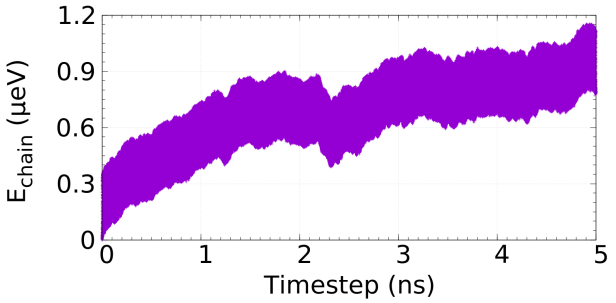

(d) $(\zeta, K_3, V_0, v_0^{\text{lab}}) = (0, -6.0\times10^{16}, 0.5, 400)$. Similar shapes are present in all cases not contemplated in **Figure 3.18a**

Figure 3.18: Examples of E_{chain} shapes in the undamped case (i.e. $\zeta = 0$) for different values of parameters $(\zeta, K_3, V_0, v_0^{\text{lab}})$ (units of measurement are omitted for simplicity).

When $\zeta = 1.0\times10^{-16}$ (corresponding to *weak damping*), two kinds of behaviours can be observed:

- one in which, after a quick and steep increase, the energy starts fluctuating chaotically and irregularly; this is characteristic of the anharmonic case with velocities either 400 m/s or 630 m/s and an example is illustrated in **Figure 3.19a**;
- one, such as the one shown in **Figure 3.19b**, in which, after a transient, chain energy oscillations "stabilize" (except for some fluctuations) and their upper and lower profiles can drift either upwards, downwards or get damped; this occurs with both harmonicity for every velocity and anharmonicity for small velocities.

The *strong damping case* (i.e. $\zeta = 1.0\times10^{-12}\,\text{kgs}^{-1}$) is also rather interesting:

- for $V_0 = 0.1\,\text{meV}$ and for all values of K_3 and v_0^{lab}, the energy oscillates with either an upward or downward drift or with an increase of oscillation amplitude after the initial gain; an example is illustrated in **Figure 3.20a**;
- for $V_0 = 0.5\,\text{meV}$ and for all values of K_3 and v_0^{lab}, a bump appears after an enhancement of oscillations, followed by an important damping of the energy, as it can be seen in **Figure 3.20b**;
- for $V_0 = 1.0\,\text{meV}$ and for all values of K_3 and v_0^{lab}, the aforementioned bump occurs earlier and the damping is more evident when compared to the previous case at the same fixed anharmonicity and velocity; looking at **Figure 3.20c**, the shape of the tail at the end allows to infer that the damping would have continued if simulations had been longer.

Moreover, the insurgence of such a bump corresponds to a change in the behaviour of $\Delta v_{\%}$: comparing **Figure 3.20b** and the violet line in **Figure 3.20d**, one can see how at approximately 1.6 ns there is a change in both plots, with in particular $\Delta v_{\%}$ changing from a linear trend to one in which the velocity decrease rate reduces, since its slope becomes smaller in module with time; the same change occurs at

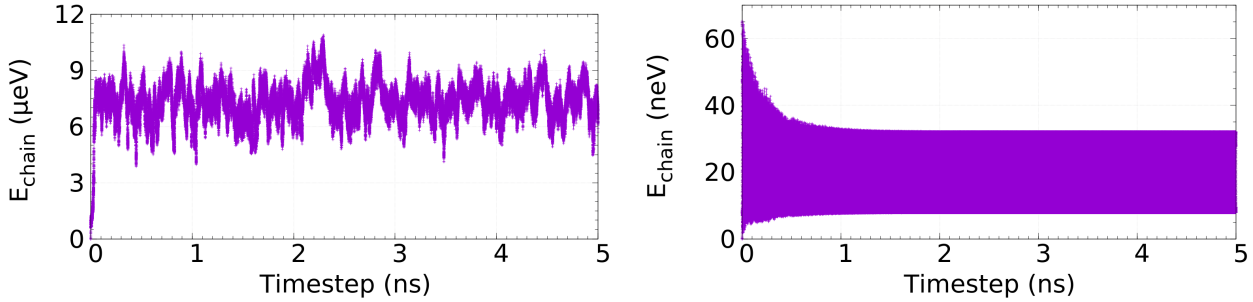

(a) $(\zeta, K_3, V_0, v_0^{\text{lab}}) = (1.0 \times 10^{-16}, -5.4 \times 10^{13}, 0.5, 630)$. The same result occurs at every V_0 for $(\zeta, K_3, v_0^{\text{lab}}) = (1.0 \times 10^{-16}, -5.4 \times 10^{13}, \{400, 630\})$ and $(1.0 \times 10^{-16}, -6.0 \times 10^{16}, 630)$ and at $(\zeta, K_3, V_0, v_0^{\text{lab}}) = (1.0 \times 10^{-16}, -6.0 \times 10^{16}, 0.1, 400)$

(b) $(\zeta, K_3, V_0, v_0^{\text{lab}}) = (1.0 \times 10^{-16}, -5.4 \times 10^{13}, 0.1, 230)$. A similar shape is present in all cases not contemplated in **Figure 3.19a**

Figure 3.19: Examples of E_{chain} shapes in the weakly damped case (i.e. $\zeta = 1.0 \times 10^{-16}\,\text{kgs}^{-1}$) for different values of parameters $(\zeta, K_3, V_0, v_0^{\text{lab}})$ (units of measurement are omitted for simplicity).

approximately 0.1 ns when comparing **Figure 3.20c** and the green line in **Figure 3.20d**. This change can be interpreted as follows: after having gathered velocity (and hence energy) from the flowing particle, the chain starts feeling viscous effects more strongly, with a fast damping of its energy and a slowdown in He-chain energy exchange. Furthermore, it was noticed that keeping V_0 and v_0^{lab} fixed, the height of this bump decreases when $|K_3|$ increases; vice versa, when keeping K_3 and v_0^{lab} constant an increase of V_0 causes a rise in the bump height; if instead V_0 and K_3 are fixed, the bump shifts rightwards as v_0^{lab} is increased, as illustrated in **Figure 3.20e**. In **Figure 3.20f** the comparison of $\Delta v_{\%}$ corresponding to data in **Figure 3.20e** is illustrated, showing how increasing v_0^{lab} causes also a rightward shift of the onset of deviation from linear behaviour. To our current knowledge, such a particular delay in energy dissipation has never been detected before in scientific literature.

$\Delta v_{\%}^{\text{end}}$ study

Percentage wise fluctuations of the maximum of He velocity were studied at the end of 5 ns-long simulations as a function of v_0^{lab}, V_0 and ζ; the trend with K_3 was not considered since it was previously shown in undamped dissipation curves how the dependence on anharmonicity is quite complex and changes significantly with other parameters.

While no peculiar trends were observed for data $\{(v_0^{\text{lab}}, \Delta v_{\%}^{\text{end}})\}$ (as one could have expected given the results of undamped dissipation curves), it was found out that $\Delta v_{\%}^{\text{end}}$ decreases both with ζ at fixed $(K_3, V_0, v_0^{\text{lab}})$ (except for $(-5.4 \times 10^{13}\,\text{N/m},\ 0.1\,\text{meV},\ 230\,\text{m/s})$) and with V_0 at constant $(\zeta, K_3, v_0^{\text{lab}})$ (except for $(0,\ 0,\ 230\,\text{m/s})$), as illustrated in **Figure 3.21**.

This means that the velocity (and hence the energy) exchange is enhanced if either the viscosity in $\text{C}-\text{C}$ bonds or the barrier height is increased. These results could be especially relevant when the radius of the armchair nanotube is decreased while keeping all the other parameters fixed, since, as it is described in **Subsection 4.2.2** for $(5, 5)$ and $(7, 7)$ CNTs, decreasing chiral coefficients causes an increase of the corrugation in the interface potential. Given the physical importance of this finding, these BOMDs were repeated for a water molecule with realistic parameters shown in **Table 4.2** from *ab-initio* calculations, confirming the observed trends.

$\Delta E_{\text{chain},\%}^{\text{end}}$ study

First of all, it has to be pointed out that these percentage wise fluctuations can be both positive (particularly common in the undamped case) or negative. Performing simulations with all possible combinations of values listed in **Table 3.3**, the following peculiar trends of $\Delta E_{\text{chain},\%}^{\text{end}}$ were identified:

1. an increase with v_0^{lab} for every fixed (ζ, K_3) pair when $V_0 = 1.0\,\text{meV}$, for every (ζ, V_0) pair when $K_3 = -6.0 \times 10^{16}\,\text{N/m}^2$ and for (ζ, K_3, V_0) equal to $(\{0, -1.0 \times 10^{-16}\}\,\text{kgs}^{-1}, -5.4 \times$

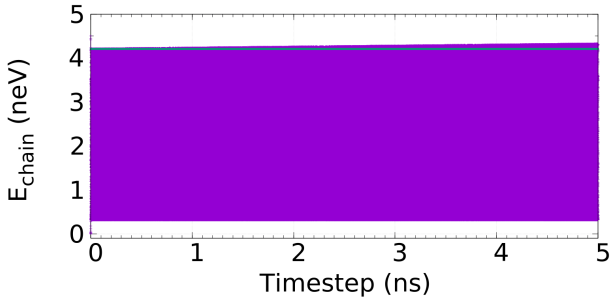

(a) $(\zeta, K_3, V_0, v_0^{\text{lab}}) = (1.0 \times 10^{-12}, -5.4 \times 10^{13}, 0.1, 230)$; the green line is a guide for the eye to understand the increase of oscillation amplitude. A similar shape is present for every K_3 and v_0^{lab} at $(\zeta, V_0) = (1.0 \times 10^{-12}, 0.1)$

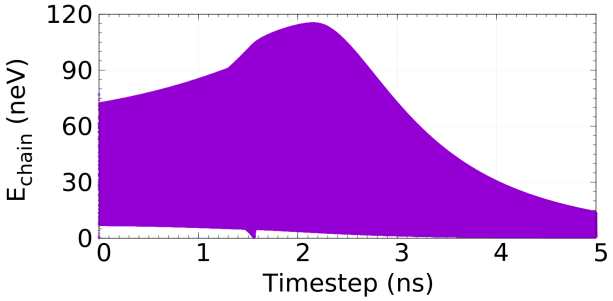

(b) $(\zeta, K_3, V_0, v_0^{\text{lab}}) = (1.0 \times 10^{-12}, -5.4 \times 10^{13}, 0.5, 230)$. Similar shapes occur for every K_3 and v_0^{lab} at $(\zeta, V_0) = (1.0 \times 10^{-12}, 0.5)$

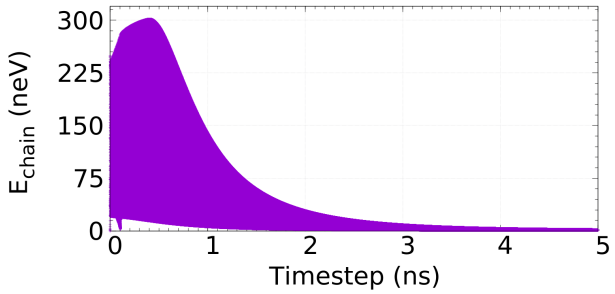

(c) $(\zeta, K_3, V_0, v_0^{\text{lab}}) = (1.0 \times 10^{-12}, -5.4 \times 10^{13}, 1.0, 230)$. Similar shapes occur for every K_3 and v_0^{lab} at $(\zeta, V_0) = (1.0 \times 10^{-12}, 1.0)$

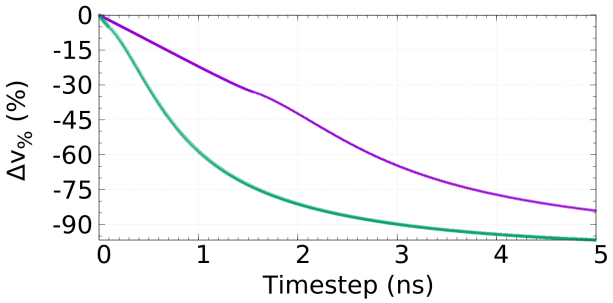

(d) $(\zeta, K_3, V_0, v_0^{\text{lab}}) = (1.0 \times 10^{-12}, -5.4 \times 10^{13}, \{0.5, 1.0\}, 230)$: violet data correspond to $V_0 = 0.5\,\text{meV}$ and green ones to $V_0 = 1.0\,\text{meV}$

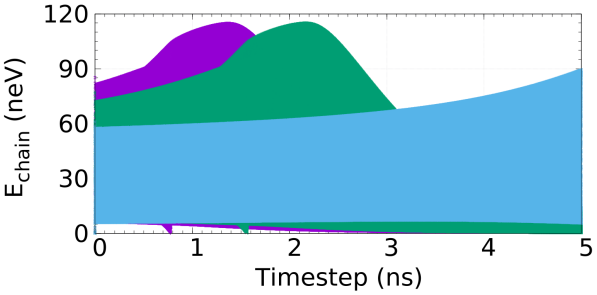

(e) $(\zeta, K_3, V_0, v_0^{\text{lab}}) = (1.0 \times 10^{-12}, -5.4 \times 10^{13}, 0.5, \text{variable})$: violet data correspond to 190 m/s, green ones to 230 m/s and light blue ones to 400 m/s; the larger v_0^{lab} the more shifted rightwards the bump

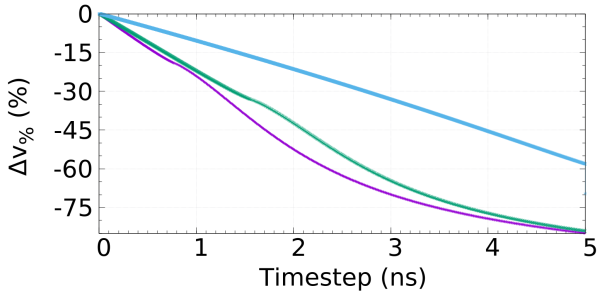

(f) $(\zeta, K_3, V_0, v_0^{\text{lab}}) = (1.0 \times 10^{-12}, -5.4 \times 10^{13}, 0.5, \text{variable})$: violet data correspond to 190 m/s, green ones to 230 m/s and light blue ones to 400 m/s; the larger v_0^{lab} the more shifted rightwards the onset of deviation from linear behaviour

Figure 3.20: Examples of E_{chain} shapes and $\Delta v_{\%}$ in the strongly damped case (i.e. $\zeta = 1.0 \times 10^{-12}\,\text{kgs}^{-1}$) for different values of parameters $(\zeta, K_3, V_0, v_0^{\text{lab}})$ (units of measurement are omitted for simplicity).

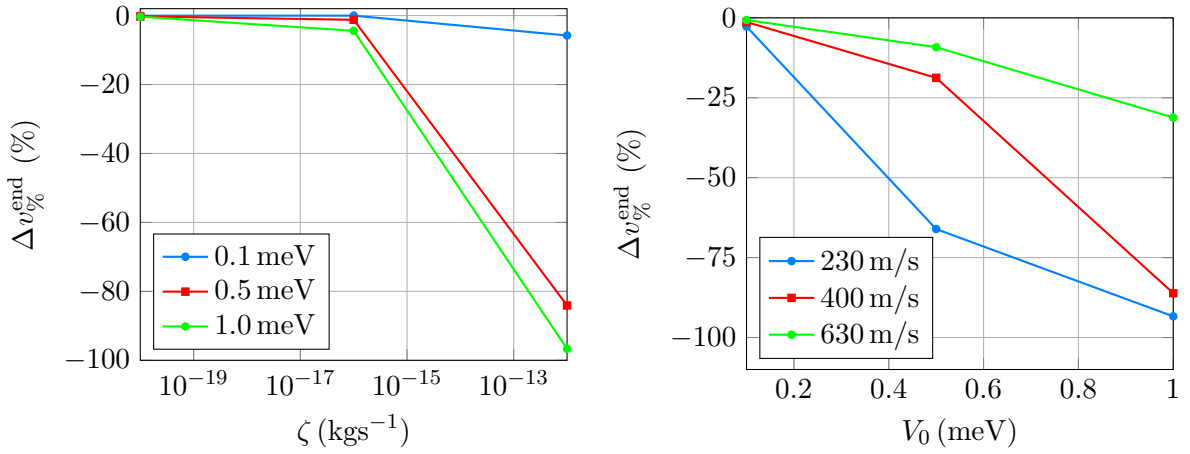

(a) $K_3 = -5.4 \times 10^{13}\,\text{N/m}^2$, different fixed V_0, $v_0^{\text{lab}} = 230\,\text{m/s}$. The same trend is observed at every fixed $(K_3, V_0, v_0^{\text{lab}})$, except for $(-5.4 \times 10^{13}\,\text{N/m}, 0.1\,\text{meV}, 230\,\text{m/s})$

(b) $\zeta = 1.0 \times 10^{-12}\,\text{kgs}^{-1}$, $K_3 = -6.0 \times 10^{16}\,\text{N/m}^2$, different fixed v_0^{lab}. The same trend occurs at every fixed $(\zeta, K_3, v_0^{\text{lab}})$, except for (0, 0, 230 m/s)

Figure 3.21: Examples of peculiar trends of $\Delta v^{\text{end}}_{\%}$ for different values of $(\zeta, K_3, V_0, v_0^{\text{lab}})$. For data points $\{(\zeta, \Delta v^{\text{end}}_{\%})\}$ a logarithmic scale is used and values of the damping coefficient are increased by $1.0 \times 10^{-20}\,\text{kgs}^{-1}$ in order to show also the value corresponding to zero. Velocities here considered always allowed the particle to flow, regardless of the barrier height V_0. Data were acquired towards the end of 5 ns-long simulations with $dt = 0.2\,\text{fs}$ and show an enhancement of particle-chain velocity transfer with ζ and V_0.

$10^{13}\,\text{N/m}^2, 0.5\,\text{meV}$); examples of these behaviours are illustrated in the first three plots of **Figure 3.22** respectively;

2. an increase with $|K_3|$ for every fixed v_0^{lab} at $(\zeta, V_0) = (1.0 \times 10^{-12}\,\text{kgs}^{-1}, 1.0\,\text{meV})$, as shown in **Figure 3.22d**;

3. a decrease with ζ for every fixed (K_3, v_0^{lab}) pair at $V_0 = 1.0\,\text{meV}$ (which pairs with the first trend in 1) and for every $(V_0, v_0^{\text{lab}} \geq 190\,\text{m/s})$ at $K_3 = -5.4 \times 10^{13}\,\text{N/m}^2$ (except for $(0.1\,\text{meV}, \{190, 230\}\,\text{m/s})$), whose examples can be seen in **Figure 3.23a** and **Figure 3.23b** respectively;

4. a decrease with V_0 for every fixed $(\zeta, v_0^{\text{lab}})$ at $K_3 = -6.0 \times 10^{16}\,\text{N/m}^2$ (except for $(1.0 \times 10^{-16}\,\text{kgs}^{-1}, 230\,\text{m/s})$) and for every K_3 at $(\zeta, v_0^{\text{lab}}) = (1.0 \times 10^{-16}\,\text{kgs}^{-1}, 400\,\text{m/s})$ and $(1.0 \times 10^{-12}\,\text{kgs}^{-1}, 230\,\text{m/s})$, as illustrated respectively in **Figure 3.23c** and **Figure 3.23d**.

Looking at these plots, a pattern can be identified: keeping fixed all other parameters, chain energy percentage wise fluctuations tend to increase (namely, less energy is dissipated) if either helium initial velocity v_0^{lab} or anharmonicity $|K_3|$ is increased. Chain energy fluctuations tend instead to decrease (that is, more dissipation occurs) if the damping coefficient or the barrier height is enhanced, as one would expect. Moreover, only the last three enumerated trends find a counterpart in particle maximum velocity percentage wise fluctuations $\Delta v^{\text{end}}_{\%}$. Nevertheless, none of these trends is general, i.e. all of them require at least one of the parameters to be fixed, and hence no extension to all possible values of $(\zeta, K_3, V_0, v_0^{\text{lab}})$ is possible.

In spite of this last observation, these particular trends can still be relevant to understand dissipation mechanisms: supposing that the pair $(K_3, V_0) = (-5.4 \times 10^{13}\,\text{N/m}^2, 0.5\,\text{meV})$ represents realistic values for parameters of our model for a $(5, 5)$ armchair CNT[5], fixing v_0^{lab} and increasing ζ cause a reduction of chain energy percentage wise fluctuations and an increase of dissipation (or, since $\Delta E^{\text{end}}_{\text{chain},\%}$ can also be positive, a decrease in the energy gain from the particle). These trends were confirmed also for a water molecule, by repeating these simulations with values in **Table 4.2**.

[5]Indeed the order of magnitude of K_3 was estimated in **Appendix C** at zero temperature from literature molecular dynamics results, while a similar value of V_0 was estimated in **Subsection 4.2.2**.

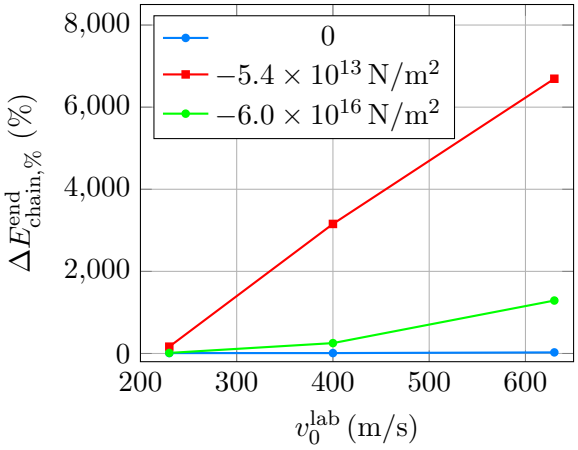

(a) $\zeta = 0$, different fixed K_3, $V_0 = 1.0\,\text{meV}$. The same trend is observed also for every fixed (ζ, K_3) at $V_0 = 1.0\,\text{meV}$

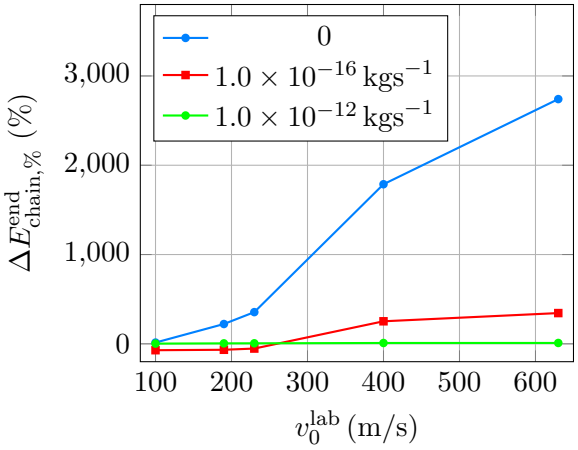

(b) Different fixed ζ, $K_3 = -6.0 \times 10^{16}\,\text{N/m}^2$, $V_0 = 0.1\,\text{meV}$. The same trend is observed also for every fixed (ζ, V_0) at $K_3 = -6.0 \times 10^{16}\,\text{N/m}^2$

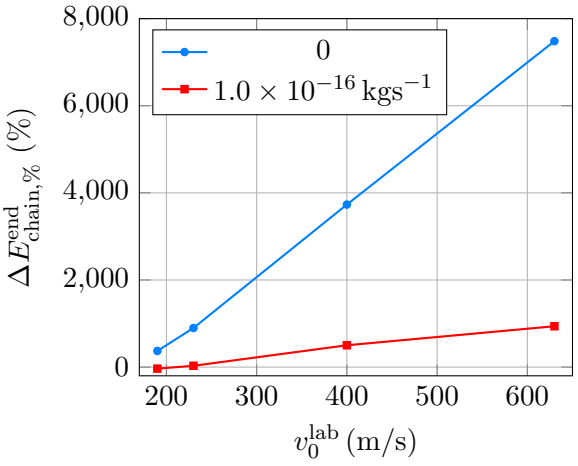

(c) Different ζ, $K_3 = -5.4 \times 10^{13}\,\text{N/m}^2$, $V_0 = 0.5\,\text{meV}$

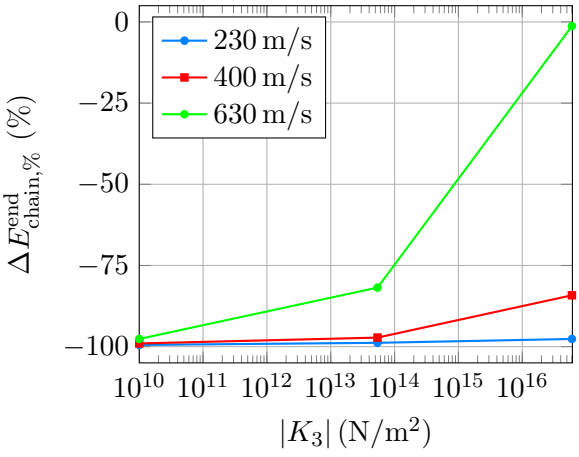

(d) $\zeta = 1.0 \times 10^{-12}\,\text{kgs}^{-1}$, $V_0 = 1.0\,\text{meV}$, different fixed v_0^{lab}

Figure 3.22: Examples of peculiar and common increasing trends of $\Delta E^{\text{end}}_{\text{chain},\%}$ for different values of $(\zeta, K_3, V_0, v_0^{\text{lab}})$. For data points $\{(|K_3|, E^{\text{end}}_{\text{chain},\%})\}$ a logarithmic scale is used and values of the third order anharmonic coefficient are increased by $1.0 \times 10^{10}\,\text{N/m}$ in order to show also the value corresponding to zero. Velocities here considered always allowed the particle to flow, regardless of the barrier height V_0. Data were acquired towards the end of 5 ns-long simulations with $dt = 0.2\,\text{fs}$ and show an increase of chain percentage wise energy fluctuations with either v_0^{lab} or $|K_3|$.

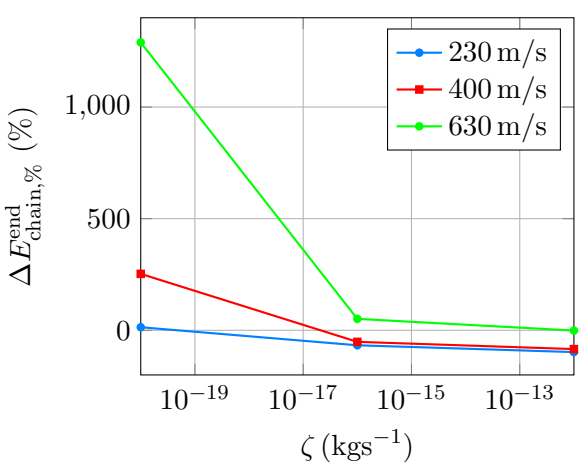

(a) $K_3 = -6.0 \times 10^{16}\,\mathrm{N/m^2}$, $V_0 = 1.0\,\mathrm{meV}$, different fixed v_0^{lab}. The same trend is observed also for every fixed $(K_3, v_0^{\mathrm{lab}})$ pair at $V_0 = 1.0\,\mathrm{meV}$

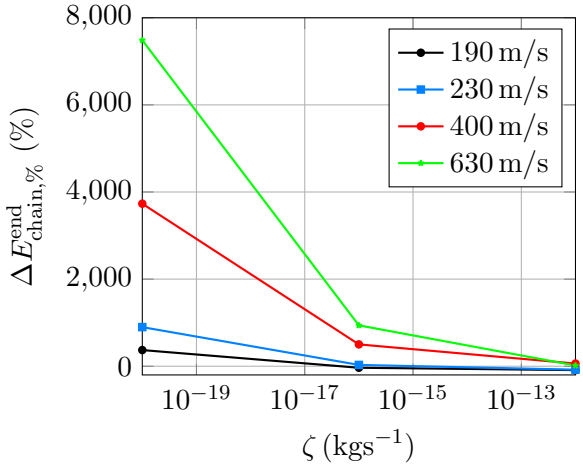

(b) $K_3 = -5.4 \times 10^{13}\,\mathrm{N/m^2}$, $V_0 = 0.5\,\mathrm{meV}$, different fixed v_0^{lab}. The same trend is observed also for every fixed $(V_0, v_0^{\mathrm{lab}} \geq 190\,\mathrm{m/s})$ at $K_3 = -5.4 \times 10^{13}\,\mathrm{N/m^2}$, except for $(0.1\,\mathrm{meV}, \{190, 230\}\,\mathrm{m/s})$

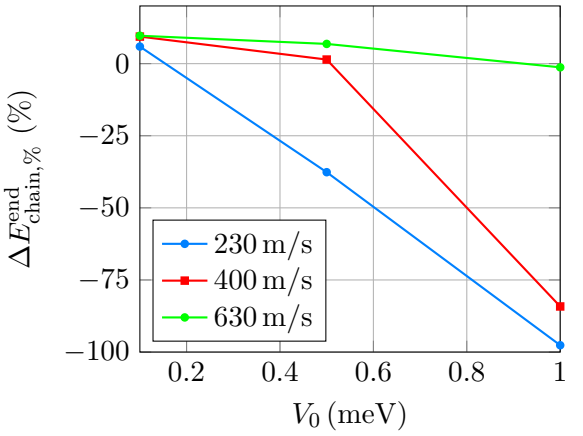

(c) $\zeta = 1.0 \times 10^{-12}\,\mathrm{kgs}^{-1}$, $K_3 = -6.0 \times 10^{16}\,\mathrm{N/m^2}$, different fixed v_0^{lab}. The same trend is observed also for every fixed $(\zeta, v_0^{\mathrm{lab}})$ at $K_3 = -6.0 \times 10^{16}\,\mathrm{N/m^2}$, except for $(1.0 \times 10^{-16}\,\mathrm{kgs}^{-1}, 230\,\mathrm{m/s})$

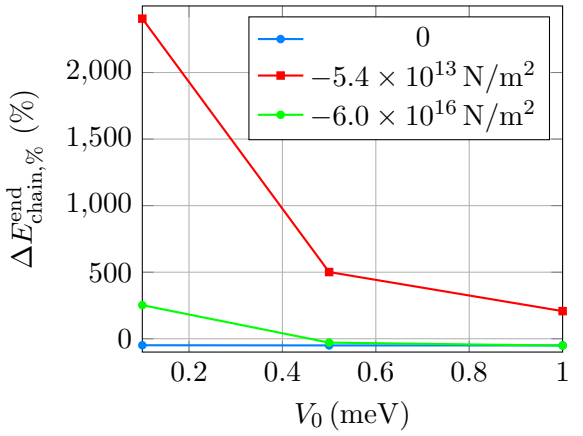

(d) $\zeta = 1.0 \times 10^{-16}\,\mathrm{kgs}^{-1}$, different fixed K_3, $v_0^{\mathrm{lab}} = 400\,\mathrm{m/s}$. The same trend is observed also for $\zeta = 1.0 \times 10^{-12}\,\mathrm{kgs}^{-1}$, different fixed K_3 and $v_0^{\mathrm{lab}} = 230\,\mathrm{m/s}$

Figure 3.23: Examples of peculiar and common decreasing trends of $\Delta E^{\mathrm{end}}_{\mathrm{chain},\%}$ for different values of $(\zeta, K_3, V_0, v_0^{\mathrm{lab}})$. For data points $\{(\zeta, \Delta E^{\mathrm{end}}_{\mathrm{chain},\%})\}$ a logarithmic scale is used and values of the damping coefficient are increased by $1.0 \times 10^{-20}\,\mathrm{kgs}^{-1}$ in order to show also the value corresponding to zero. Velocities here considered always allowed the particle to flow, regardless of the barrier height V_0. Data were acquired towards the end of 5 ns-long simulations with $dt = 0.2\,\mathrm{fs}$ and show a decrease of chain percentage wise energy fluctuations with either ζ or V_0.

Table 3.4: Summary of the relevant results found in BOMDs for different kinds of interactions between carbons in the chain.

C − C interaction	Particle dynamics	Behaviour of energies
Purely harmonic	When the particle has an initial velocity $v_0^{\text{lab}} \lesssim \sqrt{\frac{2V_0}{m}}$ and x_0^{lab} is located between two C atoms, the particle remains confined; if instead its initial velocity is high enough or if x_0^{lab} is on top of a C atom, the particle can flow; in both cases periodic oscillations emerge and persist throughout the whole dynamics	The particle transfers a small fraction of its energy to the chain; then, both exchanged and chain energy oscillate periodically
Anharmonic	Same as in the harmonic case, but with a phase shift and with more chaotic oscillations	Particle-chain energy exchange is enhanced (i.e. the particle loses more energy) and its periodic oscillations disappear; the transferred energy is harvested in the chain. For fixed v_0^{lab} and V_0, there exist specific values of K_3 which provide the highest energy transfer
With viscous contributions	Always considering the particle initially between two carbons, when the initial velocity is small enough the particle remains confined and shows damped oscillations, otherwise it can flow	Now both the particle and the chain experience an energy loss, which becomes greater with the entity of the damping coefficient ζ and with V_0. The chain energy loss does not occur immediately and follows different behaviours depending on the values of characterizing parameters

The robustness of these results in a small region close to $(-5.4 \times 10^{13}\,\text{N/m}^2, 0.5\,\text{meV})$ is suggested by the fact that, except close to absolute minima, undamped dissipation curve profiles of **Subsection 3.2.4** do not present abrupt changes and by the monotonicity of trends seen in **Figure 3.21b**, **Figure 3.22d**, **Figure 3.23c** and **Figure 3.23d**.

In **Table 3.4** a summary of the most relevant results found with BOMDs is presented.

Chapter 4

Density Functional Theory calculations

In order to provide realistic parameters for the Gaussian interaction of the effective model exposed in **Chapter 2** and used in Born-Oppenheimer molecular dynamics simulations, *ab-initio* Density Functional Theory (DFT) calculations were performed using the suite *Quantum ESPRESSO* [18–20]. In particular, DFT data allowed us to estimate the barrier (called *corrugation potential*) experienced by either a single water molecule or a linear chain of interacting H_2O molecules (a quasi-one dimensional ice structure named *1D ice*) while flowing inside a carbon nanotube. A proper description of van der Waals interactions in DFT (see below) was essential for an accurate determination of such corrugation potentials with different chiralities.

4.1 Theoretical background

Density Functional Theory describes the energy of a system of N particles by a functional E which does not depend explicitly on the N-particle wave function $\Psi(\vec{r}_1, \ldots, \vec{r}_N)$, characterized by $3N$ degrees of freedom, but on the system local density $\rho(\vec{r})$, with only three degrees of freedom, thanks to the two powerful theorems by Hohenberg and Kohn [21], reported in the next subsection. The ground state density of the system and the corresponding energy can then be obtained applying the variational principle.

4.1.1 Hohenberg-Kohn theorems [21, 22]

Theorem 1. *For a system of N electrons under an external potential $U(\vec{r})$, the density $\rho(\vec{r})$ is a unique functional of $U(\vec{r})$ and $U(\vec{r})$ is a unique functional of $\rho(\vec{r})$.*

In this way $\rho(\vec{r})$ uniquely determines $U(\vec{r})$, the Hamiltonian $\hat{H}$ (since kinetic and electron-electron interaction parts are formally known if one models the latter with Coulomb interaction) and in the end also the many-body wave function Ψ by solving its Schrödinger equation, meaning that effectively the energy functional E can be expressed in terms of ρ. But there is more: one can separate the different contributions in the energy functional $E[\rho]$ of a given system, writing it as a sum of the internal energy functional $F[\rho]$ (which is universal for the system under analysis, being independent of the number of particles and of the external potential applied) and of the external energy contribution, namely as

$$E[\rho] = F[\rho] + \int d\vec{r} U(\vec{r})\rho(\vec{r}) \,, \tag{4.1}$$

with $F[\rho] = T[\rho] + E_{\text{ee}}[\rho] = \langle \Psi_{\text{gs}} | \hat{T} + \hat{V}_{\text{ee}} | \Psi_{\text{gs}} \rangle$, i.e. sum of the kinetic and of the exact interaction energy of the system in its ground state Ψ_{gs}.

Theorem 2. *For a system of N identical interacting particles under an external potential $U(\vec{r})$, the density functional $E[\rho]$ is such that $E[\rho] \geq E[\rho_{\text{gs}}] = E_{\text{gs}}$ ground state energy and the equality holds for $\rho(\vec{r}) = \rho_{\text{gs}}(\vec{r})$ ground state density.*

However, in practice the expression for $F[\rho]$ is unknown: in the two following subsections some useful, practical recipes are presented.

4.1.2 Thomas-Fermi-Dirac-von Weizsäcker functional [22]

A first phenomenological expression for the energy functional E is based on the model proposed separately by Thomas [23] and Fermi [24] in 1927 to compute properties of atoms (such as the electron distribution around the nucleus and atomic fields), in which electrons are described as a uniform degenerate gas.

Given a system of N electrons of local density

$$\rho(\vec{r}) = N \int d\vec{r}_2 \dots d\vec{r}_{\mathrm{N}} \, |\Psi(\vec{r}, \vec{r}_2, \dots, \vec{r}_{\mathrm{N}})|^2 \,, \tag{4.2}$$

$\Psi(\vec{r}, \vec{r}_2, \dots, \vec{r}_{\mathrm{N}})$ being the N-electron many-body wave function, according to this model the Thomas-Fermi energy functional $E_{\mathrm{TF}}[\rho(\vec{r})]$ is expressed as (omitting the spatial dependence in the functional argument)

$$E_{\mathrm{TF}}[\rho] = T_{\mathrm{TF}}[\rho] + E_{\mathrm{H}}[\rho] + E_{\mathrm{ext}}[\rho] \,. \tag{4.3}$$

In this model T_{TF} is the generalization of the kinetic energy of a uniform electron gas to a slowly varying local density (generalization called *Local Density Approximation* or *LDA*)

$$T_{\mathrm{TF}}[\rho] = \int d\vec{r} \frac{3}{5} \frac{\hbar^2}{2m} (3\pi)^{\frac{2}{3}} \rho^{\frac{5}{3}}(\vec{r}) \,, \tag{4.4}$$

E_{H} is the electrostatic interaction energy between electrons described in the Hartree approximation (for this reason also called *direct interaction energy*)

$$E_{\mathrm{H}}[\rho(\vec{r})] = \frac{1}{2} \int d\vec{r} \, d\vec{r'} \, \frac{e^2}{4\pi\varepsilon_0 |\vec{r} - \vec{r'}|} \rho(\vec{r}) \rho(\vec{r'}) \,, \tag{4.5}$$

and E_{ext} is the interaction energy due to an external potential $U(\vec{r})$ (usually the electron-nuclei interaction in the case of condensed matter)

$$E_{\mathrm{ext}}[\rho(\vec{r})] = \int d\vec{r} U(\vec{r}) \rho(\vec{r}) \,. \tag{4.6}$$

In 1930 Dirac [25] proposed a functional correction $E_{\mathrm{X}}[\rho]$ to this model, called *exchange term* since it accounts for the exchange energy contribution in Hartree-Fock theory for a homogeneous gas of electrons with Coulomb interaction, supposed to hold also for a non-homogeneous system:

$$E_{\mathrm{X}}[\rho] = -C_{\mathrm{X}} \int d\vec{r} \, \rho^{\frac{4}{3}}(\vec{r}) \,, \tag{4.7}$$

in which C_{X} is a constant equal to $\left[\frac{3}{4} \frac{e^2}{4\pi\varepsilon_0} \left(\frac{3}{\pi}\right)^{\frac{1}{3}}\right]$.

Another relevant correction was proposed in 1935 by von Weizsäcker [26], correcting the kinetic energy of the system by introducing a gradient contribution:

$$E_{\mathrm{W}}[\rho] = \lambda_{\mathrm{W}} \int d\vec{r} \, \frac{\hbar^2}{2m} \left(\vec{\nabla} \sqrt{\rho(\vec{r})}\right)^2 \,, \tag{4.8}$$

with λ_{W} (called *von Weizsäcker coefficient*) being an adjustable phenomenological parameter; this correction provides an improvement only for systems with one or two electrons, but it is still relevant since it is the first historical example of gradient correction.

Consequently, the final expression for the Thomas-Fermi-Dirac-von Weizsäcker energy functional is

$$E_{\mathrm{TFDW}}[\rho] = T_{\mathrm{TF}}[\rho] + E_{\mathrm{H}}[\rho] + E_{\mathrm{ext}}[\rho] + E_{\mathrm{X}}[\rho] + E_{\mathrm{W}}[\rho] \,. \tag{4.9}$$

4.1.3 Kohn-Sham equations [27]

A very important practical recipe to implement DFT is the one proposed by Kohn and Sham in 1965: it consists of replacing the true system of interacting electrons with a fictitious non-interacting one with the same density of the original system and subject to a suitable external potential.

Starting from (4.1), one can add and subtract the kinetic energy of the fictitious non-interacting system $T_{\rm S}[\rho]$ and the Hartree-like electron-electron interaction energy $E_{\rm H}[\rho]$, obtaining:

$$E_{\rm KS}[\rho] = T_{\rm S}[\rho] + E_{\rm H}[\rho] + E_{\rm XC}[\rho] + \int d\vec{r}\, U(\vec{r})\rho(\vec{r})\,; \tag{4.10}$$

in this equation $E_{\rm XC}[\rho] = (T - T_{\rm S})[\rho] + (E_{\rm ee} - E_{\rm H})[\rho]$ is the *exchange-correlation energy* contribution, a quantity that unfortunately can only be approximated since its exact expression is unknown, while $T_{\rm S}$ is actually a functional which depends on the orthonormal wave functions $\{\varphi_i(\vec{r})\}_{i=1,\dots,N}$ (called *Kohn-Sham orbitals*) of the non-interacting system,

$$T_{\rm S} = -\frac{\hbar^2}{2m}\sum_{i=1}^{N}\int d\vec{r}\,\varphi_i^*(\vec{r})\nabla^2\varphi_i(\vec{r})\,. \tag{4.11}$$

The local density is consequently defined as $\rho(\vec{r}) = \sum_{i=1}^{N}|\varphi_i(\vec{r})|^2$.

Since $\rho(\vec{r})$ is expressed in terms of $\varphi_i(\vec{r})$ and $\varphi_i^*(\vec{r})$, these Kohn-Sham orbitals are now the variational parameters and applying the variational principle[1] one obtains a set of N coupled equations for them

$$\left\{-\frac{\hbar^2}{2m}\nabla^2 + \int d\vec{r'}\,\frac{e^2}{4\pi\varepsilon_0|\vec{r}-\vec{r'}|}\rho(\vec{r'}) + \frac{\delta E_{\rm XC}[\rho(\vec{r})]}{\delta\rho(\vec{r})} + U(\vec{r})\right\}\varphi_i(\vec{r}) = \varepsilon_i\varphi_i(\vec{r})\,,\ i = 1,\dots,N\,. \tag{4.12}$$

These equations are single-particle Schrödinger equations and coincide with those of the fictitious non-interacting system if the last three terms in curly brackets are identified with a fictitious external potential called *Kohn-Sham external potential* $U_{\rm KS}(\vec{r})$

$$U_{\rm KS}(\vec{r}) = \int d\vec{r'}\,\frac{e^2}{4\pi\varepsilon_0|\vec{r}-\vec{r'}|}\rho(\vec{r'}) + \frac{\delta E_{\rm XC}[\rho(\vec{r})]}{\delta\rho(\vec{r})} + U(\vec{r}) \equiv U_{\rm H}(\vec{r}) + U_{\rm XC}(\vec{r}) + U(\vec{r})\,, \tag{4.13}$$

leading to

$$H_{\rm KS}\,\varphi_i(\vec{r}) = \left\{-\frac{\hbar^2}{2m}\nabla^2 + U_{\rm KS}(\vec{r})\right\}\varphi_i(\vec{r}) = \varepsilon_i\varphi_i(\vec{r})\,,\ i = 1,\dots,N\,, \tag{4.14}$$

called *Kohn-Sham equations*. These equations are coupled since the Kohn-Sham external potential depends on all single-electron orbitals and therefore they have to be solved self-consistently; once $\{\varphi_i(\vec{r})\}_{i=1,\dots,N}$ have been determined, one can compute the energy and the density of the original system, but also other properties such as forces acting on nuclei.

As examples, in LDA the exchange-correlation functional $E_{\rm XC}$ can be expressed as

$$E_{\rm XC}^{\rm LDA} = \int d\vec{r}\,\rho(\vec{r})\epsilon_{\rm XC}^{\rm unif}(\rho)\,, \tag{4.15}$$

$\epsilon_{\rm XC}^{\rm unif}(\rho)$ being the exchange-correlation energy density of a uniform system of electrons, while in the *generalized gradient approximation* (GGA) one has

$$E_{\rm XC}^{\rm GGA} = \int d\vec{r}\, f(\rho, \vec{\nabla}\rho)\,, \tag{4.16}$$

$f(\rho, \vec{\nabla}\rho)$ being a particular function of system density and of its gradient. It has to be specified that, even if DFT is able to provide the exact energy of the ground state taking into account also van der Waals energies, all LDA and GGA functionals cannot reproduce such contributions due to the nature of these two approximations, which describe the system as an inhomogeneous gas of electrons [28]. Nevertheless, new approaches were developed in order to describe also van der Waals contributions (see below).

[1] Since single-particle orbitals are normalized, one has to introduce N Lagrangian multipliers $\{\varepsilon_i\}_{i=1,\dots,N}$ and to minimize the new functional $E_{\rm KS}[\rho] - \sum_{i=1}^{N}\varepsilon_i|\varphi_i|^2$.

4.1.4 *Quantum ESPRESSO* suite

Quantum ESPRESSO is an open-source suite for electronic-structure calculations and nanoscale materials modeling. Among the many adjustable parameters present in an input file, particularly relevant are:

- the type and dimension of the supercell, i.e. the periodically repeated unit of the system;
- values for parameters *ecutwfc* and *ecutrho*, which represent respectively the kinetic energy cutoff in the expansion of the wave function in terms of plane-wave basis set and the kinetic energy cutoff in the charge density expansion;
- the type of exchange-correlation functional (*input_ dft*) and of van der Waals correction (*vdw_ corr*) used;
- the type of *pseudopotential* used to mimic the true potential generated by the nucleus and by core electrons (which usually are little affected by bonds and clusters formations); they can be chosen for each chemical species involved in the calculation and allow to save computational time by freezing inner electrons, hence focusing only on valence ones. When ultra-soft pseudopotentials are used, as in this thesis work, *ecutrho* parameter should be approximately $6 \div 8$ times *ecutwfc*;
- positions of atoms of the different chemical species inside the supercell.

Moreover, different kinds of calculations can be performed, but in this thesis work two were mainly used: self-consistent wave function optimization (*'scf'* option) and geometry optimization (*'relax'* option).

A *'scf'* (self-consistent field) calculation consists of solving Kohn-Sham equations self-consistently, computing at every iteration the system total energy, until the difference between energies of the last two iterations is lower than a given threshold (whose default value is 1×10^{-6} Ry).

A *'relax'* calculation allows to optimize the system configuration keeping fixed the periodic supercell and consists of a series of *'scf'* cycles (at least one). At the end of each relaxation step (i.e. after a *'scf'* cycle ended) both system energy and forces acting on nuclei are computed and all ions are moved according to these forces; then a new *'scf'* cycle starts. This kind of calculations ends when differences in forces and energies of the last two cycles are below given thresholds (whose default values are respectively 1×10^{-3} Ry/Bohr and 1×10^{-4} Ry).

4.2 Corrugation potential characterization

4.2.1 Computational setup

Supercell dimensions

The choice of the supercell was particularly relevant. In all calculations performed, a primitive tetragonal cell was used, whose dimensions orthogonal and along the CNT axis were respectively

$$a \gtrsim 2d_{\mathrm{CNT}}\,, \quad c = n_{\mathrm{repl}} L_{\mathrm{CNT}}\,, \tag{4.17}$$

in which d_{CNT} was provided by (1.3), n_{repl} was the number of considered replicas of the elementary unit of the CNT and L_{CNT} was the length of such elementary unit. a was chosen in such a way that CNTs and encapsulated systems were isolated along directions orthogonal to the CNT axis. As for n_{repl}, its value depended on the chirality of the CNT (and hence on the number of C atoms in its smallest unit of repetition) and on the system encapsulated in it, also considering the computational cost of simulations: in the case of a single water molecule, 6 replicas were employed for a $(5,5)$ CNT, 5 for a $(7,7)$ and 3 for a $(9,9)$; as for 1D ice, 6 replicas were used for $(5,5)$ chirality, 4 in $(7,7)$ and 2 in $(9,9)$.

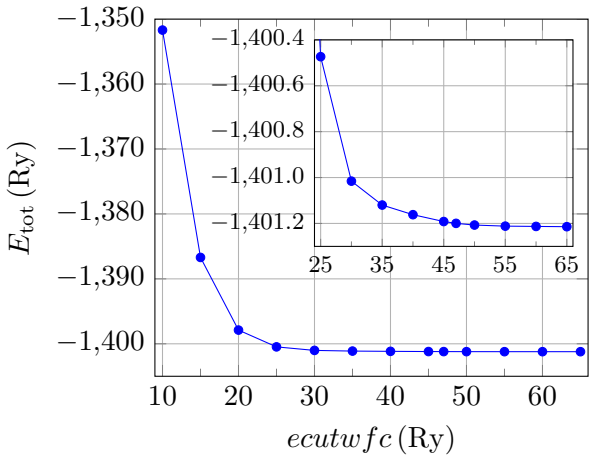

Figure 4.1: Convergence test of total energy as a function of the $ecutwfc$ parameter; the inset shows a zoom of the region where convergence was almost achieved.

Convergence of the *ecutwfc* parameter

Before computing energy values for corrugation potential evaluation, we studied the convergence of the total energy as a function of the *ecutwfc* parameter. This was carried by several self-consistent field calculations for a single H_2O water in a $(5, 5)$ CNT with PBE-D2 van der Waals correction (see later). The total energy convergence was performed starting from the value 10.0 Ry up to 65.0 Ry, increasing it by steps of 5.0 Ry, getting **Figure 4.1**. A first observation is that the convergence is achieved from above, as it is expected since *ecutwfc* is a variational parameter. Furthermore, looking at the inset, one can see how the curve flattens from 50.0 Ry onwards, which is the value that was chosen for the following calculations, also considering that the largest recommended minimum cutoff value for the three pseudopotentials used to describe the behaviour of H, C and O inner shells is 47.0 Ry. Consequently, *ecutwfc* and *ecutrho* were always set to 50.0 Ry and 330.0 Ry respectively.

Corrugation potential points methodology

Energy data used to characterize a single corrugation potential were obtained by adopting the following procedure:

1. a first *'relax'* calculation was performed, keeping fixed the z-coordinate of the O atom of the first water molecule and the first C atom of the CNT (in order to prevent the whole nanotube from moving together with the water structure); alternatively all C atoms of the nanotube were kept fixed. In both cases the CNT initial configuration was taken from Ref. [29];

2. the optimized water structure was then used to get data with a series of *'scf'* calculations, in which again the pristine configuration form Ref. [29] was used for the nanotube; before each new calculation, the water structure was translated along the z-axis (i.e. the CNT axis)[2] by 0.1 Å.

Unless differently specified, default thresholds for forces and energy were used.

4.2.2 Single water corrugation potential

Study of the best functional and configuration

First of all, different exchange-correlation functionals and van der Waals corrections and two different water dipole orientations were compared in order to assess which functional is more suited for the description of the corrugation profile and which configuration is more energetically favorable. As for corrections and functionals, the following were considered:

[2]It has to be specified that in **Chapter 2** and **Chapter 3** the CNT axis was chosen along the x-axis, while in this chapter it was considered along the z-axis.

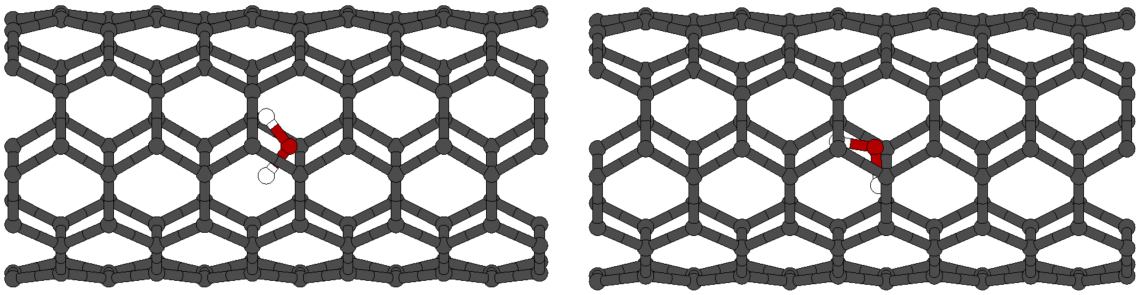

(a) Dipole along the z-axis **(b)** Dipole inclined by $-48°$ with respect to the z-axis

Figure 4.2: Representations of the supercell of a water molecule in a $(5, 5)$ armchair carbon nanotube with two different dipole orientations, realized with the visualization program *XCrySDen* [8]: carbon atoms are in grey, oxygen atoms in red and hydrogen atoms in white.

- PBE [30], which is a GGA functional providing a simpler and numerically similar version of another exchange-correlation GGA functional, i.e. PW91 [31]; PBE is characterized by the facts that all its parameters are fundamental constants and that it solves some of PW91 problems, like overparametrization, complexity and non transparency of the function $f(\rho, \vec{\nabla}\rho)$ in (4.16). Since, as pointed out, LDA and GGA are not able to describe van der Waals energy contributions, this kind of functional will be denoted as *no van der Waals* or *no-vdW*;

- Grimme-D2 (or PBE-D2) [32], which is a semiempirical GGA parametrized in order to introduce damped dispersion corrections between pairs of atoms of the form $\frac{C_6}{R^6} f_{\text{dmp}}(R)$, in which $f_{\text{dmp}}(R)$ is a damping function inserted to avoid singularities for small interatomic distances R;

- rVV10 [33], a revision of the VV10 functional [34], in which a nonlocal correlation functional

$$E_{\text{c}}^{\text{nl}} = \frac{\hbar}{2} \int \int d\vec{r} d\vec{r'}\, \rho(\vec{r}) \Phi(\rho, \vec{\nabla}\rho, |\vec{r} - \vec{r'}|) \rho(\vec{r'}) \tag{4.18}$$

  is added together with a LDA/GGA exchange functional. The revision consists of a simple and sound modification of the expression for $\Phi(\rho, \vec{\nabla}\rho, |\vec{r} - \vec{r'}|)$;

- vdW-DF-cx [35], which is a nonempirical exchange-correlation functional based on plasmon description, depending on density and its gradients in a nonlocal manner.

As for orientations, the water molecule dipole was considered either aligned along the CNT axis or inclined with an angle of approximately $-48°$ with respect to the z-axis; the latter was chosen as one of the many possible reasonable water configurations with inclined dipole. These two orientations can be seen in **Figure 4.2**. This preliminary study, performed for a $(5, 5)$ CNT, yielded corrugation potentials shown in **Figure 4.3a** and in **Figure 4.3b**, whose data were obtained leaving all C atoms free to move in the CNT (except for the first one) in step 1 and performing *'scf'* calculations in step 2 but every 0.2 Å; thresholds were considered equal to 2×10^{-5} Ry for energy and to 4.5×10^{-4} Ry/Bohr for forces to account for small deformations in CNT structure.

In the first place, all corrugation potentials are periodic, as one would expect from the periodic structure of the CNT, even though the periodicity for rVV10 and vdW-DF-cx corrections in the aligned case is not as evident as in the other cases due to the numerical noise caused by *'scf'* calculations, which dominates over corresponding barriers, as one can see in **Figure 4.3c**. Moreover, looking at these plots, one can notice how the periodicity is different depending on the angle formed by the dipole with respect to the z-axis, being roughly 1.2 Å in the aligned case and 2.5 Å when it is inclined.

Referring to **Figure 4.3a**, PBE-D2 correction provides the smallest barrier, while no-vdW the highest; instead, looking at **Figure 4.3b**, in the aligned case no-vdW provides a quite small barrier, while rVV10 and vdW-DF-cx profiles exhibit many irregularities due to the already pointed out *'scf'* numerical noise dominance over the barrier. Furthermore, barriers are higher when the water dipole is not aligned with the z-axis. Consequently, PBE-D2 was deemed to be the most suited functional to be used for further

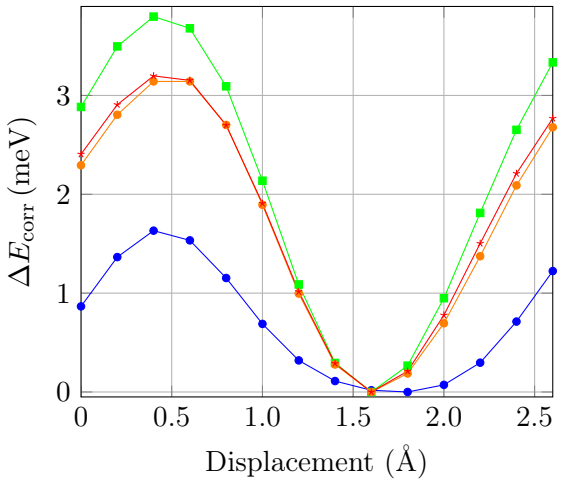

(a) Dipole inclined by $-48°$ with respect to z-axis

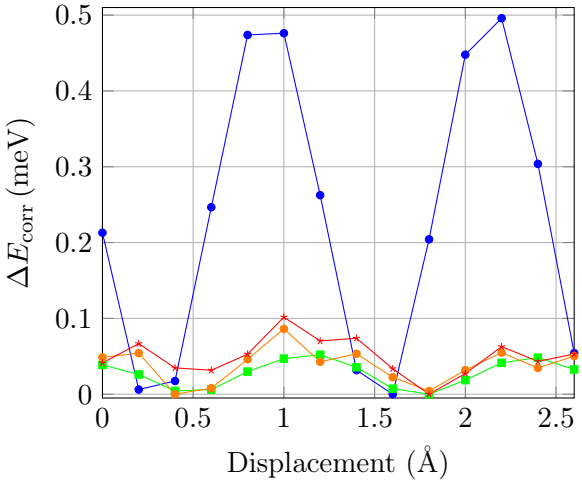

(b) Dipole along the z-axis

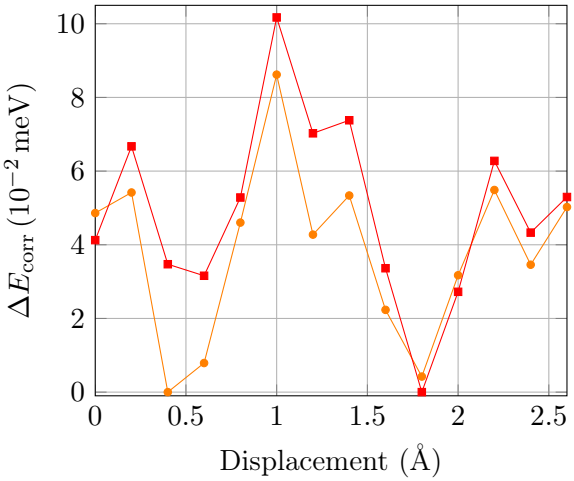

(c) Case of dipole along the z-axis for rVV10 (in orange) and vdW-DF-cx (in red) functionals

Figure 4.3: Comparison between corrugation potentials obtained with different van der Waals corrections and exchange-correlation functionals for two different orientations of the water dipole in the $(5, 5)$ CNT: green lines represent data obtained using the PBE functional, blue lines represent PBE-D2 functional, orange ones rVV10 and red ones vdW-DF-cx. ΔE_{corr} is the value of the total energy with respect to the minimum, i.e. $\Delta E_{\text{corr}} = E_{\text{tot}} - E_{\text{tot}}^{\text{min}}$. PBE-D2 and the oriented configuration were deemed to be respectively the most suitable functional and the most stable configuration.

Table 4.1: Differences between the energies of a single water molecule in a $(5, 5)$ CNT with inclined dipole $E^{\text{incl}}_{\text{corr}}$ and with dipole along the z-axis E^{z}_{corr} for different van der Waals corrections and exchange-correlation functionals: when such differences are positive, alignment with the z-axis is favoured. Displacements are computed with respect to the configuration with oxygen z-position at 5.91 Å, whose value should not affect the result since water z-coordinates were shifted by multiples of 0.1 or 0.2 Å and since the system is periodic, with large enough supercell to prevent interactions between replicas. With PBE-D2 correction the aligned configuration is stabler than inclined one.

(a) no-vdW

Displacement (Å)	$E^{\text{incl}}_{\text{corr}} - E^{z}_{\text{corr}}$ (meV)
0	−0.742
0.2	−0.117
0.4	0.206
0.6	0.086
0.8	−0.525
1	−1.497
1.2	−2.551
1.4	−3.329
1.6	−3.595
1.8	−3.321
2	−2.657
2.2	−1.817
2.4	−0.983
2.6	−0.286

(b) PBE-D2

Displacement (Å)	$E^{\text{incl}}_{\text{corr}} - E^{z}_{\text{corr}}$ (meV)
0	15.413
0.2	16.123
0.4	16.379
0.6	16.052
0.8	15.444
1	14.977
1.2	14.821
1.4	14.843
1.6	14.782
1.8	14.560
2	14.387
2.2	14.565
2.4	15.173
2.6	15.934

(c) rvv10

Displacement (Å)	$E^{\text{incl}}_{\text{corr}} - E^{z}_{\text{corr}}$ (meV)
0	1.132
0.2	1.637
0.4	2.029
0.6	2.021
0.8	1.543
1	0.694
1.2	−0.160
1.4	−0.888
1.6	−1.135
1.8	−0.930
2	−0.450
2.2	0.206
2.4	0.943
2.6	1.515

(d) vdW-DF-cx

Displacement (Å)	$E^{\text{incl}}_{\text{corr}} - E^{z}_{\text{corr}}$ (meV)
0	−1.917 95
0.2	−1.442 62
0.4	−1.119 24
0.6	−1.161 58
0.8	−1.636 64
1	−2.476 61
1.2	−3.337 15
1.4	−4.067 78
1.6	−4.315 86
1.8	−4.071 73
2	−3.532 54
2.2	−2.8422
2.4	−2.115 52
2.6	−1.5672

corrugation potential studies, since in the aligned case it is the only one able to describe a profile whose height is of the same magnitude of other results reported in literature, such as those of Ref. [7].

As for the identification of the most stable configuration, in **Table 4.1** the energy difference (at the same displacement with respect to the configuration with oxygen z-position at 5.91 Å[3]) between the inclined case $E_{\text{corr}}^{\text{incl}}$ and the oriented one E_{corr}^{z} is showed for different corrections and functionals: as one can see, with PBE-D2 correction such difference is always positive, meaning that the energy of H_2O in a $(5,5)$ CNT with inclined dipole is always higher than the aligned case, and hence that the rotated-dipole configuration is more unstable. Differences for no-vdW, rVV10 and vdW-DF-cx corrections are also reported for completeness.

In conclusion, from now on only the PBE-D2 correction will be employed (also for 1D ice calculations) and single water molecules will be considered with the dipole along the CNT axis, since it represents a stabler configuration compared to the inclined one.

Effect of CNT chirality

Data used to characterize single water corrugation potentials were obtained following the methodology explained above, keeping all carbons in the nanotube fixed in step 1.

Results for $(5,5)$ and $(7,7)$ armchair CNT are represented by blue points in **Figure 4.4a** and **Figure 4.4c** respectively: both corrugation potentials present a periodicity of roughly 1.2 Å, but data for the $(7,7)$ chirality are more irregular due to the lower barrier they provide, more susceptible to numerical noise from *'scf'* calculations[4] (this is why points are connected with lines, in order to guide the eye).

These points were shifted in such a way that the minimum was in zero and were then fitted with the expression[5]

$$V_{\text{int}}(x) = V_0 \sum_{n=-3}^{3} e^{-\left(\frac{x-nL^{\text{fit}}}{\Delta}\right)^2} + C \tag{4.19}$$

using the software *Gnuplot*, with $L^{\text{fit}} = 1.231\,179$ Å. These fits (shown in red in the aforementioned figures) yielded parameter values shown in **Table 4.2** for each chirality. Uncertainties of the three quantities were found following this procedure:

1. a preliminary fit was performed using (4.19) and taking parameters V_0, Δ and C as fitting parameters;
2. since errors provided by *Gnuplot* in this first fit were fairly large (i.e. comparable with quantities themselves, if not even greater), a second fit was performed keeping V_0 fixed equal to the value found in 1;
3. point 2 was repeated keeping fixed first only Δ and then only C;
4. results of fits in 2 and 3 were compared and found to be in agreement every time within their corresponding standard deviation; the final uncertainty was estimated as the highest error from these fits, in order to avoid underestimations.

It has to be pointed out that originally the value for $C^{(5,5),\text{fit}}$ was (-1.35 ± 0.01) meV, but it was then chosen to be (-1.34 ± 0.01) meV in order to always have positive corrugation potentials, with the introduced variation that was within the standard error and hence deemed acceptable (however, the value of this parameter is not relevant since it causes a trivial rigid shift of energies).

[3] Such a value of initial oxygen z-position should not affect the result since water structure's z-coordinates were shifted by multiples of 0.1 or 0.2 Å and since the system is periodic, with large enough supercell to prevent interactions between replicas.

[4] Actually, *'relax'* calculations were performed at first, but every time they ended with a single *'scf'* cycle and hence with no optimization, meaning that their results coincide with those of *'scf'* calculations.

[5] The x variable was actually shifted in such a way that, for every chirality, the first maximum of the corrugation potential was in correspondence of zero displacement; this choice should not affect the final result thanks to the equivalence of initial configurations with respect to which displacements can be computed.

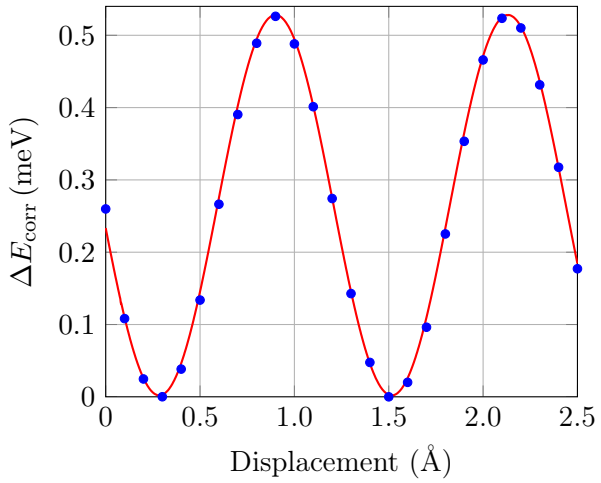

(a) Water-$(5,5)$ CNT corrugation potential

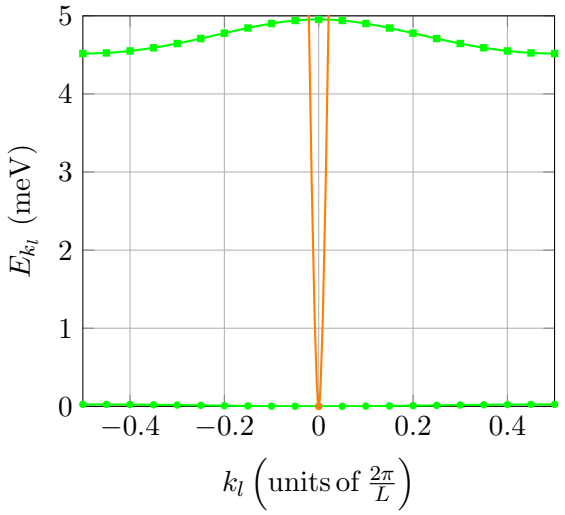

(b) Energy bands for water in a $(5,5)$ CNT

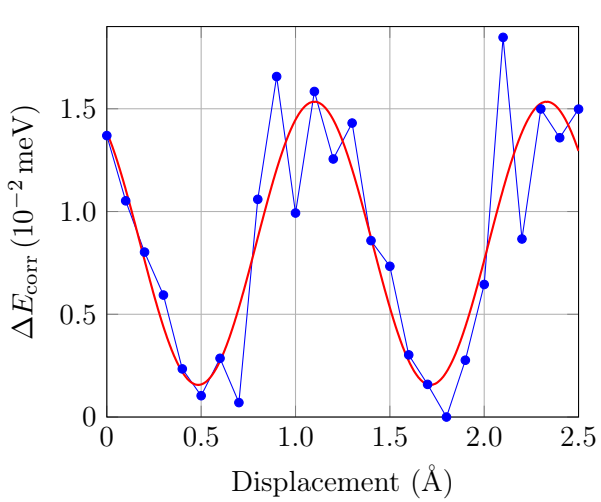

(c) Water-$(7,7)$ CNT corrugation potential

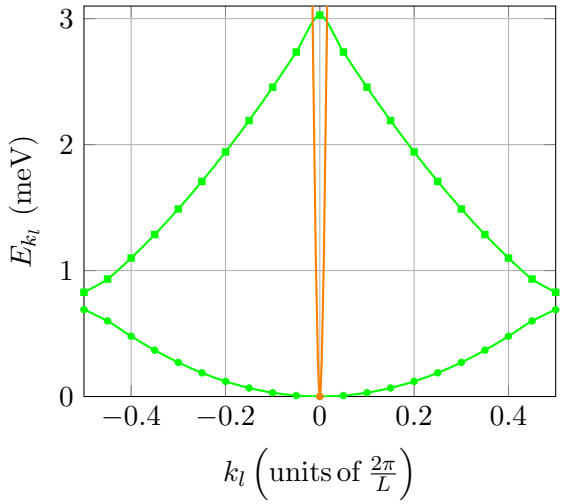

(d) Energy bands for water in a $(7,7)$ CNT

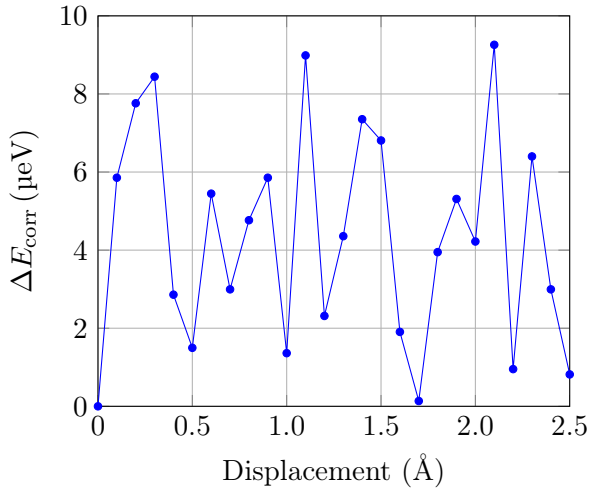

(e) Water-$(9,9)$ CNT corrugation potential

Figure 4.4: Corrugation potential points of a single water molecule (blue points), with the corresponding fitting function (4.19) (in red), in armchair carbon nanotubes with different chirality for PBE-D2 correction. Corresponding energy bands (in green) are also shown and compared with chain phonon spectrum (in orange). ΔE_{corr} is the value of the total energy with respect to the minimum, i.e. $\Delta E_{\text{corr}} = E_{\text{tot}} - E_{\text{tot}}^{\text{min}}$. Comparing the three corrugation potentials one can see that the height of the barrier tends to decrease as chiral coefficients (and consequently CNT radius) increase. Comparing also the energy bands one can understand how no water-CNT energy transfer is possible when the flowing particle is in its lowest energy band.

Table 4.2: Values of parameters of (4.19) obtained from fits of single water corrugation potentials with different chiralities shown in **Figure 4.4**. $(9,9)$-chirality parameters are not present since no fit could be performed due to the dominance of numerical noise over the barrier.

Chirality	V_0^{fit} $(10^{-2}\,\text{meV})$	Δ^{fit} (Å)	C^{fit} $(10^{-2}\,\text{meV})$
$(5,5)$	180 ± 1	0.620 ± 0.001	-134 ± 1
$(7,7)$	6.5 ± 0.7	0.67 ± 0.02	-5.3 ± 0.7

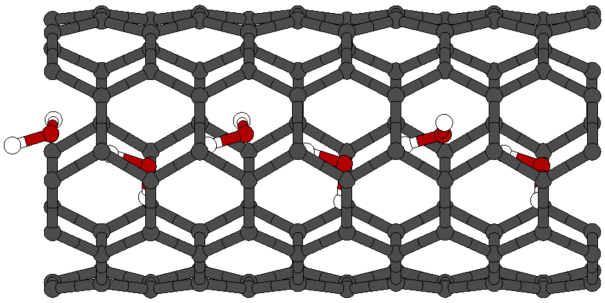

Figure 4.5: Representation of the supercell of 1D ice structure in a $(5,5)$ armchair carbon nanotube, realized with the visualization program *XCrySDen* [8]: carbon atoms are in grey, oxygen atoms in red and hydrogen atoms in white.

It has to be specified also that there is a crucial difference between the value of V_0 in BOMDs and the one from these *ab-initio* calculations: due to value of the Gaussian width Δ chosen in **Chapter 3**, there is a one-to-one correspondence between V_0 and the maximum of the Gaussian interaction (corresponding to the height of the barrier); instead, in these corrugation potentials the values of Δ^{fit} are such that the height of the barrier corresponds not to V_0^{fit} alone, but to $V_0^{\text{fit}} + C^{\text{fit}}$. This difference has to be taken into account when comparing barriers in **Chapter 3** and from this chapter.

In order to understand whether an exchange of energy was possible between the water molecule and the CNT, water energy bands (computed using the effective model as exposed in **Subsection 2.1.2** and with parameter values from **Table 4.2**) were compared with the chain phonon spectrum, obtaining **Figure 4.4b** and **Figure 4.4d**: as one can notice, our model predicts that no energy transfer is possible when the flowing particle is in its lowest energy band, since in this case the two dispersion relations intersect only at $k_l = 0$, corresponding to water at rest.

In the end, peculiar is the case of the $(9,9)$ CNT: as one can see from **Figure 4.4e**, the energy barrier is so small that numerical noise dominates, making it impossible to perform any fit; this is why for this chirality no values are reported in **Table 4.2** and no energy bands were computed.

Comparing all these three single-water corrugation potentials, one can see that the height of the barrier tends to decrease as chiral coefficients (and consequently CNT radius) increase.

4.2.3 1D ice corrugation potential

In order to estimate barriers for 1D ice, represented in **Figure 4.5**, all carbon atoms were again kept fixed during the first *'relax'* calculation in step 1 of the methodology exposed above. Resulting barriers per unit molecule are illustrated in **Figure 4.6**: as one can see, again the barrier decreases as the radius increases, with even a change in the shape. Also in this case the barrier in a $(9,9)$ CNT is so small that numerical noise from *'scf'* convergence dominates.

It has to be noted that, at variance with the previous case of single water, in which the dimension of the supercell was enough to prevent interactions, now water molecules interact not only within the supercell but also with other molecules in periodic replicas along the CNT axis. The presence of such interactions causes a relevant increase of the corrugation potential height, enhancement which is higher the larger the radius. Furthermore, compared again to the single-water case, 1D ice corrugation potentials present a periodicity equal to that of the supercell, i.e. approximately 2.4 Å.

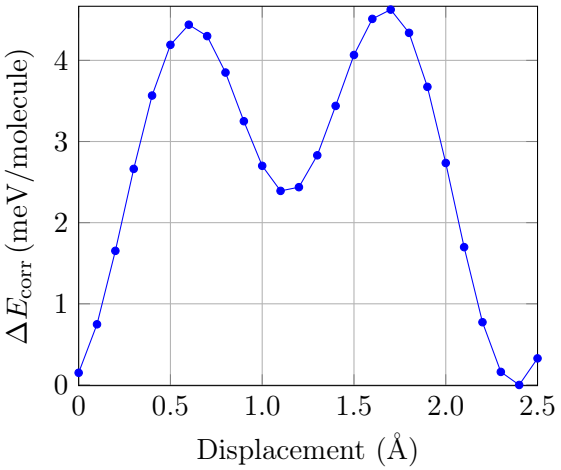

(a) 1D ice-$(5,5)$ CNT corrugation potential

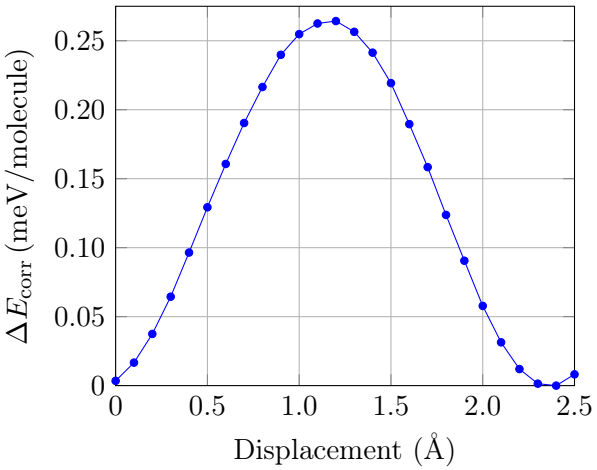

(b) 1D ice-$(7,7)$ CNT corrugation potential

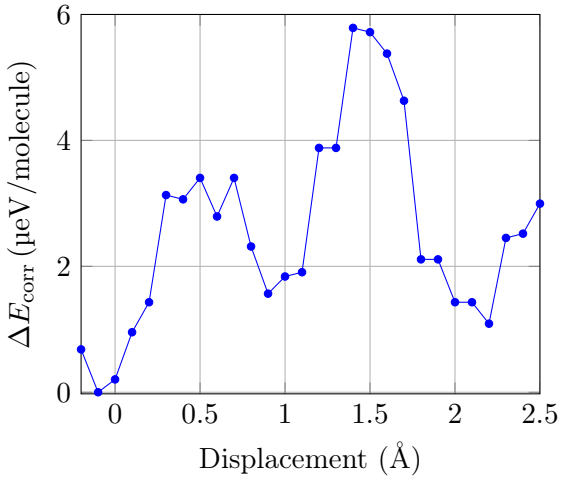

(c) 1D ice-$(9,9)$ CNT corrugation potential

Figure 4.6: Study of the corrugation potential per unit molecule of 1D ice in an armchair carbon nanotube with different chirality for PBE-D2 correction. In this case ΔE_{corr} is the value of the system total energy with respect to the minimum, normalized to the number of water molecules in the chain, i.e. $\Delta E_{\text{corr}} = \frac{E_{\text{tot}} - E_{\text{tot}}^{\text{min}}}{N_{\text{H}_2\text{O}}}$. Comparing the three corrugation potentials, one can see that also in this case the height of the barrier tends to decrease as chiral coefficients (and consequently CNT radius) increase.

Chapter 5

Conclusions

Some interesting results were achieved in this thesis. In **Chapter 2** we developed a model to effectively describe the flow of a particle in a $(5, 5)$ armchair carbon nanotube, later used to compute particle dispersion relations and chain phonon spectrum. In **Chapter 3** Born-Oppenheimer molecular dynamics simulations were performed, combining the aforementioned model with different kinds of $C-C$ interaction: among the most relevant results exposed in **Table 3.4**, particularly striking ones regard particle-chain energy transfer and chain energy dissipation. With only harmonicity, little particle-chain exchange occurs and it is oscillating in time. With anharmonicity this transfer increases and loses its periodicity, the energy being harvested in the chain; moreover, this exchange can become maximum for particular values of the third-order anharmonic coefficient K_3, which depend on particle initial velocity v_0^{lab} and barrier height V_0. If damping contributions are further introduced (corresponding to CNT radiative decays or couplings to the environment), also the chain experiences an energy loss, which is enhanced with the damping coefficient ζ and with the barrier height V_0, as it also occurs with particle-chain energy exchange. In **Chapter 4** the corrugation of interface potential was studied for both a single water molecule and for 1D ice encapsulated in armchair CNTs with different chiralities: we detected a decrease of the barrier height as the CNT radius was increased. Furthermore, realistic parameters for the developed model were estimated and exposed in **Table 4.2** and it was shown how, when in its lowest energy band, water cannot scatter with the CNT, with hence no energy transfer.

Applying results of **Chapter 3** and **Chapter 4** to the real case of water in armchair nanotubes, we can then predict an increase of particle-chain energy transfer if the CNT radius (and consequently its chirality) is reduced or if the damping coefficient ζ is increased and an enhancement of chain energy loss with ζ.

To the best of our knowledge, no other studies reporting similar results in the subject matter of this work were done as for now.

One of the possible future perspectives provided by this thesis work would be, for instance, repeating the study of anharmonicity and damping effects in BOMDs with other K_3/K_4 ratios. Furthermore, since in **Figure 4.3** different water dipole moment orientations are shown to lead to different periodicity and magnitudes of the corrugation potential, one could possibly refine the proposed effective model by including an internal degree of freedom of the particle, i.e. the presence of a dipole moment. A study of 1D ice dynamics through BOMDs could be also performed, with the consequent development of a new interaction potential to use as a fitting function for profiles in **Figure 4.6a** and in **Figure 4.6b**. Moreover, it would be interesting to repeat quantum-mechanical calculations of Ref. [7] but with anharmonic effects, in order to compare those results with classical ones of this thesis. In addition, one could take a step further with respect to what done in this work going beyond Born-Oppenheimer molecular dynamics, hence including also quantum-mechanical effects for both a single flowing molecule and for 1D ice. As last possible research direction opened up by this project, corrugation potentials could be studied with other corrections and functionals, but also with other chiralities in order to acquire a broader view of the phenomenon of superflow. Experimental data of corrugation potentials would represent a valuable resource as well, allowing a comparison with *ab-initio* results.

Appendix A

Bloch theorem approach to Central equation

Using Bloch theorem (since the external potential is periodic), one can express the particle wave function in Bloch state (n, k), with n being the band number and k a IBZ vector, as

$$\begin{cases} \psi_k^n(x) = e^{ikx} u_k^n(x) \\ u_k^n(x + L) = u_k^n(x) \end{cases} \tag{A.1}$$

and expressing also $u_k^n(x)$ in Fourier series one has

$$u_k^n(x) = \sum_{G_m} C_{k+G_m}^n e^{iG_m x} \implies \psi_k^n(x) = \sum_{G_m} C_{k+G_m}^n e^{i(k+G_m)x} \,. \tag{A.2}$$

Inserting then this expansion in (2.10) one obtains

$$\sum_{G_m} \frac{\hbar^2}{2m}(k+G_m)^2 e^{i(k+G_m)} C_{k+G_m}^n + \sum_{G'_m} \sum_{G_m} V_{G'_m} C_{k+G_m}^n e^{i(k+G_m+G'_m)x} = E_k^n \sum_{G_m} e^{i(k+G_m)} C_{k+G_m}^n \,; \tag{A.3}$$

translating in the second left hand side term $G'_m \to G'_m - G_m$ and swapping G'_m and G_m in place (since they are dummy variables) yields to

$$\frac{\hbar^2}{2m}(k+G_m)^2 C_{k+G_m}^n + \sum_{G'_m} V_{G_m - G'_m} C_{k+G'_m}^n = E_k^n C_{k+G_m}^n \,. \tag{A.4}$$

Finally, since $G_m = \frac{2\pi}{L} m$ with $m \in \mathbb{Z}$, its sign (and the one of G'_m) can be reversed when summing over it, getting exactly (2.14).

Appendix B

Algorithms employed in BOMDs

Supposing to be in one dimension as it is done in the effective model developed in **Chapter 2**, algorithms used in BOMDs are now presented.

B.1 Original Verlet

The Verlet algorithm [13] allows to solve Newton's equations for a system of particles conserving its energy, i.e. it is symplectic. Knowing the position x_i of the i^{th} particle of the system and its derivatives at time t, one can expand its positions at time $t+dt$ and $t-dt$ in Taylor series up to third order as:

$$\begin{cases} x_i(t+dt) = x_i(t) + \dot{x}_i(t)dt + \frac{1}{2}\ddot{x}_i(t)dt^2 + \frac{1}{3!}\dddot{x}_i(t)dt^3 + \mathcal{O}(dt^4) \\ x_i(t-dt) = x_i(t) - \dot{x}_i(t)dt + \frac{1}{2}\ddot{x}_i(t)dt^2 - \frac{1}{3!}\dddot{x}_i(t)dt^3 + \mathcal{O}(dt^4) \end{cases} ; \tag{B.1}$$

summing these two equations yields the first equation used in the algorithm

$$x_i(t+dt) = 2x_i(t) - x_i(t-dt) + a_i(t)dt^2 + \mathcal{O}(dt^4)\,. \tag{B.2}$$

In order to obtain the velocity, one can use the standard formula for numerical derivation:

$$v_i(t+dt) = \frac{x_i(t+dt) - x_i(t-dt)}{2dt} + \mathcal{O}(dt^2)\,, \tag{B.3}$$

which represents the second formula of the algorithm.

B.2 Velocity Verlet

At variance with its original version, in velocity Verlet algorithm [12] one expands both $x_i(t+dt)$ and $x_i(t)$ up to second order:

$$\begin{cases} x_i(t+dt) = x_i(t) + \dot{x}_i(t)dt + \frac{1}{2}\ddot{x}_i(t)dt^2 + \mathcal{O}(dt^3) \\ x_i(t) = x_i(t+dt) - \dot{x}_i(t+dt)dt + \frac{1}{2}\ddot{x}_i(t+dt)dt^2 + \mathcal{O}(dt^3) \end{cases} \tag{B.4}$$

and sums them to obtain the expression for the velocity

$$v_i(t+dt) = v_i(t) + \frac{1}{2}[a_i(t) + a_i(t+dt)]dt + \mathcal{O}(dt^2)\,. \tag{B.5}$$

Introducing the velocity after half a timestep $v_i(t+dt/2) = v_i(t) + \frac{1}{2}a_i(t)dt$, one can rewrite the two equations for this algorithm as

$$\begin{cases} x_i(t+dt) = x_i(t) + v_i(t+dt/2)dt \\ v_i(t+dt) = v_i(t+dt/2) + \frac{1}{2}a_i(t+dt)dt \end{cases} . \tag{B.6}$$

For the system under analysis in presence of anharmonicity, expressions for the accelerations used both in original Verlet and velocity Verlet are

$$\begin{cases} K\{[(X_{i-1}-X_i)_{nn}+L]+[(X_{i+1}-X_i)_{nn}-L]\}+ \\ -\frac{2V_0}{\Delta^2}e^{\left[-\frac{(x-X_i)^2_{nn}}{\Delta^2}\right]}(x-X_i)_{nn}+ \\ +3K_3\{-[(X_{i-1}-X_i)_{nn}+L]^2+[(X_{i+1}-X_i)_{nn}-L]^2\}+ \\ +4K_4\{[(X_{i-1}-X_i)_{nn}+L]^3+[(X_{i+1}-X_i)_{nn}-L]^3\} \qquad \text{for the chain} \\ \frac{2V_0}{\Delta^2}\sum_{j=1}^{N} e^{\left[-\frac{(x-X_j)^2_{nn}}{\Delta^2}\right]}(x-X_j)_{nn} \qquad \text{for the particle} \end{cases} , \tag{B.7}$$

with $(X_{i+1}-X_i)_{nn}$ denoting the distance between the two closest replicas of the $(i+1)^{\text{th}}$ and of the i^{th} particle.

B.3 Runge-Kutta

Runge-Kutta algorithms [14, 15] allow to integrate ordinary differential equations with initial conditions, such as

$$\begin{cases} \frac{dy}{dt} = f(t,y) \\ y(t_0) = y_0 \end{cases} . \tag{B.8}$$

The version employed in this work is the *Fourth order Runge-Kutta*, in which four coefficients are introduced, defined as

$$\begin{cases} k_1 = f(t_n, y_n) \\ k_2 = f(t_n + \frac{dt}{2}, y_n + k_1\frac{dt}{2}) \\ k_3 = f(t_n + \frac{dt}{2}, y_n + k_2\frac{dt}{2}) \\ k_2 = f(t_n + dt, y_n + k_3 dt) \end{cases} , \tag{B.9}$$

with $t_n = t_0 + n\,dt$; then, given $y_n = y(t_n)$, one can compute y_{n+1} as

$$y_{n+1} = y(t_{n+1}) = y_n + dt\frac{(k_1+2k_2+2k_3+k_4)}{6} . \tag{B.10}$$

This algorithm was used to integrate Newton's equations of motion for the system of interest in presence of viscous terms acting on the CNT, rewriting second order differential equations as a system of first order ones; furthermore, since time does not appear explicitly in these equations, functions $f(t,y)$ are time-independent.

Denoting with $\vec{X} = (X_1, \ldots, X_N, x)$ the vector of the $N+1$ positions and with $\vec{V} = (V_1, \ldots, V_N, v)$ the vector of velocities, one can write:

$$\begin{cases} \dot{\vec{X}} = \vec{V} \\ \dot{v} = f_1(\vec{X}) \\ \dot{V}_i = f_3(\vec{X}, \vec{V}, i) \end{cases} , \tag{B.11}$$

with

$$f_1(\vec{X}) = \frac{1}{m}\frac{2V_0}{\Delta^2}\sum_{j=1}^{N} e^{\left[-\frac{(x-X_j)^2_{nn}}{\Delta^2}\right]}(x-X_j)_{nn} \tag{B.12}$$

and

$$\begin{aligned} M\, f_3(\vec{X},\vec{V},i) = {} & K\{[(X_{i-1}-X_i)_{nn}+L]+[(X_{i+1}-X_i)_{nn}-L]\}+ \\ & -\frac{2V_0}{\Delta^2}e^{-\left[\frac{(x-X_i)^2_{nn}}{\Delta^2}\right]}(x-X_i)_{nn} + 3K_3\{-[(X_{i-1}-X_i)_{nn}+L]^2+[(X_{i+1}-X_i)_{nn}-L]^2\}+ \\ & + 4K_4\{[(X_{i-1}-X_i)_{nn}+L]^3+[(X_{i+1}-X_i)_{nn}-L]^3\} - \zeta V_i . \end{aligned} \tag{B.13}$$

In order to solve these differential equations, one has to introduce two vectors of coefficients $\vec{k}$ and $\vec{l}$, associated respectively with $\vec{X}$ and $\vec{V}$:

$$\begin{cases} k_{1,i} = \left[\vec{V}\right]_i \\ k_{2,i} = \left[\vec{V}\right]_i + l_{1,i}\frac{dt}{2} \\ k_{3,i} = \left[\vec{V}\right]_i + l_{2,i}\frac{dt}{2} \\ k_{4,i} = \left[\vec{V}\right]_i + l_{3,i}dt \end{cases} , \quad \begin{cases} l_{1,i} = f(\vec{X}, \vec{V}) \\ l_{2,i} = f(\vec{X} + \vec{k}_1\frac{dt}{2}, \vec{V} + \vec{l}_1\frac{dt}{2}) \\ l_{3,i} = f(\vec{X} + \vec{k}_2\frac{dt}{2}, \vec{V} + \vec{l}_2\frac{dt}{2}) \\ l_{4,i} = f(\vec{X} + \vec{k}_3 dt, \vec{V} + \vec{l}_3 dt) \end{cases} \tag{B.14}$$

with

$$f(\vec{X}, \vec{V}) = \begin{cases} f_3(\vec{X}, \vec{V}, i) & \text{for the chain} \\ f_1(\vec{X}) & \text{for the particle} \end{cases} . \tag{B.15}$$

Appendix C

Estimate of anharmonicity in a $(5, 5)$ CNT

To the best of our knowledge, until now values of anharmonic coefficients K_3 and K_4 in carbon nanotube Hamiltonian (3.4) have not been estimated explicitly or measured for a single CNT, since in scientific literature results are reported either for linear carbon chains with different numbers of bonds between C atoms [36], for rigid bunches of CNTs [37] or for anharmonic effects on Raman shifts [38, 39].

So as to estimate the order of magnitude of K_3, we consider the expression for the elastic potential energy of the chain within the CNT effective model for N carbons in presence of anharmonicity:

$$V_{\text{anharm},N} = \frac{K}{2} \sum_{\substack{n=1 \\ n\,\text{per}}}^{N} (\Delta X_n - L)^2 + K_3 \sum_{\substack{n=1 \\ n\,\text{per}}}^{N} (\Delta X_n - L)^3 + K_4 \sum_{\substack{n=1 \\ n\,\text{per}}}^{N} (\Delta X_n - L)^4 \,, \tag{C.1}$$

with $\Delta X_n = X_n - X_{n-1}$ being the distance between nearest replicas of the n^{th} and of the $(n-1)^{\text{th}}$ carbon. In order to simplify the analytic evaluation, the contribution of K_4 is neglected in the following analysis.

Looking at **Figure 3.6** one can see how, if just K_3 is present and if it is large enough, the potential is well-defined and stable only for negative displacements, while in the other half plane it grows becoming more and more negative; the idea is then to mirror the left side of this potential, making it stable also on the right side (i.e. for positive displacements), as shown in **Figure C.1**. This corresponds to replacing the original anharmonic potential of the n^{th} spring with an effective harmonic one:

$$V^{\text{eff}}_{\text{anharm}} = \frac{1}{2}(\Delta X_n - L)^2 \Big[K + 2K_3(\Delta X_n - L) \Big] = \frac{M\omega^2_{\text{eff}}}{2} (\Delta X_n - L)^2 \,. \tag{C.2}$$

One can then express ω_{eff} using the formula describing the temperature dependence of the frequency of radial breathing modes (RBM)[1] provided in Ref. [38]:

$$\omega_{\text{anharm}}(T) = \omega_0 (1 + pT) \,, \tag{C.3}$$

$\omega_0 = 36.3 \times 10^{12}\,\text{Hz}$ being the zero-temperature RBM frequency and p being a temperature coefficient whose value was estimated to be $-5 \times 10^{-5}\,\text{K}^{-1}$ from molecular dynamics simulations of a $(10, 10)$ CNT [40]. Consequently:

$$K + 2K_3|(\Delta X_n - L)| = M\omega^2_{\text{eff}} = M\omega^2_{\text{anharm}}(T) = M\omega_0^2(1 + pT)^2 \,, \tag{C.4}$$

in which the module of the displacement was taken because K_3 must be negative and because $M\omega^2_{\text{anharm}}(T) < K$, since $M\omega_0^2 < K$ and p is negative.

This idea is now used with two different methods and in both cases the consistency of this procedure will be ensured, checking whether the original potential is always positive for the obtained estimate of K_3.

[1] Radial breathing modes are collective modes of the nanotube in which C atoms move in the radial direction, i.e. orthogonally to the CNT axis, causing an expansion or a contraction of the CNT radius.

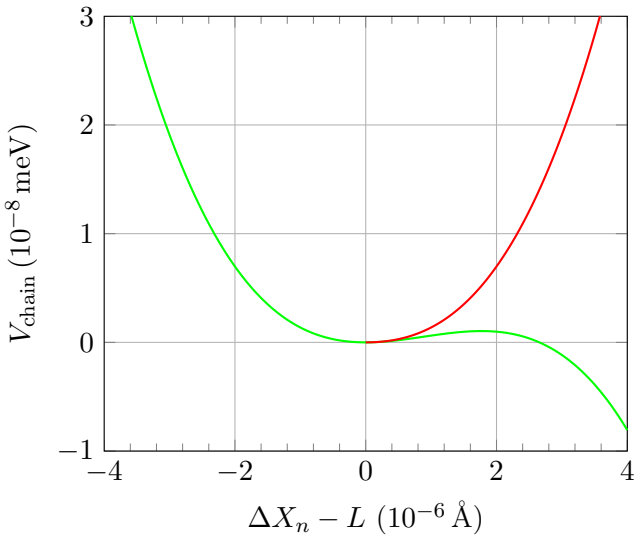

Figure C.1: Visual representation of the idea used to estimate the anharmonic coefficient K_3; the green line represents the anharmonic potential for $K_3 = -6.0 \times 10^{16}\,\mathrm{N/m^2}$, while the red one its "stabilization" for positive displacements.

C.1 Finite temperature case: comparison with the thermal quantum

In the first method the effective potential energy is compared with the thermal quantum $k_\mathrm{B}T$:

$$V^{\text{eff}}_{\text{anharm}} = \frac{M\omega^2_{\text{eff}}}{2}(\Delta X_n - L)^{*2}_T = k_\mathrm{B}T\,, \tag{C.5}$$

obtaining an expression for the spring displacement $(\Delta X_n - L)^*_T$ at temperature T :

$$|(\Delta X_n - L)^*_T| = \sqrt{\frac{2k_\mathrm{B}T}{M\omega_0^2(1+pT)^2}}\,. \tag{C.6}$$

One can then estimate K_3 by inserting (C.6) in (C.4)

$$K_3^{(1)} = \frac{M\omega_0^2(1+pT)^2 - K}{2\sqrt{\frac{2k_\mathrm{B}T}{M\omega_0^2(1+pT)^2}}}\,, \tag{C.7}$$

procedure which yields a value of approximately $-1.8 \times 10^{11}\,\mathrm{N/m^2}$ for a temperature of 300 K.

C.2 Zero-temperature estimate

In the second method one starts from

$$K + 2K_3(\Delta X_n - L)^*_T = M\omega_0^2(1+pT)^2 \tag{C.8}$$

and inserts $T = 0\,\mathrm{K}$ and $|(\Delta X_n - L)^*_0| = \mathcal{O}(5.2 \times 10^{-4}\,\text{Å})$, corresponding to the average amplitude of spring displacements for $(V_0, v_0^{\text{lab}}) = (0.1\,\mathrm{meV}, 230\,\mathrm{m/s})$ and $(1.0\,\mathrm{meV}, 630\,\mathrm{m/s})$ in the harmonic case. This procedure yields to a second estimate:

$$K_3^{(2)} = \frac{(M\omega_0^2 - K)}{2|(\Delta X_n - L)^*_0|} \approx -5.4 \times 10^{13}\,\mathrm{N/m^2}\,. \tag{C.9}$$

C.3 Comments on the two estimates

First of all, both estimates are deemed to be self-consistent with the initial hypothesis of neglecting K_4 since, for the values of K and L used in **Chapter 3** of this thesis project, they are able to provide a

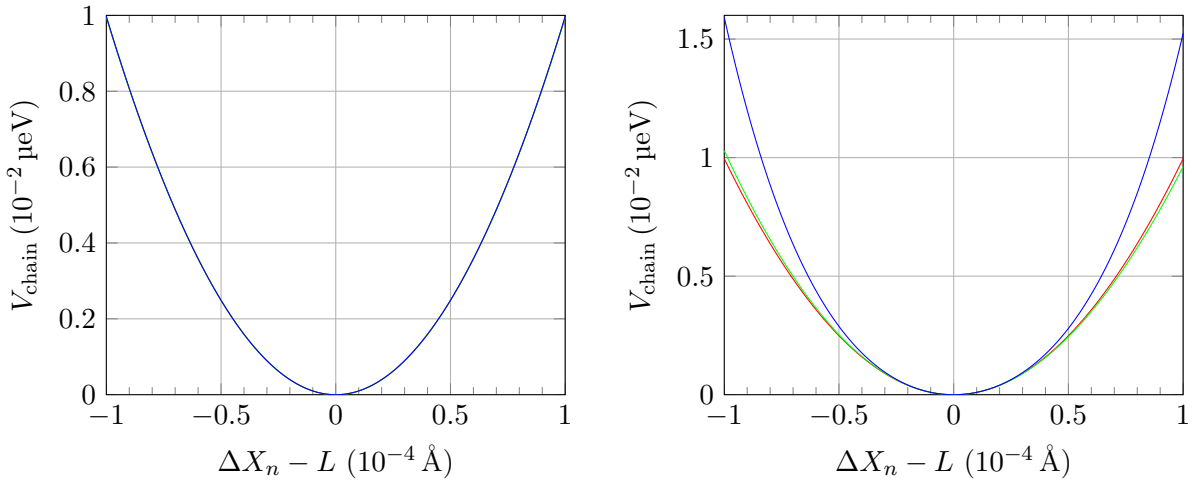

(a) With $K_3^{(1)}$ **(b)** With $K_3^{(2)}$

Figure C.2: Plots of the anharmonic potential with the estimated values of K_3 and with $K_4 = K_3/(-6\times10^{-16}\,\text{m})$: the red plot is the harmonic potential, the green one presents the K_3 contribution and the blue one also the K_4 term. At variance with $K_3^{(1)}$, $K_3^{(2)}$ gives rise to appreciable effects in the harmonic potential.

potential which is always positive and hence stable also in absence of K_4 contribution, as shown in **Figure C.2**. Furthermore, both of them are in the range of values of K_3 used to study dissipation curves, i.e. $[-10^{17}, -10^{10}]\,\text{N/m}^2$.

Anyway, as one can see from **Figure C.2**, $K_3^{(1)}$ is too small to produce an appreciable difference with respect to the purely harmonic case, even when a $K_4 = K_3/(-6\times10^{-16}\,\text{m})$ is introduced, while $K_3^{(2)}$ is able to change the shape of the potential, even in absence of K_4. Consequently, $K_3^{(2)}$ was deemed to be a more relevant estimate for the third order anharmonic coefficient.

Bibliography

[1] M. S. Dresselhaus and P. C. Eklund, Phonons in carbon nanotubes, Adv. Phys. **49**, 705–814 (2000).

[2] M. Whitby, L. Cagnon, M. Thanou, and N. Quirke, Enhanced Fluid Flow through Nanoscale Carbon Pipes, Nano Lett. **8**, 2632–2637 (2008).

[3] M. Majumder, N. Chopra, R. Andrews, and B. J. Hinds, Nanoscale hydrodynamics: Enhanced flow in carbon nanotubes, Nature **438**, 44 (2005).

[4] J. K. Holt, H. G. Park, Y. Wang, M. Stadermann, et al., Fast Mass Transport Through Sub-2-Nanometer Carbon Nanotubes, Science **312**, 1034–1037 (2006).

[5] E. Secchi, S. Marbach, A. Niguès, D. Stein, et al., Massive radius-dependent flow slippage in carbon nanotubes, Nature **537**, 210 (2016).

[6] A. Ambrosetti, P. L. Silvestrelli, and L. Salasnich, Superfluidity Meets the Solid State: Frictionless Mass Transport through a (5,5) Carbon Nanotube, Phys. Rev. Lett. **131**, 206301 (2023).

[7] A. Ambrosetti and P. L. Silvestrelli, Quantum-mechanical water-flow enhancement through a sub-nanometer carbon nanotube, J. Chem. Phys. **159**, 204709 (2023).

[8] A. Kokalj, Computer graphics and graphical user interfaces as tools in simulations of matter at the atomic scale, Comp. Mater. Sci. **28**, 155–168 (2003).

[9] N. W. Ashcroft and N. D. Mermin, Solid State Physics (Holt-Saunders, 1976)

[10] G. Guennebaud, B. Jacob, et al., *Eigen v3*, 2010, URL: `http://eigen.tuxfamily.org`.

[11] P. K. Jarnet, Gnuplot in Action. Understanding data with graphs (Manning, 2016)

[12] W. C. Swope, H. C. Andersen, Berens P. H., and Wilson K. R., A computer simulation method for the calculation of equilibrium constants for the formation of physical clusters of molecules: Application to small water clusters, J. Chem. Phys. **76**, 637–649 (1982).

[13] L. Verlet, Computer "Experiments" on Classical Fluids. I. Thermodynamical Properties of Lennard-Jones Molecules, Phys. Rev. **159**, 98–103 (1967).

[14] C. Runge, Ueber die numerische Auflösung von Differentialgleichungen, Math. Ann. **46**, 167–178 (1895).

[15] M. Kutta, Beitrag zur näherungsweisen Integration totaler Differentialgleichungen, Z. Angew. Math. Phys. **46**, 435–453 (1901).

[16] F. von Oppen, F. Guinea, and E. Mariani, Synthetic electric fields and phonon damping in carbon nanotubes and graphene, Phys. Rev. B **80**, 075420 (2009).

[17] J. Wang, M. Ma, and E. Tosatti, Kinetic friction of structurally superlubric 2D material interfaces, J. Mech. Phys. Solids **180**, 105396 (2023).

[18] P. Giannozzi, S. Baroni, N. Bonini, M. Calandra, et al., QUANTUM ESPRESSO: a modular and open-source software project for quantum simulations of materials, J. Phys. Condens. Matter **21**, 395502 (2009).

[19] P. Giannozzi, O. Andreussi, T. Brumme, O. Bunau, et al., Advanced capabilities for materials modelling with Quantum ESPRESSO, J. Phys. Condens. Matter **29**, 465901 (2017).

[20] P. Giannozzi, O. Baseggio, P. Bonfà, D. Brunato, et al., Quantum ESPRESSO toward the exascale, J. Chem. Phys. **152**, 154105 (2020).

[21] P. Hohenberg and W. Kohn, Inhomogeneous Electron Gas, Phys. Rev. **136**, B864–B871 (1964).

[22] L. Salasnich, Quantum Physics of Light and Matter (Springer Cham, 2017)

[23] L. H. Thomas, The calculation of atomic fields, Math. Proc. Camb. Philos. Soc. **23**, 542–548 (1927).

[24] E. Fermi, Un metodo statistico per la determinazione di alcune proprietà dell'atomo, Rend. Lincei **6**, 602–607 (1927).

[25] P. A. M. Dirac, Note on Exchange Phenomena in the Thomas Atom, Math. Proc. Camb. Philos. Soc. **26**, 376–385 (1930).

[26] C. F. von Weizsäcker, Zur Theorie der Kernmassen, Z. Phys. **96**, 431–458 (1935).

[27] W. Kohn and L. J. Sham, Self-Consistent Equations Including Exchange and Correlation Effects, Phys. Rev. **140**, A1133–A1138 (1965).

[28] W. Kohn, Y. Meir, and D. E. Makarov, van der Waals Energies in Density Functional Theory, Phys. Rev. Lett. **80**, 4153–4156 (1998).

[29] J. T. Fery and D. J. Dorem, *TubeGen 3.4*, University of Delaware, Newark DE, 2011, URL: `http://turin.nss.udel.edu/research/tubegenonline.html`.

[30] J. P. Perdew, K. Burke, and M. Ernzerhof, Generalized Gradient Approximation Made Simple, Phys. Rev. Lett. **77**, 3865–3868 (1996).

[31] J. P. Perdew, in: *Electronic Structure of Solids '91,* ed. by P. Ziesche and H. Eschrig, (Akademie Verlag, 1991) 11.

[32] S. Grimme, Semiempirical GGA-type density functional constructed with a long-range dispersion correction, J. Comput. Chem. **27**, 1787–1799 (2006).

[33] R. Sabatini, T. Gorni, and S. de Gironcoli, Nonlocal van der Waals density functional made simple and efficient, Phys. Rev. B **87**, 041108 (2013).

[34] O. A. Vydrov and T. Van Voorhis, Nonlocal van der Waals density functional: The simpler the better, J. Chem. Phys. **133**, 244103 (2010).

[35] K. Berland and P. Hyldgaard, Exchange functional that tests the robustness of the plasmon description of the van der Waals density functional, Phys. Rev. B **89**, 035412 (2014).

[36] G. Candiotto, F. R. Silva, D. G. Costa, and R. B. Capaz, Strain, anharmonicity, and finite-size effects on the vibrational properties of linear carbon chains, Phys. Rev. B **109**, 045405 (2024).

[37] S. Gupta, K. Dharamvir, and V. K. Jindal, Implicit phonon shifts and thermodynamical properties of rigid Carbon Nanotube bunches, AIP Advances **2**, 042192 (2012).

[38] H. Wang, D. Dickel, and M. S. Daw, Study of the Anharmonicity of Vibrational Modes in Carbon Nano-Materials Using a Moments-Based Approach, J. Raman Spectrosc. **49**, 621–626 (2018).

[39] T. Umakoshi, M. Taniguchi, and P. Verma, Anharmonic Effects in Single-Walled Carbon Nanotubes Analyzed through Low-Temperature Raman Imaging, J. Phys. Chem. C **124**, 6922–6928 (2020).

[40] N. R. Raravikar, P. Keblinski, A. M. Rao, M. S. Dresselhaus, et al., Temperature dependence of radial breathing mode Raman frequency of single-walled carbon nanotubes, Phys. Rev. B **66**, 235424 (2002).